Deep radio continuum study of NGC 4631 and its Faraday tomography

Dissertation
zur
Erlangung des Doktorgrades (Dr. rer. nat.)
der
Mathematisch-Naturwissenschaftlichen Fakultät
der
Rheinischen Friedrich-Wilhelms-Universität Bonn

von
Silvia Carolina Mora Partiarroyo
aus
Caracas, Venezuela

Bonn, 28.01.2016

Dieser Forschungsbericht wurde als Dissertation von der Mathematisch-Naturwissenschaftlichen Fakultät der Universität Bonn angenommen und ist auf dem Hochschulschriftenserver der ULB Bonn http://hss.ulb.uni-bonn.de/diss_online elektronisch publiziert.

1. Gutachter:	Hon. Prof. Dr. Michael Kramer
2. Gutachter:	Prof. Dr. Thomas Reiprich
Tag der Promotion:	30.06.2016
Erscheinungsjahr:	2016

Abstract

Radio continuum observations of NGC 4631 were performed with the Karl G. Jansky Very Large Array (EVLA) at C-band in the C & D array configurations, and at L-band in the B, C & D array configurations. In order to recover the large-scale emission that is missing due to the incomplete u,v sampling of the interferometer, the data were combined with single-dish Effelsberg data. Observations of NGC 4631 with the Effelsberg telescope were performed at 1.42 and 4.85 GHz.

In order to determine the best approach to separate the thermal and nonthermal components of the total radio emission in the context of edge-one galaxies, we derive the thermal emission of NGC 4631 on a pixel-by-pixel basis by using three different methods to account for dust extinction. The Hα emission is optically thick along the entire disk of NGC 4631 and it becomes optically thin with larger z-distance. Therefore, the method which uses the $I_{70\mu m}/I_{160\mu m}$ to correct the observed Hα emission for extinction (Tabatabaei et al. 2007) should be applied with caution for edge-on galaxies due to the optically thick nature of the disk emission. The method which employs the calibrations that only use the 24 μm luminosity to estimate the extinction-corrected Hα emission appear to overestimate the correction for extinction when compared to results obtained with the other two methods. We conclude that the most promising approach to estimate the thermal emission for NGC 4631 and other edge-on galaxies consists of using the calibrations that combine Hα and 24 μm data. The resulting global thermal fraction of NGC 4631 at C-band (L-band) is 15±3% (6±1%). This is the first time maps of the distribution of synchrotron emission and synchrotron spectral indices have been derived for an edge-on galaxy.

The mean vertical scale height of the total radio emission observed at C-band for the thick disk (3.4 ± 0.9 kpc) is larger by a factor of 1.9 with respect to the mean scale height of the thick disk found in five other edge-on spiral galaxies. This may be related to the tidal interaction NGC 4631 is undergoing with its neighboring galaxies. The largest scale heights in both frequency bands of the thinner component of the synchrotron radiation correspond to emission in the southeast and southwest of the

galaxy. At C-band (L-band) these scale heights are a factor of 2-7 (2-3) larger than the scale heights of the synchrotron-emitting thin disk found in other parts of the galaxy. Therefore, it seems we have not detected a thin disk in these regions within NGC 4631. We believe this might be associated with the disturbances present in these areas of the disk (visible as supershells in HI Rand & van der Hulst 1993) and/or it might be an indication that the disk is warped.

The Faraday depths at C-band and at L-band are characterized by a smooth large-scale distribution, indicating that NGC 4631 has a large-scale regular magnetic field. The Faraday depths in the northern halo of NGC 4631 vary smoothly from $\sim 200\ \mathrm{rad \cdot m^{-2}}$ to about $-150\ \mathrm{rad \cdot m^{-2}}$ in a quasi-periodic pattern, indicating that the magnetic field in the sky plane has a systematic change in direction on scales of about 1.9 kpc. This is the first time the strength of the turbulent and ordered magnetic field in the sky plane have been derived on a pixel-by-pixel basis for an edge-on galaxy. The total magnetic field of NGC 4631 has a mean strength of $\langle \mathrm{B_{eq}} \rangle \approx 9 \pm 0.7\ \mu\mathrm{G}$ in the disk, and a mean strength of $\langle \mathrm{B_{eq}} \rangle \approx 7 \pm 1.5\ \mu\mathrm{G}$ in the halo. In addition, the ordered magnetic field in the plane of the sky has a mean strength of $\langle \mathrm{B_{o,\perp}} \rangle \approx 1\ \mu\mathrm{G}$ in the disk and $\langle \mathrm{B_{o,\perp}} \rangle \approx 2\ \mu\mathrm{G}$ in the halo (values represent lower limits).

Among all of the edge-on galaxies observed so far, only NGC 4631 seems to have a different field orientation in its disk. Along the eastern and western sides of its disk the magnetic field orientation is parallel to the galactic plane, but in the central region of the disk a vertical field seems to dominate at low angular resolution. To uncover the disk magnetic field in the center of NGC 4631 we analyze high-resolution Faraday-corrected data at $\lambda 3.6$ cm observed using the Very Large Array Telescope (VLA). We demonstrate that merging single-dish with interferometer data increases the zone of depolarization along the disk of NGC 4631. Our study indicates that the magnetic field orientation along the central 5-7 kpc of the disk is parallel to the midplane of the galaxy, which is only clearly visible in the high-resolution $\lambda 3.6$ cm VLA data. Therefore, we confirm that NGC 4631 also has a magnetic field structure plane-parallel along its entire disk.

The spectral index distribution between C-band and L-band of the background radio galaxy to the southwest of NGC 4631 is flat in the outskirts of the lobes and steepens towards the core. This spectral index distribution is typical of FR II radio galaxies and is consistent with the backflow model. The background radio galaxy has an average degree of polarization of 6% at L-band and its Faraday depths are rather uniform over the two lobes with an average value of $21 \pm 13\ \mathrm{rad \cdot m^{-2}}$. Its intrinsic magnetic field is orientated parallel to the radio galaxy's main axis.

A mi AmmaB.

Emancipate yourselves from mental slavery,
none but ourselves can free our minds.
Have no fear for atomic energy,
‘cause none of them can stop the time.
Won’t you help to sing these songs of freedom?
‘Cause all I ever have: redemption songs.

Bob Marley, Redemption Song

Contents

Preface

Magnetic fields pervade the universe at all astrophysical scales. They have been detected in or around essentially all astronomical objects by the electromagnetic radiation emitted by cosmic rays, gas or dust. The Earth (Courtillot & Le Mouel 1988), the Sun (Parker 1970), and other planets (Jones 2011) and stars (Pérez-Sánchez et al. 2013; Donati & Landstreet 2009; Chanmugam 1992) have considerable magnetic fields. In addition, large-scale magnetic fields have been studied in our Milky Way (Haverkorn 2015), in other galaxies (Beck 2015) and in clusters of galaxies (Carilli & Taylor 2002). Furthermore, magnetic fields have been observed in molecular clouds (Crutcher 2012), in active galactic nuclei (Hovatta et al. 2012) and even in masers (Pérez-Sánchez & Vlemmings 2013).

Typical magnetic field strengths in the universe range from several microgauss (μG), in galaxies or clusters, to a few gauss on planets like the Earth. All these fields are probably originated from the motion of electrically charged fluids which can be explained by the so-called *dynamo effect*. This effect is based on the conversion of kinetic energy into magnetic energy, which occurs by means of stretching, twisting and folding of the magnetic field lines (Brandenburg et al. 2010; Cho & Ryu 2009). Up to now it is believed to be the most promising mechanism to explain the amplification and ordering of magnetic fields (Beck et al. 1996). Several dynamo models have been proposed (Wielebinski & Krause 1993; Beck et al. 1996). For instance, the $\alpha - \Omega$ dynamo which is based on differential rotation (the Ω-effect) and the turbulent motion of the interstellar gas (α-effect).

The main idea is that initial *seed fields*, generated either by a process in the early universe or by some more recent astrophysical mechanism, are amplified to μG strengths by dynamo action. The presence of a seed field is necessary since the dynamics of astrophysical plasmas are ruled by magnetohydrodynamics (MHD), and within this theory the induction equation does not have a source term. This means that the dynamo mechanism cannot generate, but only amplify, magnetic fields. The origin of these initial seed fields, however, constitutes today a rather intriguing point in physical theories. Various scenarios for the origin of initial seed fields are discussed in Widrow et al. (2012). Overall, two broad theories can explain the origin of these seed fields. On one hand, seed fields may be *primordial*, which means they were generated in the early Universe before any structure formation took place (Caprini et al. 2009; Battaner & Lesch 2000). On the other hand, they might have been generated during the phase of cosmological structure formation by diverse mechanisms like the Weibel instability (Schlickeiser 2005), injection by stars or jets (Rees 2005) or the Biermann mechanism operating in supernova remnants (Hanayama et al. 2005).

Magnetic fields play an important role in many astrophysical contexts. They control the density and distribution of cosmic rays. While magnetic fields reduce the star formation rate by stabilizing gas clouds, they can also help in the formation of stars by removing the angular momentum from protostellar clouds via ambipolar diffusion (McKee & Ostriker 2007). In addition, a small ionization fraction is enough for the magnetic field to be coupled to the ionized and neutral gas (Cox 2005). Furthermore, magnetic reconnection can be a possible heating source for the interstellar medium (Birk et al. 1998). Current observations of magnetic fields in galaxies indicate that these play a crucial part in the evolution of galaxies and in the formation of their large-scale structure. For example, they contribute immensely to the total pressure within a galaxy that helps balance the gas in the galactic disk against gravitational collapse (Beck & Wielebinski 2013), and they can also affect gas flows in spiral arms (Gómez & Cox 2002). Magnetic fields may be important to understand how the disk and halo in galaxies interact, and thus in determining how matter and energy are redistributed throughout a galaxy. In consequence, this can also shed some light in the formation and evolution of galaxy clusters by feedback processes.

Many fundamental questions related to the origin, role and evolution of magnetic fields in galaxies remain unanswered. For instance, how important are magnetic fields for the physics behind the formation of spiral arms or the generation of outflows in galaxies? Can outflows from galaxies magnetize intergalactic space? Can magnetic fields influence the dynamics of galaxies and vice versa? What is the relation between magnetic fields, star formation and galactic winds? How do the gaseous layers of a galaxy interact with the magnetic field? The aim of this thesis is to contribute in the scientific search to answer these and many other intriguing questions in the scope nearby galaxies. Although our Milky Way can provide knowledge concerning the local structure of the galactic magnetic field, observations of external galaxies are a very valuable tool for the reconstruction of global features of galactic magnetic fields. The edge-on spiral galaxy NGC 4631 was chosen as target due to its spectacular radio halo, its fascinating morphology and its unique environment.

In external galaxies the best tracer of the magnetic field is synchrotron radiation, which is best probed with radio continuum observations at cm wavelengths. With the recently updated Karl G. Jansky Very Large Array[1], i.e. the Expanded Very Large Array (EVLA), high resolution observations were performed. The new wide bandwidth capabilities of the EVLA provide us with the highest sensitivity achieved up to now for interferometer observations. Chapter 1 of this thesis offers a brief overview of the physical processes behind electromagnetic radiation and it provides the reader with the necessary concepts to interpret the radio continuum observations. A short overview of previous observations of NGC 4631 is presented in Chapter 2. The data reduction techniques used throughout this work are explained in Chapter 3, together with a detailed description of the interferometer and single-dish radio observations. Analyses of the total power emission is presented in Chapter 4, while Chapter 5 carefully explains how the thermal radio emission of NGC 4631 is derived on a pixel-by-pixel basis. Chapter 6 presents the analysis of the synchrotron and polarized emission of NGC 4631 in order to understand the properties of its magnetic field, and Chapter 7 focuses solely on the orientation of the magnetic field along the disk of the galaxy. Finally, a summary of the thesis is presented in Chapter 8.

---

[1] The EVLA is operated by the National Radio Astronomy Observatory (NRAO), a facility of the National Science Foundation operated under cooperative agreement by Associated Universities, Inc.

1

Theoretical Background

"The pursuit of truth and beauty
is a sphere of activity in which we are
permitted to remain children all our lives."
Albert Einstein

In this chapter we present a short summary of the necessary concepts to interpret the radio continuum observations and to study magnetic field in galaxies. For more complete treatments, the reader is referred to books by Melia (2009), Longair (2011), Pacholczyk (1970), Draine (2010) and Klein & Fletcher (2015). The lecture notes by Prof. Dr. Uli Klein on 'Radio Astronomy: Tools, Applications & Impacts' (course astro841) can be retrieved from this website[1]. In section 1.1 we briefly explain the main radiation processes in astrophysical plasmas which are necessary to understand in order to study the properties of magnetic fields. In section 1.2 we describe the main tools available to investigate magnetic fields in galaxies. Thermal free-free radiation contaminates the total radio emission we observe, therefore it is important to quantify its contribution. Interstellar dust grains play an important role in estimating the thermal radiation of galaxies since they attenuate the Hα emission and emit infrared radiation, as we will explain in Chapter 5. Thus, in section 1.3 we give a short overview of the properties of dust particles in the interstellar medium.

---

[1] `https://astro.uni-bonn.de/~uklein/`

1.1 Radiative processes

1.1.1 Thermal free-free radiation

This type of radiation was first noted by Nikola Tesla in the 1880s and is also called *braking radiation* or, in German, *Bremsstrahlung*. It is produced by the deceleration of a charged particle when it is deflected by the Coulomb field of another charged particle. This occurs in ionized regions where free electrons are elastically scattered off ions and escape as free electrons, this is why it is called a free-free transition. This interaction results in loss of kinetic energy which causes transitions between unbound states of the electron where a photon is emitted to satisfy the law of conservation of energy. The electrons move at thermal velocities, according to the temperature of the electron gas.

Often the medium is not thin enough for the radiation to escape without interacting with the plasma that produced it. This can be determined at a specific frequency ν through the optical depth (Longair 2011):

$$\tau_\nu = \int_0^L \chi_\nu \, dl = 3.01 \cdot 10^{-2} \left(\frac{\nu}{\mathrm{GHz}}\right)^{-2} \left(\frac{T_e}{10^4\ \mathrm{K}}\right)^{-1.5} \cdot g_{ff} \cdot \int_0^L \left(\frac{n_e}{\mathrm{cm}^{-3}}\right)^2 \left(\frac{dl}{\mathrm{pc}}\right) \tag{1.1}$$

where χ_ν is the absorption coefficient, l is the pathlength, T_e is the temperature and n_e the density of the thermal electrons. The parameter g_{ff} is the gaunt factor defined for free-free emission as:

$$g_{ff} = 12.5 + \ln \left[Z^{-1} \left(\frac{T_e}{10^4\ \mathrm{K}}\right)^{1.5} \left(\frac{\nu}{\mathrm{GHz}}\right)^{-1} \right] \tag{1.2}$$

where Z is the charge number of the ionized atom. If the optical depth is less than one then the medium is optically thin, otherwise it is known as optically thick. Equation 1.1 applies only for neutral plasmas where the electron density is equal to the density of ions. The integral along the line-of-sight of the thermal electron density squared is defined as the *emission measure*:

$$EM = \int_0^L \left(\frac{n_e}{\mathrm{cm}^{-3}}\right)^2 \left(\frac{dl}{\mathrm{pc}}\right) \tag{1.3}$$

If the medium is optically thick ($\tau \gg 1$), the radiation and plasma can reach a local thermodynamical equilibrium and the radiation emerges with the intensity of a blackbody according to Planck's law:

$$I_\nu = B_\nu(T_e) = \frac{2h\nu^3}{c^2[\exp(h\nu/kT_e) - 1]} \tag{1.4}$$

At high temperatures or long wavelengths ($h\nu \ll kT_e$) Planck's law turns into the Rayleigh-Jeans expression:

$$I_\nu = B_\nu(T_e) = \frac{2h\nu^2 kT_e}{c^2} \tag{1.5}$$

and then the temperature, which in this case is referred to as the *brightness temperature*, can be estimated from the intensity of the radiation. Equation 1.5 shows that optically thick free-free emission has a spectral index of $\alpha = 2$ in the Rayleigh-Jeans limit.

If the medium is optically thin ($\tau \ll 1$), the intensity of the radiation becomes:

$$I_\nu = \tau_\nu \cdot B_\nu(T_e) = 8.29 \cdot 10^{-23} \left(\frac{EM}{\mathrm{pc \cdot cm^{-6}}}\right) \left(\frac{T_e}{10^4 \mathrm{K}}\right)^{-0.5} \cdot g_{ff} \tag{1.6}$$

Due to the frequency dependence of the Gaunt factor, the free-free radiation spectrum in the optically thin regime has a spectral index of $\alpha = -0.1$. Thermal free-free radiation is unpolarized since the trajectories of its electrons are randomly oriented. This form of spectrum is typically found in warm ionized gas around regions of recent star formation where the main contributor to the ionization are hot, young, massive stars.

1.1.2 Nonthermal synchrotron radiation

Synchrotron radiation of relativistic electrons dominates much of the emission studied in high energy astrophysics and is the main diagnostic tool to trace magnetic fields in the interstellar medium (ISM) and the intergalactic medium (IGM). This radiation is emitted by relativistic electrons that are accelerated in turbulent plasmas. In the ISM, electrons may be accelerated due to supernova explosions or by active galactic nuclei (AGN) and in the IGM this is caused, for example, by galaxy merges.

The energy and momentum transferred to the relativistic electrons are provided by a magnetic field which accelerates the particles according to the Lorentz force ($\mathbf{F} = \mathrm{q}\mathbf{E} + \mathrm{q}\mathbf{v}/\mathrm{c} \times \mathbf{B}$). These electrons gyrate along magnetic field lines, continuously emitting what we know as *synchrotron radiation*. This radiation is responsible for most of the radio emission of our Galaxy, of many extragalactic radio sources and of supernova remnants.

The energy spectrum of an ensemble of relativistic electrons was measured in Earth's vicinity by studying the cosmic rays that reach our atmosphere. The cosmic ray energy spectrum is a power-law of the form (Pacholczyk 1970):

$$N(E)dE = KE^{-\gamma}dE, \tag{1.7}$$

where $N(E)dE$ is the number density of electrons in the energy interval E to $E + dE$, K is a normalization constant and γ is an index that varies over the range $\sim 2 - 2.5$. Since the energy spectrum does not follow a Maxwellian distribution this type of radiation is often called *nonthermal synchrotron emission*. With this energy distribution the intensity produced by an ensemble of relativistic electrons can be simplified to:

$$I_\nu \propto B_\perp^{1+\alpha} \nu^{-\alpha} \tag{1.8}$$

where $B_\perp$ is the strength of the magnetic field perpendicular to the line-of-sight (LOS) and the spectral index is equal to $\alpha = (\gamma - 1)/2$. Therefore, the index α of the radiation spectrum is determined by the slope of the electron energy spectrum γ.

At low enough frequencies self-absorption effects are expected to be important, this means that synchrotron emission becomes optically thick. Thus, the nonthermal synchrotron spectrum is a power law everywhere except below a break frequency ν_b, whose value depends on the properties of the medium. This limit is set by the balance between emission and reabsorption by the radiating particles. Below the break frequency the slope of the synchrotron spectrum does not depend on the spectral index ($\nu^{5/2}$). In figure 1.1 the typical spectrum of a self-absorbed radio source emitting synchrotron radiation is shown. Spectra of roughly this form are found in the nuclei of active galaxies and quasars.

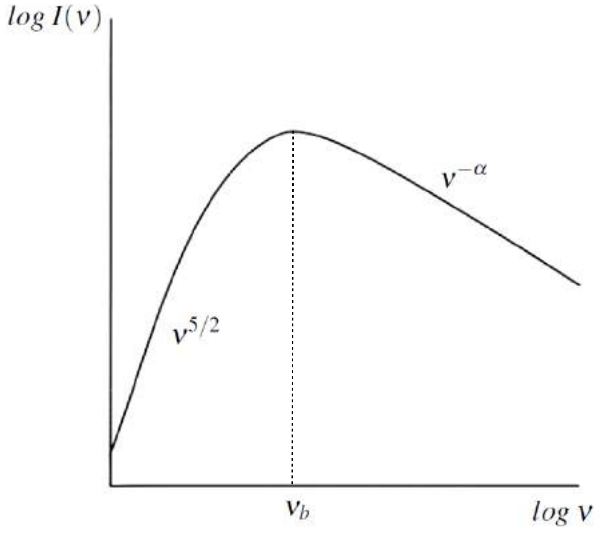

FIGURE 1.1— Synchrotron spectrum exhibiting self-absorption. The optically thin synchrotron spectrum increases toward lower frequencies, until it reaches the break frequency ν_b. From this point on the particles begin to be reabsorbed and the spectrum drops with decreasing frequency. Based on an illustration by Longair (2011).

One of the most important properties of synchrotron radiation is that it is polarized, unlike free-free radiation. The radiation from a single electron is elliptically polarized.

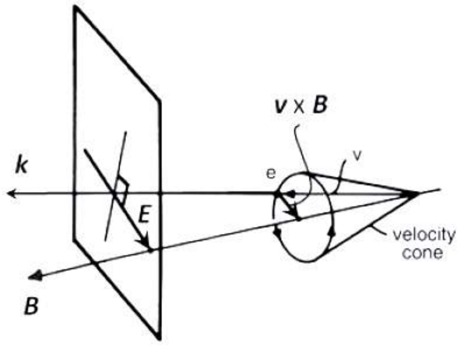

FIGURE 1.2— Velocity cone of a relativistic particle in the presence of a magnetic field. Illustrates the polarization of the received radiation. From Longair (2011).

This is not the case, however, for an ensemble of particles with a distribution of pitch angles. At this point it is helpful to introduce the concept of the velocity cone with help of figure 1.2. This is the cone described by the velocity vector of the electron as it spirals around the magnetic field. The axis of the cone is along the direction of the magnetic-field vector and the velocity vector processes about this direction. Thus, the opening angle of the cone is twice the pitch angle. All of the radiation components, linearly polarized and circularly polarized, are merged together in the velocity cone. Figure 1.3 shows that the two circularly polarized components cancel each other out, leaving only a contribution to the linear polarization. Hence, the net result is a linearly polarized wave. The polarization properties together with the frequency dependence of the radiation are important features by which we can discern synchrotron from free-free emission.

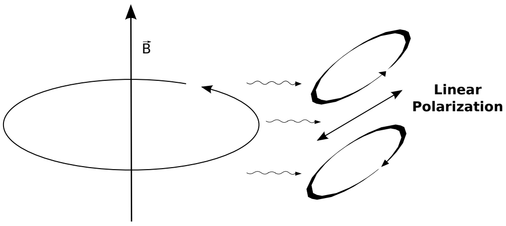

FIGURE 1.3— Illustration on how linear polarization is produced by synchrotron radiation. Based on a plot by Melia (2009).

1.1.3 Inverse-Compton radiation

In Compton scattering a collision occurs between a charged particle and a photon. The photon then transfers some of its energy and momentum to the charged particle and consequently, the scattered photon has less energy and momentum after the collision. Since the energy and momentum of the photon is proportional to frequency, the loss of energy of the photon corresponds to an increase in its wavelength. If the charged particle is more energetic than the photon, then the opposite happens and the charged particle scatters the low energy photon to high energies so that the photon gains energy at the expense of the kinetic energy of the charged particle. This is known as *inverse-Compton scattering* because the charge loses energy rather than the photon. Inverse-Compton scattering is important in our case since cosmic ray electrons propagate through the radiation field of the galaxy and lose part of their energy by producing inverse-Compton radiation. Since both synchrotron and inverse-Compton radiation have similar energy dependences, it is difficult to distinguish between synchrotron and inverse Compton losses based on the shape of the radio spectrum alone.

1.2 How do we trace magnetic fields in astrophysical plasmas?

1.2.1 Synchrotron polarization

Since synchrotron radiation is polarized it has become a valuable tool to research magnetics fields in the Universe. The total intensity of the synchrotron emission measures the strength of the total magnetic field, while the linearly polarized intensity reveals the strength and the structure of the ordered field perpendicular to the LOS.

The polarization state of an electromagnetic wave is described by the Stokes parameters I, U, Q and V. The Stokes parameters are useful to express the polarization properties as vectors on a Poincaré sphere. The measured total intensity is referred to as Stokes I and the polarized intensity is defined as:

$$I_{pol} = \sqrt{Q^2 + U^2 + V^2}. \tag{1.9}$$

In the case of linear polarization, however, V $= 0$. The degree of polarization is given by:

$$p_{tot} = \frac{\sqrt{Q^2 + U^2 + V^2}}{I}. \tag{1.10}$$

The polarization angle of the incoming electromagnetic wave can be determined from Stokes Q and U as follows:

$$\psi = (1/2) \arctan(U/Q) \tag{1.11}$$

Measuring the polarization angle is a valuable tool since it provides information concerning the orientation of the observed electric field perpendicular to the LOS. For synchrotron radiation the observed magnetic field is then perpendicular to the electric field.

1.2.2 Faraday rotation

If linearly polarized emission passes through a magnetized plasma the plane of polarization of the electromagnetic wave will rotate, this phenomenon is known as the *Faraday effect*. A linear polarized wave can be decomposed into a right-handed and left-handed circularly polarized component (LHC and RHC). The Faraday effect produces a phase difference between the two circularly polarized components, which is visible as a net rotation of the linear polarization vector. The angle by which the plane of polarization rotates ($\Delta\psi$) is proportional to the rotation measure (RM):

$$\Delta\psi = \lambda^2 \cdot RM. \tag{1.12}$$

Furthermore, the RM is proportional to the LOS integral over the density of thermal electrons multiplied by the strength of the field component parallel to the LOS ($B_{\shortparallel}$):

$$RM = 0.81 \cdot \int_0^L \left(\frac{n_e}{\mathrm{cm}^{-3}}\right) \left(\frac{B_{\shortparallel}}{\mu\mathrm{G}}\right) \left(\frac{dl}{\mathrm{pc}}\right) \ \mathrm{rad} \cdot \mathrm{m}^{-2} \tag{1.13}$$

By measuring the rotation measure one can correct the polarization angles for Faraday rotation and also obtain information about the strength (if we have knowledge of $\mathrm{n_e}$) and the direction of the magnetic field component along the LOS: the sign of the rotation measure indicates the direction of the $\mathrm{B}_{\shortparallel}$-field. By definition, positive values indicate that the $\mathrm{B}_{\shortparallel}$-field is directed towards the observer and negative values indicate that the field is directed away from the observer. Moreover, rotation measure values add up for parallel fields along the LOS, but may cancel for antiparallel fields of equal strength.

The polarization angles, however, can only be determined with an $n \cdot \pi$ ambiguity which leads to an uncertainty in the RM derivation. This is due to the fact that we cannot distinguish between ψ and $\psi \pm n\pi$ (n being an integer). Nevertheless, this problem can be overcome by observing at multiple frequencies and by using the *Rotation Measure Synthesis Technique* (RM-synthesis) which will be explained in section 3.5.

Depolarization

Several effects decrease the polarization degree of a radio source, these can be separated into two according to their origin: instrumental and physical effects. Instrumental effects produce beam depolarization and bandwidth depolarization. Bandwidth depolarization is due to the dependence of the rotation measure on λ^2, this implies that the amount of Faraday rotation of the polarization angle increases with wavelength. Within a frequency band this causes a change in Faraday rotation from one end of the band to the other, and therefore to depolarization. This effect is more severe at longer wavelengths, however, it can be minimized by reducing the channel width of the utilized receiver and by implementing the RM-synthesis technique. Beam depolarization is wavelength independent and is caused by the combination of polarized emission with different polarization angles within the telescope beam.

With respect to the physical effects, which are all wavelength dependent, there are basically three types: differential Faraday rotation, internal Faraday dispersion and external Faraday dispersion. Depolarization by differential Faraday rotation originates within a synchrotron emitting source in a magneto-ionic medium which has an ordered magnetic field along the LOS. The polarization plane of the radio emission produced at different depths within the source is rotated over different angles by the Faraday effect. The superposition along the LOS of these Faraday rotated intrinsic magnetic field vectors leads to depolarization within the source (Gardner & Whiteoak 1966; Burn 1966). In addition, gradients in rotation measure across the beam can also cause differential Faraday rotation depolarization (Sokoloff et al. 1998).

Depolarization by internal Faraday dispersion originates within a synchrotron-emitting source if the magneto-ionic medium contains a random magnetic field. A turbulent magnetic field produces different amounts of Faraday rotation along different lines-of-sight within the beam. If the beam encompasses many turbulent cells this causes internal Faraday dispersion depolarization (Burn 1966; Sokoloff et al. 1998). Depolarization by external Faraday dispersion occurs when there is a turbulent magnetic field located between the observer and the source of synchrotron emission. As long as many turbulent cells are within the beam area along the LOS this effect will depolarize the signal (Sokoloff et al. 1998).

1.3 Interstellar dust particles

Dust grains are solid, macroscopic particles composed of dielectric and refractory materials. Our knowledge of interstellar dust is based mainly on its interaction with electromagnetic radiation, i.e. absorption, scattering and emission of photons by dust particles. Dust was first recognized for its obscuring effects by Trumpler (1930). Because of this effect we need to correct observed intensities, at the optical wavelengths for example, for *dust attenuation* or *extinction*. The term extinction is used to describe the attenuation of the radiation due to both absorption and scattering. Dust grains absorb and scatter electromagnetic waves efficiently at wavelengths less than or equal to their physical sizes but are transparent at longer wavelengths. A complete introduction to the astrophysics of interstellar dust can be found in Krügel (2002); Draine (2003, 2010)

In the optical and infrared wavebands, the effect of dust attenuation can be described by the extinction law $S \propto e^{-\tau}$, where the optical depth τ of the medium depends upon wavelength as $\tau \propto \lambda^{-x}$ ($x = 1$ in the optical and $1.6 \lesssim x \gtrsim 1.8$ in the infrared). The strong dependence of the extinction coefficient upon wavelength explains why attenuation can affect optical and ultraviolet (UV) observations very severely but have a small effect in the infrared waveband.

There are a number of ways that a dust particle may be heated: by absorbing an ultraviolet photon, by collisions with other particles (atoms/electrons/cosmic rays/dust grains), and by absorbing energy from chemical reactions occurring on grain surfaces. However, heating of dust grains is mainly due to absorption of UV photons compared to the other two heating mechanisms Krügel (2002). Dust grains can cool through a number of ways: by emitting a thermal photon, by colliding with cold atoms/molecules, and by sublimation of atoms/molecules from the surface of the grain. In this case radiative cooling is expected to dominate and establish equilibrium Krügel (2002).

Interstellar dust grains are very important for a number of reasons. Dust clouds protect molecules from the interstellar flux of dissociating radiation since they absorb the ultraviolet and optical radiation. In addition, dust grains absorb photons and reradiate them, which becomes an efficient energy loss mechanism for stars which are forming or have just formed. Dust particles absorb the UV photons emitted by stars which form in the densest regions of giant molecular clouds. The dust particles are heated and they radiate in a similar manner as a blackbody but with respect to the emissivity of the material of the grain. The dust particles radiate away the absorbed energy very rapidly at approximately the temperature to which they are heated. This temperature is typically about 30-100 K for the far-infrared (FIR) sources found in dense molecular clouds (Longair 2011). At wavelengths 30-100 μm the dust is transparent and so the energy of the star can be radiated away very efficiently. This explains why areas with intense FIR emission can represent sites of star formation. Therefore, the emission spectrum of dust is an excellent indicator of physical conditions and with its radiated power we can identify star populations.

Dust particles can also be important in interstellar gas dynamics since they communicate radiation pressure from starlight to the gas, and because they provide coupling of the magnetic field to the gas in regions of low fractional ionization. In addition, dust is understood to play an important role in galactic evolution. They also play a major role in the chemistry of interstellar gas by sequestering selected elements in solid grains. Dust particles are also the primary sites of molecular formation, and are thought to be responsible for essentially all of the H_2 in the ISM. Dust is not only the principle molecule builder, it might also be thought of as one of the principal ingredients of planetary formation and life.

1.3.1 Radiation from dust particles

The energy which dust particles absorb from UV photons is reradiated at longer wavelengths, from the infrared to the radio wavebands. In general, the equilibrium temperatures of grains are in the range of 30-50 K or more, which means they radiate mainly at FIR wavelengths of 50-100 μm (Blain et al. 2002).

There are two types of thermal continuum radiation from dust grains. One of them is originated from warm dust grains in thermal equilibrium with the local radiation field (20-40 K). This radiation emerges at mid- to far-infrared wavelengths. In addition, there is thermal continuum emission from nonequilibrium heating of tiny grains emitted at near to mid-infrared wavelengths (1-25 μm).

To account for the observed infrared emission, theoretical models require large numbers of extremely small dust particles that radiate in their optically active vibrational modes once they have absorbed UV photons. In addition to vibrating, these grains will rotate and if they have electric dipole moments there will be rotational emission from these grains at microwave frequencies.

1.3.2 Polarization

In addition to absorbing and scattering light, elongated dust grains can polarize light. This is produced when stellar light propagates through the ISM and becomes linearly polarized as a result of differential extinction by dust grains that are aligned to the interstellar magnetic field. Polarization of starlight was first discovered in the 1940s by Hiltner (1949); Hall & Mikesell (1949). These observations demonstrated that dust grains were nonspherical, and that they had to be globally aligned, presumably by large-scale magnetic fields.

This type of polarization depends on the degree of alignment with the local magnetic field, the angle between the local magnetic field and the LOS, and the degree to which the direction of the magnetic field varies along the LOS. The mechanism responsible for the grain alignment remains a puzzle, but it is overall believed to be related to the magnetic moments of the dust grains. Furthermore, the aligned dust grains that polarize starlight will also produce linearly polarized emission at mm, sub-mm and infrared wavelengths. Because the emission efficiency is greater along the long axis of the grains than along the short axis, there is net polarization of the thermal emission aligned parallel to the long axis. The resulting linear polarization is oriented parallel to the magnetic field, contrary to synchrotron polarization. It is now possible to map this polarized emission from dense regions. For example, the W51 star-forming region has been mapped at 100 μm (Dotson et al. 2000), 850 μm (Chrysostomou et al. 2002), and 1.3 mm (Lai et al. 2001), with linear polarization as large as 10% observed at 1.3 mm.

2

Observational Overview

> *"The real voyage of discovery*
> *consists not in seeking new*
> *landscapes but in having new eyes."*
> Marcel Proust

NGC 4631 is a fascinating barred spiral galaxy located in the constellation Canes Venatici. It was first discovered by William Herschel back in 1787. Viewed nearly edge-on with an inclination of 86°, it is popularly known as the *Whale Galaxy* due to its peculiar shape in the optical. Its eastern halo is thicker than its western halo, giving the galaxy a whale-like appearance, hence its nickname. NGC 4631 is considered to have high star formation activity with no nuclear starburst, but rather a central molecular ring (Irwin et al. 2011) with extended Hα (Rand et al. 1992; Golla et al. 1996; Hoopes et al. 1999) and UV emission (Smith et al. 2001) along its disk. In addition, there is no evidence of hosting an AGN (Ho et al. 1995; Maiolino & Rieke 1995).

The central region of the galaxy has an interesting structure consisting of three collinear emission peaks, according to Duric et al. (1982) who analyzed these features with a resolution of $\sim 10'' \text{ x } 5''$ FWHM. The central peak coincides with the IR center at λ 2.2 μm (Aaronson 1978). Irwin et al. (2011) argue that this location best represents the dynamical center of the galaxy. The western peak resolves into a complex of smaller structures, one of these is possibly a background radio galaxy (Golla 1999). The easternmost radio peak of the triple source coincides with the huge HII region CM 67 (Crillon & Monnet 1969). According to Krause et al. (1994), the nonthermal radio continuum, CO, and HII line emission in CM 67 are physically connected and form a huge star forming region in NGC 4631. Roy et al. (1991)

suggested that the HII region CM 67 might be the tip of a bar. Rand (2000) state that the kinematic evidence from their CO observations favors a rigidly rotating ring instead of a bar. However, it is still a subject of debate whether the inner 4 kpc structure of the galaxy might be a bar or a ring.

Two highly energetic supershells have been detected in HI (21 cm line) near the midplane which have diameters of 3 and 1.8 kpc (Rand & van der Hulst 1993). *Shell 2* (towards the west of CM 67), as labeled in Rand & van der Hulst (1993), seems to be an expanding bubble, whereas *shell 1* (towards the east of CM 67) is most probably caused by an impact of a cloud (Neininger & Dumke 1999). Shell 2 corresponds to a distortion in the eastern side of the galactic disk appearing in all optical, far-ultraviolet (FUV) and Hα maps (Smith et al. 2001). All the rotation curves published at different wavelengths show rigid rotation for radii roughly < 2.4 kpc and differential rotation in the outer parts of the galaxy (Golla & Wielebinski 1994; Rand 1994; Irwin et al. 2011). With respect to the overall movement of the galaxy, the western side is moving towards the observer, while the eastern side is red-shifted (Neininger & Dumke 1999).

Its spectacular halo, observed at various frequencies, is one of the largest known for edge-on galaxies. Therefore, this galaxy constitutes a perfect target to investigate disk-halo interaction. X-ray emission has been observed up to 8 kpc above the plane (Wang et al. 1995, 2001). In addition, NGC 4631 has been observed at various radio wavelengths, at $\lambda 2.8$ cm (Klein et al. 1984; Dumke et al. 1995), $\lambda 3.55$-3.7 cm (Duric et al. 1982; Golla & Hummel 1994; Krause 2009), $\lambda 6.2$ cm (Golla & Hummel 1994), $\lambda 11$ cm (Duric et al. 1982), $\lambda 18$-22 cm (Ekers & Sancisi 1977; Hummel et al. 1988; Heald et al. 2009), $\lambda 49$ cm (Ekers & Sancisi 1977) and $\lambda 91.6$ cm (Hummel & Dettmar 1990). Furthermore, NGC 4631 has been observed at C-band, $\lambda 6$ cm (Golla 1999; Irwin et al. 2012a) and L-band, $\lambda 20$ cm (Golla 1999; Irwin et al. 2012a).

There is even evidence for dust in the halo of NGC 4631. Neininger & Dumke (1999) found cold dust ($\lambda 1.2$ mm) up to distances larger than 10 kpc above the plane of the galaxy that correlate with HI features. In addition, Alton et al. (1999) identified several chimneys or filaments at $\lambda 450$ and 850 μm, which they interpreted as dust outflows connected to the star formation activity in NGC 4631. Other FIR and submillimeter studies of NGC 4631 were also done by Bendo et al. (2006) and Dumke et al. (2004). New observations by Meléndez et al. (2015) with Herschel also show a complex of filaments and chimney-like features at $\lambda 70$ and 160 μm that extend up to 6 kpc above the plane of the galaxy.

The disk of the galaxy is warped, as indicated by dust (Neininger & Dumke 1999), HI (Rand 1994), CO (Golla & Wielebinski 1994; Rand 2000), Hα (Golla et al. 1996; Hoopes et al. 1999), radio (Hummel & Dettmar 1990; Golla & Hummel 1994) and optical (Ann et al. 2011) observations. NGC 4631 is highly disturbed in its eastern disk, whereas the western disk is consistent with a normal spiral viewed edge-on. The position angle of the western disk is 83°(Golla & Wielebinski 1994; Rand 1994), as opposed to the position angle of the whole galaxy of 86°given in the literature. Ann & Park (2006) analyzed the disk morphologies of 325 edge-on galaxies to derive warp statistics and concluded that strong warps are mostly caused by tidal interactions.

The interaction of NGC 4631 with its neighbours is argued to be responsible for the large extent and asymmetries of its halo. According to Makarov & Karachentsev (2011), NGC 4631 is located in a group environment accounting 28 members. Among these, there is the dwarf elliptical galaxy NGC 4627 ($2\overset{'}{.}6$ to the northwest) and the spiral galaxy NGC 4656 ($32'$ to the southeast). Recently, Karachentsev et al. (2014) discovered three low-surface-brightness dwarfs in the NGC 4631 system with small amateur telescopes. Therefore, this system offers an incredible opportunity to research how interactions disturb the gaseous layers of a galaxy.

The interaction between NGC 4631 and NGC 4656 was discovered by Roberts (1968), who mapped the emission from these galaxies in HI. Later on, Weliachew et al. (1978) and Rand (1994) observed these galaxies with the Westerbork Synthesis Radio Telescope (WSRT) and found an HI bridge emerging from NGC 4631 towards NGC 4656 (labeled *spur 1*), an HI concentration stretching out to the south of NGC 4631 (*spur 2*), and two elongated spurs on the northern extension of NGC 4631 (one oriented north-south, *spur 3*, and the other extending to the north-east, *spur 4*). Combes (1978) presented a model for the tidal interaction of the three dominant galaxies NGC 4631, NGC 4656, and NGC 4627. She also suggested that NGC 4627 was once a gas-rich galaxy that had its gas stripped away by the encounter with NGC 4631. Furthermore, optical observations from Vigroux & Nieto (1985) suggest that the dwarf elliptical companion may hold young stars. Last year Martinez-Delgado et al. (2014) detected two stellar tidal streams in the halo of NGC 4631, however, they state these streams are not associated with the HI spurs described above. In addition, they have reproduced these stellar streams by numerical simulations of a tidal interaction between NGC 4631 and a satellite dwarf galaxy (not NGC 4627).

Observations of face-on spiral galaxies show that the magnetic field lines in the disk follow a spiral structure similar to the optical spiral morphology (Beck et al. 1996). In all of the edge-on spiral galaxies studied up to now, the large-scale ordered fields in the disk lie plane-parallel along the disk of the galaxy and in the halo they have an X-shaped morphology (Krause 2009), sometimes with nearly vertical field components above and below the central region (e.g., in NGC 5775, Soida et al. 2011). The disk-parallel magnetic field is the expected edge-on projection of the spiral magnetic disk field seen in face-on galaxies. This large-scale magnetic field in the disk is believed to be amplified by the action of a large-scale $\alpha - \Omega$ dynamo (please refer to preface).

It has been argued for quite some time that NGC 4631 seems to be the only edge-on galaxy that does not exhibit a plane-parallel field in its disk. However, the large-scale vertical field in the disk of NGC 4631 seems to be restricted to the central region

(Krause 2003). Outside of a radius of about 2.5 kpc the field is plane-parallel in the western and eastern halves of the disk. In its outer halo it does present the typical X-shaped configuration seen in the other edge-on galaxies (Golla & Hummel 1994; Krause 2009). Furthermore, above and below the galactic center the halo field is orientated perpendicular to the plane of the galaxy.

Golla & Hummel (1994) argue that the field in the central region of the disk might be wind-driven and that it may be related to the high star-forming activity in this galaxy. However, in a sample of 8 edge-on galaxies (Krause 2012), NGC 4631 does not have such a high star formation rate compared to other edge-on galaxies of different Hubble types. In addition, there are other edge-on galaxies with higher star formation activity that still present plane-parallel magnetic fields in their disks, for example NGC 253 (Heesen et al. 2009b; Krause 2012). Since the rotation curve of NGC 4631 rises nearly rigidly in the inner few kpc, Krause (2009) suggested that the differential rotation in this region might be too low to trigger a large-scale $\alpha - \Omega$ dynamo and thus there may be no amplification of the plane-parallel magnetic field in the disk. On the other hand, Drzazga et al. (2011) state that gravitational interactions may also modify galactic magnetic fields. Since NGC 4631 is gravitationally interacting with several of its companions, this might have caused a disturbance of its disk magnetic field.

Irwin et al. (2012a) already noticed in their 6 GHz EVLA observations, however, that the magnetic field along the plane of the galaxy appears to be parallel to the disk. Their observations unfortunately, have not been corrected for Faraday rotation. Therefore, it still remains unclear whether NGC 4631 has a unique magnetic field orientation in the central region of its disk. This is one of the questions we will address in this work. The parameters of NGC 4631 assumed throughout this study are presented in Table 2.1.

TABLE 2.1— Parameters of NGC 4631, as obtained from the literature.

Parameter	**Value**
Morphological type	SBcd
Dynamical Center[a]	$\alpha_{2000} = 12^{h}42^{m}08^{s}$ $\delta_{2000} = 32^{\circ}32'29''\!.4$
Inclination	86°
Position angle of major axis	85°
Assumed distance[b]	7.6 Mpc[c]

---

[a] IR center at 2.2 μm.

[b] from Seth et al. (2005), determined by the tip of the red giant branch method.

[c] $10''$ corresponds to 370 pc.

3

Observations and Data Reduction Techniques

"You see, wire telegraph is a kind of a very, very long cat.
You pull his tail in New York and his head is meowing in Los Angeles.
Do you understand this? And radio operates exactly the same way:
you send signals here, they receive them there.
The only difference is that there is no cat."
Albert Einstein

3.1 EVLA observations and calibration

Radio observations of NGC 4631 were taken with the Karl G. Jansky Very Large Array, hereafter called Expanded Very Large Array (EVLA), during its commissioning phase through the project *Continuum HAlos in Nearby Galaxies- an EVLA Survey (CHANG-ES)*. The CHANG-ES project is a new survey of 35 edge-on galaxies that is exploiting the new capabilities of the EVLA (Irwin et al. 2012a,b, 2013; Wiegert et al. 2015; Irwin et al. 2015). The data were taken at C-band at two array configurations, and L-band at three array configurations, making up a total of five data sets per galaxy. Thanks to the new wide-band receiver *WIDAR*, during the scheduled time for the CHANG-ES project the point source sensitivity had improved by about a factor of five with respect to Very Large Array (VLA) observations. At C-band the data covers 16 spectral windows (1024 spectral channels) for a total bandwidth of 2 GHz (4.979-7.021 GHz). At L-band the data covers 32 spectral windows (2048 spectral channels) for a total bandwidth of 512 MHz (1.247-1.503, 1.647-1.903 GHz). Due to strong interference between 1.503-1.647 GHz, a gap was introduced in the L-band frequency coverage. The wide-bandwidth provides us with richer spectral index information and with the possibility of applying RM-synthesis to study the Faraday space (see section 3.5). A summary of the observations of NGC 4631 are presented in Table 3.1.

TABLE 3.1— Details of the EVLA observations of NGC 4631.

Frequency Band	**C-band**		**L-band**		
Array configuration	**C**	**D**	**B**	**C**	**D**
Center Frequency	5.99 GHz		1.57 GHz		
Bandwidth [a]	2 GHz		0.5 GHz		
Spectral Resolution[b]	4 MHz		0.5 MHz		
Observing date	06/04/2012	29/12/2011	03/06/2012	02/04/2012	30/12/2011
Pointings	2[c]		1[d]		
Observing time[e]	6 hrs[f]	75 min[f]	2 hrs	77 min	18 min
Flux calibrator	3C286				
Phase calibrator	J1221+2813	J1310+3220	J1221+2813		
Polarization calibrator	OQ208	J1310+3220	OQ208		

---

[a] Bandwidth before flagging.

[b] After Hanning smoothing.

[c] Pointing 1: $\alpha_{2000} = 12^h42^m16.88^s$, $\delta_{2000} = 32^\circ32'37''.2$. Pointing 2: $\alpha_{2000} = 12^h41^m59.14^s$, $\delta_{2000} = 32^\circ32'21''.6$.

[d] Pointing: $\alpha_{2000} = 12^h42^m08.01^s$, $\delta_{2000} = 32^\circ32'29''.4$

[e] On-source observing time before flagging.

[f] Total time for both pointings.

For each observation at the specific frequency band and array configuration, NGC 4631 was observed within a scheduling block (SB) that included other galaxies as well. This allowed observations of NGC 4631 near the beginning of the SB and again near the end, so that the broadest possible coverage of the u,v plane could be achieved. The phase calibrator, which was located near the galaxy in the sky, was observed before and after the NGC 4631 scans. Observations also included a scan of a bright flux calibrator, which was 3C286 for all cases. This calibrator was also used as a bandpass calibrator as well as for the determination of the absolute polarization angle. At the end of the SBs, a scan was carried out on a calibrator that was known to have negligible polarization (OQ208 = J1407+2827), in order to calibrate the polarization leakage from the instrumentation. However, for the observation at C-band in the D array configuration, the polarization calibrator scans were lost so the calibrator J1310+3220 was used instead for this purpose.

Due to the large angular size of NGC 4631 on the sky and the size of the primary beam at C-band (7!5 FWHM), two pointings were necessary to fully observe the galaxy at this frequency band. Both pointings were located on either side of the center of the galaxy along the disk separated by 3!75. At L-band the diameter of the primary beam is $30'$, hence only one pointing was sufficient. The total intensity calibration for NGC 4631 was done as described in detail by Irwin et al. (2013), using the Common Astronomy Software Applications (CASA) package. In summary, the data were corrected for antenna-based delays when necessary (according to antenna position corrections) and were Hanning-smoothed to remove Gibbs ringing across the band caused by Radio Frequency Interference (RFI). The flux-density of the flux calibrator was defined using the Perley-Butler 2010 model and since each spectral window of each antenna has its own bandpass response, bandpass calibrations we performed using the flux calibrator. Phase and amplitude calibration tables we determined separately for each of the calibrators and then the solutions obtained with the phase calibrator were applied to the scans of NGC 4631 interpolated linearly in time. All data sets were flagged for RFI manually. Several tests were carried out implementing the automatic CASA flagging routines on the NGC 4631 data, however, we obtained better results with manual flagging.

For the polarization calibration a model of Stokes Q and U for the flux calibrator was introduced (Irwin et al. 2012a). According to this model, a curve of the following form was fit through the L-band data of 3C286:

$$P_\nu = -1.443 \cdot 10^{-6} \nu^2 + 60.26 \cdot 10^{-4} \nu + 3.858 \tag{3.1}$$

where P_ν is the percentage of polarization at a given frequency ν in MHz. At C-band a linear fit was implemented:

$$P_\nu = 15.83 \cdot 10^{-5} \nu^2 + 10.57 \tag{3.2}$$

Total errors for these models do not exceed 0.3% (Irwin et al. 2012a). To set Stokes Q and U for 3C286 the absolute position angle on the sky is assumed to be constant ($\psi = 33^\circ$), while the percentage of polarization varies as a function of frequency. Values for Stokes Q and U were then estimated at each spectral window (spw) according to:

$$\mathrm{Q}_\nu = (\mathrm{P}_\nu/100) \cdot \mathrm{I}\nu \cdot \cos(2\psi) \; ; \; \mathrm{U}_\nu = (\mathrm{P}_\nu/100) \cdot \mathrm{I}\nu \cdot \sin(2\psi) \tag{3.3}$$

where I_ν is the intensity of 3C286 according to the Perley-Butler 2010 model.

Since there is leakage between the right circularly polarized (R) and the left circularly polarized (L) feeds of the EVLA, this leakage must be accounted for in the calibration of Stokes Q and U[1]. Before this step, however, correction of antenna-based delays for the cross-hands (RL and LR) derived with the flux calibrator were

---

[1] Stokes Q and U are derived from the cross-hands: Q = (RL + LR)/2 ; U = (RL - LR)/2i.

applied when necessary. The polarization calibrator was used to estimate the leakage terms. For the C-band D array data set, the phase calibrator was used to determine the leakage terms, since its range in parallactic angle ($> 60^\circ$) permitted this. As Wiegert et al. (2015) conclude, there is no significant difference in the polarization calibration of our data whether the polarization calibrator or the phase calibrator is used. Finally, the absolute position angle on the sky (the R-L phase difference) was calibrated with the position angle of 3C286.

The polarization calibration applied corrects for ionospheric Faraday rotation, assuming it is constant with time and with position on the sky. It does not, however, correct for differential ionospheric Faraday rotation which varies with time and position. Irwin et al. (2012a) determined that the differential ionospheric Faraday rotation of their L-band observations varies at the high frequency end by 0.74° and at the low frequency end by 1.45°. This results in an average error introduced by differential ionospheric Faraday rotation of 1.1° at L-band. At C-band this error is even lower due to the frequency dependence nature of the Faraday effect.

The imaging of the data was executed with the CASA *clean* wide-field imaging algorithm (Cornwell 2008). During the imaging the u,v data is Fourier transformed into the image plane, creating what is known as the *dirty image*. This image is the convolution of the Fourier transform of the point-spread-function (psf) on the u,v plane (the *dirty beam*) with the source sky brightness distribution. This dirty beam is then deconvolved from the dirty image using the Clark algorithm (Clark 1980), which cleans in cycles and handles each Stokes plane separately. The wide-field imaging algorithm takes into consideration the effect that some EVLA antennas may not be coplanar since the array is sensitive to emission far from the pointing center.

TABLE 3.2— Image results with Briggs weighting (robust=0). All rms values extracted from non-PB corrected images. At C-band the rms was estimated from the mosaiced images.

Band	**C-band**		**L-band**		
Array configuration	**C**	**D**	**B**	**C**	**D**
Restoring beam	$2\farcs61 \times 2\farcs5$	$8\farcs88 \times 8\farcs57$	$3\farcs4 \times 3\farcs05$	$10\farcs13 \times 9\farcs9$	$34\farcs96 \times 32\farcs32$
rms noise in I [μJy/beam]	2.75	7.7	16	26	31
rms noise in Q/U [μJy/beam][a]	2.84	6.9	-	21	28

---

[a] Average noise from Stokes Q and U images.

Within the clean algorithm one can apply a multi-scale multi-frequency synthesis deconvolution (MS-MFS, Rau & Cornwell 2011) to image the data. The multi-scale setting assumes the emission can be modeled as a collection of components at a variety of spatial scales, hence, this setting is necessary to account for extended emission. By employing the multi-frequency synthesis technique measurements at multiple discrete frequencies are combined during imaging improving the u,v coverage. Since the EVLA now only observes in spectral line mode, i.e. it observes in narrow-band channels, bandwidth smearing is then only restricted to the spectral resolution of the data. For all images the Briggs robust weighting scheme (Briggs 1995) was used (robust=0).

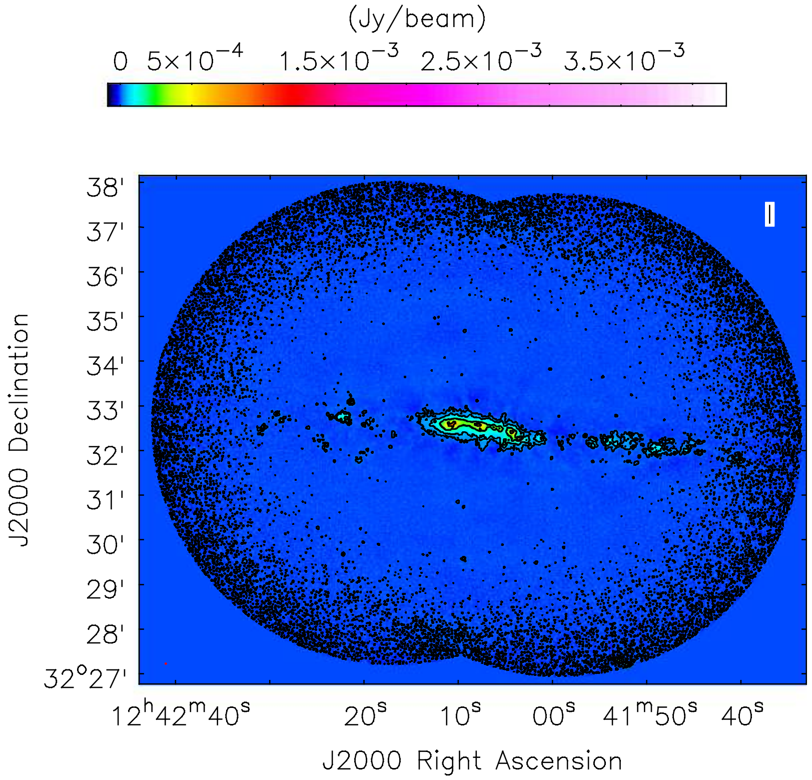

FIGURE 3.1— C-band (C array) total radio emission of NGC 4631. Angular resolution is $2.''61 \times 2.''5$. Contours correspond to: $4\ \mu\text{Jy/beam} \cdot (3, 12, 48, 192)$.

All data sets were self-calibrated once in both amplitude and phase, checking that the model to be used for self-calibration did not include any artifacts or any extended negative components. Different self-calibration approaches were tested, for instance a phase-only self calibration followed by an amplitude-only self-calibration. In addition, different solution intervals (*solint* parameter) were also experimented with iteratively to improve the self-calibration. Nevertheless, we obtained better results by applying only one self-calibration in amplitude and phase with a solution interval of 8 minutes. The self-calibration table made with the Stokes I image was then applied to the RL and LR data.

To emphasize broad scale structures at lower resolution, the u,v taper option within the cleaning algorithm was utilized. Varying the robust weighting for the total intensity images introduced artifacts in the images, so we decided to taper the visibilities instead. On the other hand, for Stokes Q and U better results were obtained by modifying the robust weighting in place of the u,v tapering alternative.

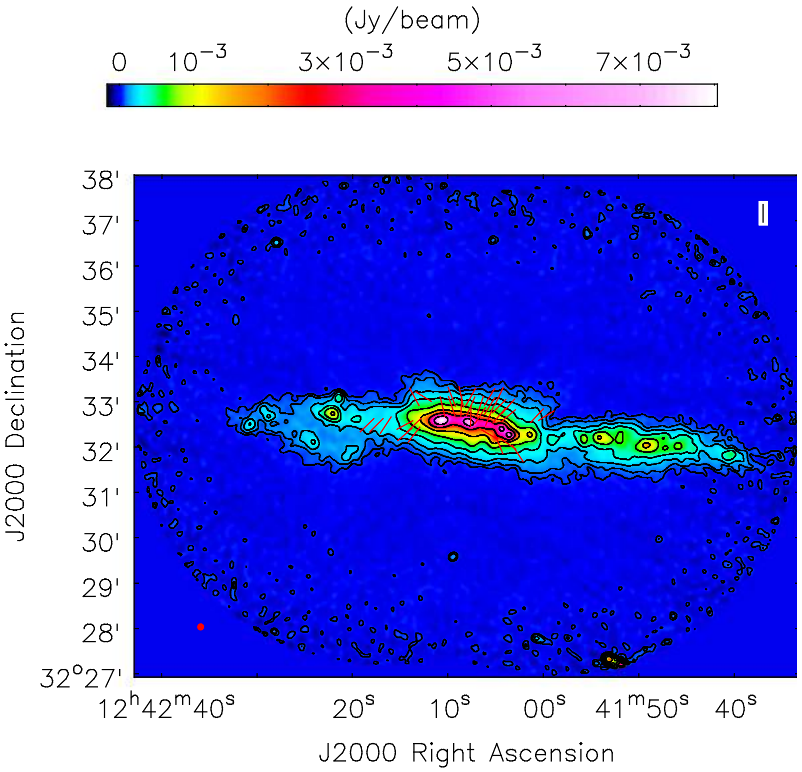

FIGURE 3.2— C-band (D array) total radio emission of NGC 4631 with apparent magnetic field vectors. Angular resolution is $8\overset{''}{.}88 \times 8\overset{''}{.}57$. Polarization vectors were cut at the 5σ level of Stokes Q/U. TP contours correspond to: 14 μJy/beam $\cdot$ $(3, 6, 12, 24, 48, 96, 192, 384)$.

To correct for the attenuation of the primary beam pattern (PB) of each of the antennae of the EVLA, it is necessary to apply a primary beam correction to the images. The CASA task *widebandpbcor* was utilized for this purpose. Since we are now dealing with wide-bandwidths, this task creates a PB cube with a model of the primary beam per frequency channel. However, the PB changes with position on the sky and it also rotates on the sky as the source is tracked. These effects can introduce significant errors with increasing distance from the pointing center. Therefore, a proper model of the PB that takes into account variations specific to a given observation must be developed. Wiegert et al. (2015) studied the potential errors introduced by this unrealistic model of the primary beam. They conclude that there can be significant errors already outside the 70% level of the PB.

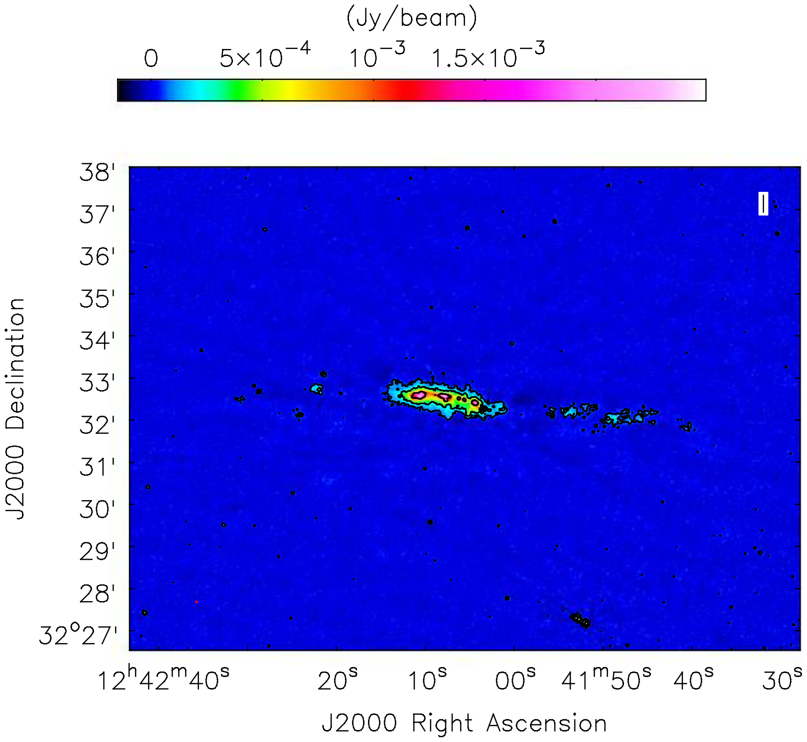

FIGURE 3.3— L-band (B array) total radio emission of NGC 4631. Angular resolution is $3''\!.4 \times 3''\!.05$. Contours correspond to: 24 μJy/beam $\cdot\,(3, 12, 48, 192)$.

At C-band, both pointings were self-calibrated and imaged separately. Consequently, widebandpbcor was executed separately on each of the corresponding Stokes I pointings. Then the non-PB corrected images for each pointing were combined in the overlapping regions by taking the weighted average out to 10% of the primary beam. The same combination on the image plane was performed for the two averaged primary beams obtained with widebandpbcor for each pointing. These averaged primary beams are created from the cube composed of the PB models. Finally, the primary beam correction was applied to the combined image by dividing by the combined primary beam.

The resolution and rms values of the resulting images are presented in Table 3.2. Total power (TP) emission at C-band is shown in figure 3.1 and 3.2. The vectors

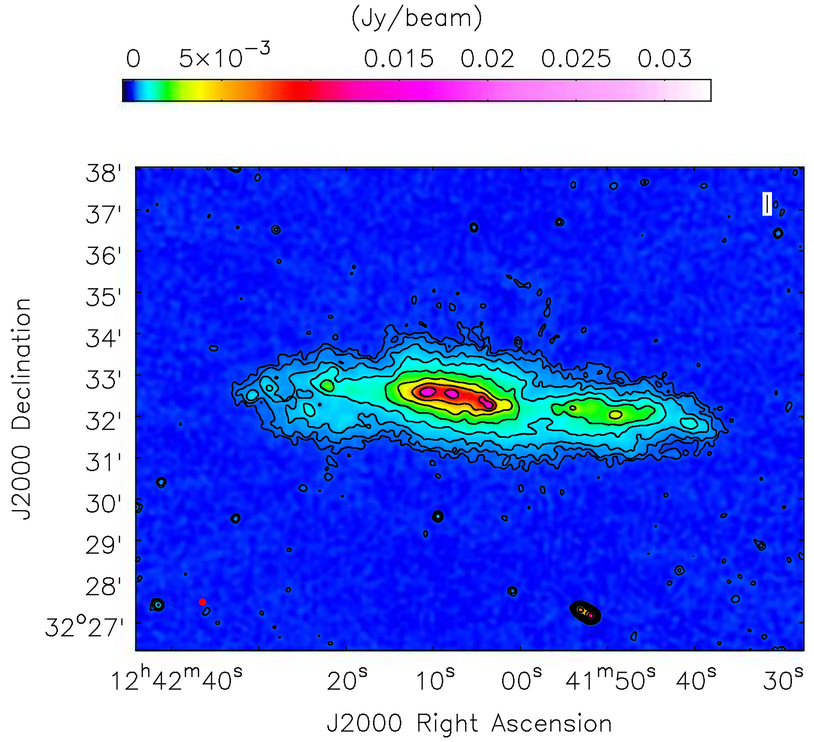

FIGURE 3.4— L-band (C array) total radio emission of NGC 4631. Angular resolution is $10\farcs13 \times 9\farcs9$. Contours correspond to: 30 μJy/beam $\cdot$ $(3, 6, 12, 24, 48, 96, 192, 384)$.

represent the observed electric field vectors[2] (E-vectors) rotated by 90°, and give the apparent magnetic field orientation in the sky plane since they have not been corrected for Faraday rotation (see Sect. 1.2.2). Currently, the CASA viewer does not have an option to vary the length of the vectors in the maps. Therefore, the vectors in each map have a constant length which was arbitrarily defined to ensure that the vectors can be well visualized. Total power emission at L-band is shown in figure 3.3, 3.4 and 3.5. In all of the maps presented, the beam-area is shown in red in the left-hand corner of each image. All radio images shown throughout this work have been PB-corrected unless stated otherwise.

3.2 Effelsberg observations and calibration

Observations of NGC 4631 with the 100 m Effelsberg telescope at 4.85 GHz (bandwidth = 0.5 GHz) were performed in 2014 with the dual-beam receiver (Project

---

[2] $\psi = (1/2) arctan(U/Q)$.

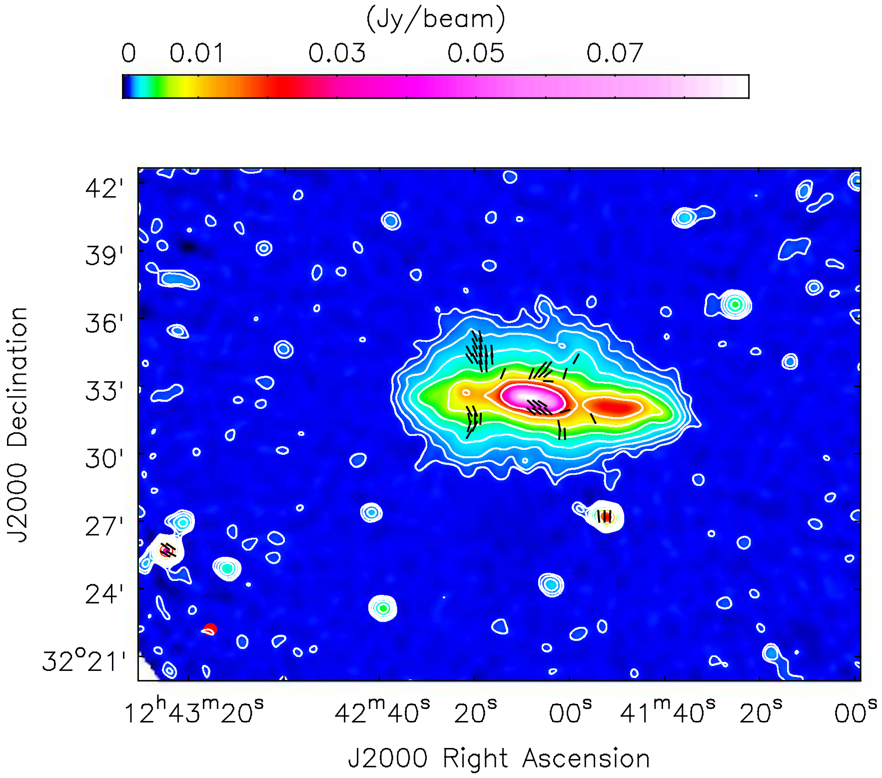

FIGURE 3.5— L-band (D array) total radio emission of NGC 4631 with apparent magnetic field vectors. Angular resolution is 34.″96 × 32.″32. Polarization vectors were cut at the 5σ level of Stokes Q/U. TP contours correspond to: 68 μJy/beam $\cdot$ $(3, 6, 12, 24, 48, 96, 192, 384)$.

114-13). A total of 20 coverages for all three Stokes parameters I, U, and Q were made of the $45' \times 35'$ scanned area, centered on the dynamical center of the galaxy (see Table 2.1). The data were reduced with the new NOD3 software package (Müller et al. in prep.), with which scanning effects due to weather conditions, receiver instabilities, and RFIs were removed. The scans of the galaxy were combined and flux calibration was done by using the radio source 3C286. We assume the 3C286 flux-density scale as measured by the NRAO[3]. The zerolevel of the maps in all Stokes parameters were corrected accordingly. The linear resolution of the maps is $146''$ FWHM and the rms noise values are 475 μJy/beam in total intensity and 142 μJy/beam in Stokes Q/U. The resulting emission is plotted in figure 3.6.

Excluding the background source to the southwest of the galaxy, the integrated

---

[3] `https://science.nrao.edu/facilities/vla/docs/manuals/oss/performance/fdscale`

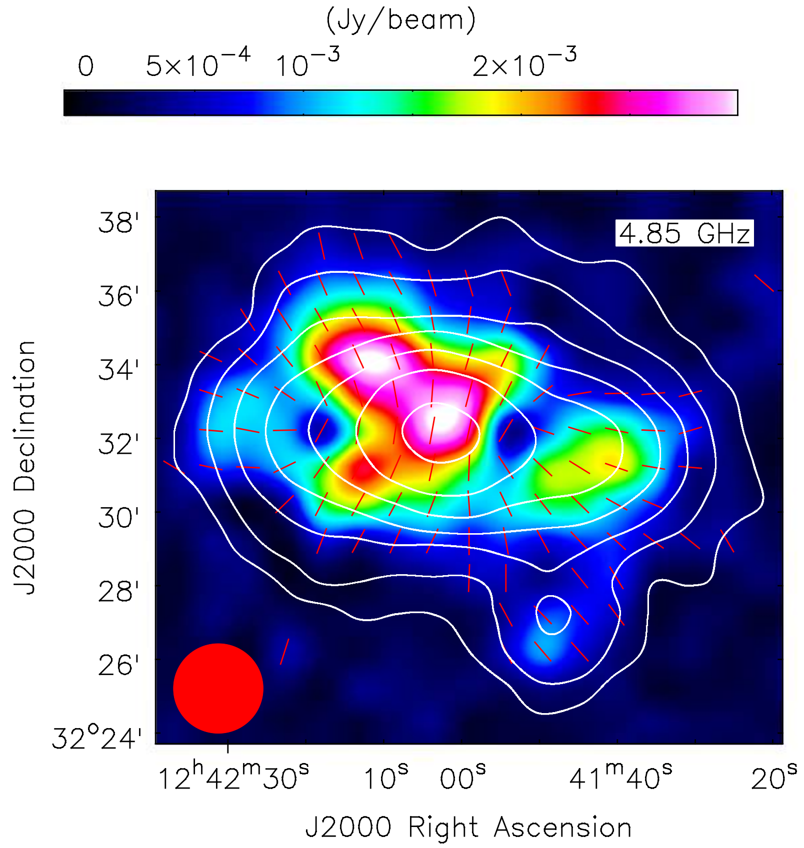

FIGURE 3.6— Effelsberg polarized emission of NGC 4631 over total intensity contours at 4.85 GHz, with apparent magnetic field vectors. Angular resolution is 146″. Total intensity contours correspond to **770** μJy/beam $\cdot$ (3, 6, 12, 24, 48, 96, 192).

flux-density of the total power emission of NGC 4631 at 4.85 GHz is of 484±29 mJy. To the uncertainties in the determination of the integrated flux-densities we have included the calibration and the zerolevel error. The estimated integrated flux-density at 4.85 GHz is a bit higher than the value obtained by Mora & Krause (2013) because we believe there was missing flux in their Effelsberg map, specially in the northwestern halo of the galaxy, caused by the limited size of their scanned area which makes it difficult to estimate a proper zerolevel.

Single dish observations with the Effelsberg telescope at 1.415 GHz (bandwidth = 0.13 GHz) were made with the single-horn receiver at excellent weather conditions in April 2002 (Project 43-02) centered on the dynamical center of NGC 4631. Approximately 16 coverages of all three Stokes parameters were taken, scanned in

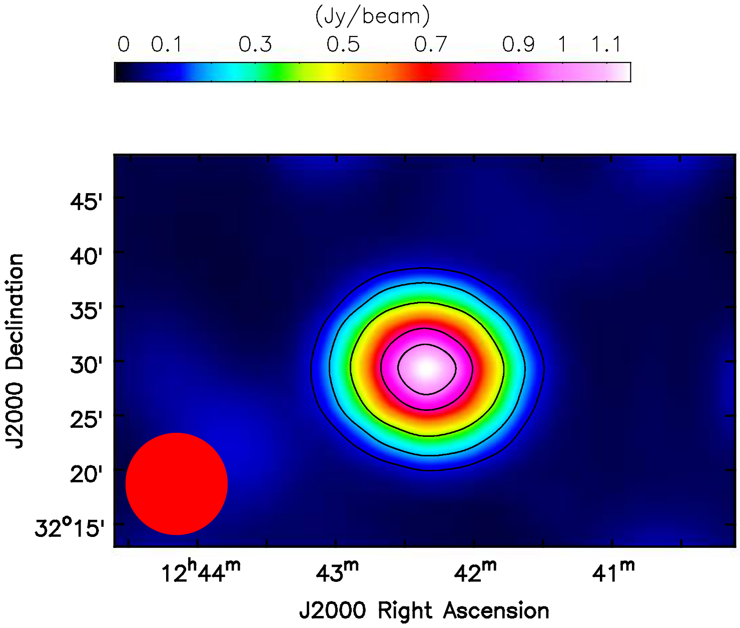

FIGURE 3.7— Effelsberg total radio emission at 1.415 GHz of NGC 4631. Angular resolution is 561″. Total intensity contours correspond to 33 mJy/beam · (3, 6, 12, 24, 30, 36).

two orthogonal directions to reduce scanning effects. The data were reduced with the NOD3 software package and flux calibration was done by using the radio source 3C286, assuming the flux-density scale measured by the NRAO. The zerolevel of the final maps in all Stokes parameters were adjusted accordingly. The linear resolution of the maps is 561″ FWHM, the rms noise values are 33 mJy/beam in total intensity and 5 mJy/beam in Q/U. The large size of the beam caused strong depolarization effects, therefore, we did not detect any polarization in NGC 4631 with these data. The total intensity is presented in figure 3.7. The integrated flux-density of the total power emission of the source observed at this frequency is of 1393±139 mJy. However, since the beam is so large this value overestimates the flux-density of NGC 4631 by roughly ∼50 mJy (which is still within the errors of the integrated flux-density), since it includes the flux of several point sources in the vicinity that we are able to measure in the interferometer data.

3.3 Integrated flux-densities and integrated total spectral index

In order to estimate the integrated flux-densities, the area of the galaxy within the 3σ level was integrated in ellipses. The corresponding values at each frequency band are

TABLE 3.3— Integrated flux-densities of NGC 4631 according to frequency band and telescope.

	Integrated flux-density [mJy]
EVLA C-band (5.99 GHz) D array	284 ± 11
Effelsberg 4.85 GHz	484 ± 29
EVLA L-band (1.57 GHz) D array	1091 ± 40
Effelsberg 1.415 GHz	1393 ± 139
ARO 0.835 GHz[a]	2005 ± 80
Effelsberg 2.68 GHz[b]	790 ± 40
Effelsberg 8.35 GHz [c]	310 ± 16
Effelsberg 10.55 GHz[d]	265 ± 12

---

[a] From (Israel & van der Hulst 1983).

[b] Werner (1984)

[c] From Mora & Krause (2013).

[d] From Dumke et al. (1995).

shown in Table 3.3. Fitting a power law of the form $I_{\nu,tot} \propto \nu^{\alpha_{tot}}$ we estimated the integrated total spectral index of the galaxy taking into account single-dish data only. In figure 3.8 the red solid line represents the best fit to the power law, resulting in a total spectral index of $\alpha_{\rm tot} = -0.81 \pm 0.03$. Within the errors the integrated spectral index agrees with that published by Hummel & Dettmar (1990) and Mora & Krause (2013).

The flux-densities presented in Table 3.3 demonstrate the interferometer data has missing spacings even in its most compact configuration. Therefore, it is necessary to combine the Effelsberg and EVLA data to recover the missing flux attributed to the incomplete u,v coverage of the interferometer.

3.4 Merging EVLA and Effelsberg total intensity images

3.4.1 Rescaling of the Effelsberg data

To combine the images one must first scale the single-dish and interferometer data to the same central frequency. The Effelsberg data at 4.85 GHz was rescaled to the flux it would have at 5.99 GHz by fitting the spectral index distribution between Effelsberg data at 8.35 GHz and 4.85 GHz on a pixel-by-pixel basis. The Effelsberg data at 8.35 GHz were available through Mora & Krause (2013). The galaxy has an integrated flux-density at 5.99 GHz given by the Effelsberg rescaled map of 398±24 mJy.

The Effelsberg data at 1.415 GHz was rescaled to 1.57 GHz by assuming a constant

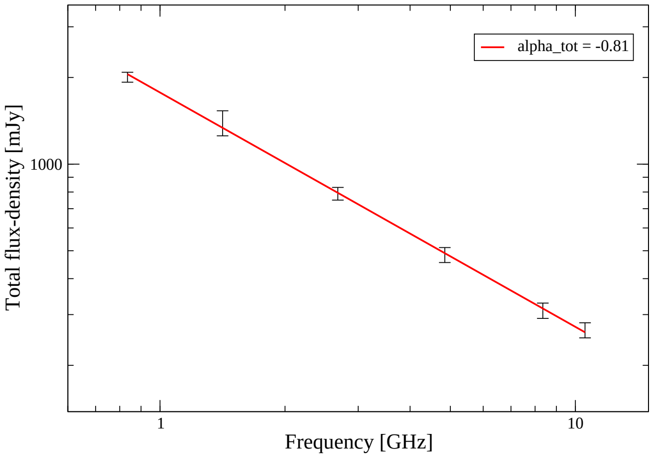

FIGURE 3.8— Integrated radio spectrum of the total emission of NGC 4631. The red solid line shows the best-fit power law, with a total spectral index of $\alpha_{\rm tot} = -0.81 \pm 0.03$. Only single-dish data was taken into account for this calculation.

spectral index of $\alpha_{\rm tot} = -0.81$. Attempts were made to fit a spectral index distribution between the Effelsberg map at 4.85 GHz (smoothed to $561''$) and the 1.415 GHz data. However, due to the poor resolution no coherent structures could be resolved so we decided to assume an integrated spectral index instead. NGC 4631 has an integrated flux-density at 1.57 GHz of 1285 ± 129 mJy, determined by the Effelsberg map rescaled to this frequency. Due to the low resolution of the data, this value represents an upper limit to the flux-density of the galaxy since it includes the contribution of several point sources located near to NGC 4631. We believe these point sources contribute by roughly ~ 45 mJy at this frequency.

3.4.2 Merging strategy

The Effelsberg and the EVLA data at 5.99 GHz were merged on the image plane with the new NOD3 algorithm *ImMerge* (Müller et al. in prep.). This algorithm combines both images by first creating a difference map by subtracting from the single-dish image the interferometer fluxes smoothed to the resolution of the single-dish beam. This difference map in then rescaled by the ratio of the two beams involved and consequently added with the interferometer image at the original resolution. Before combining the Stokes I images, however, they were brought to the same grid and the Effelsberg map was checked for any pointing errors. The total intensity image obtained by combining the Effelsberg and EVLA data is presented in figure 3.9. By combining the Effelsberg and EVLA images we recovered the missing flux attributed to the large-scale structures which contributes by about 27% to the total flux of the galaxy. The resulting integrated flux-density of NGC 4631 in the combined image is of 391±20 mJy.

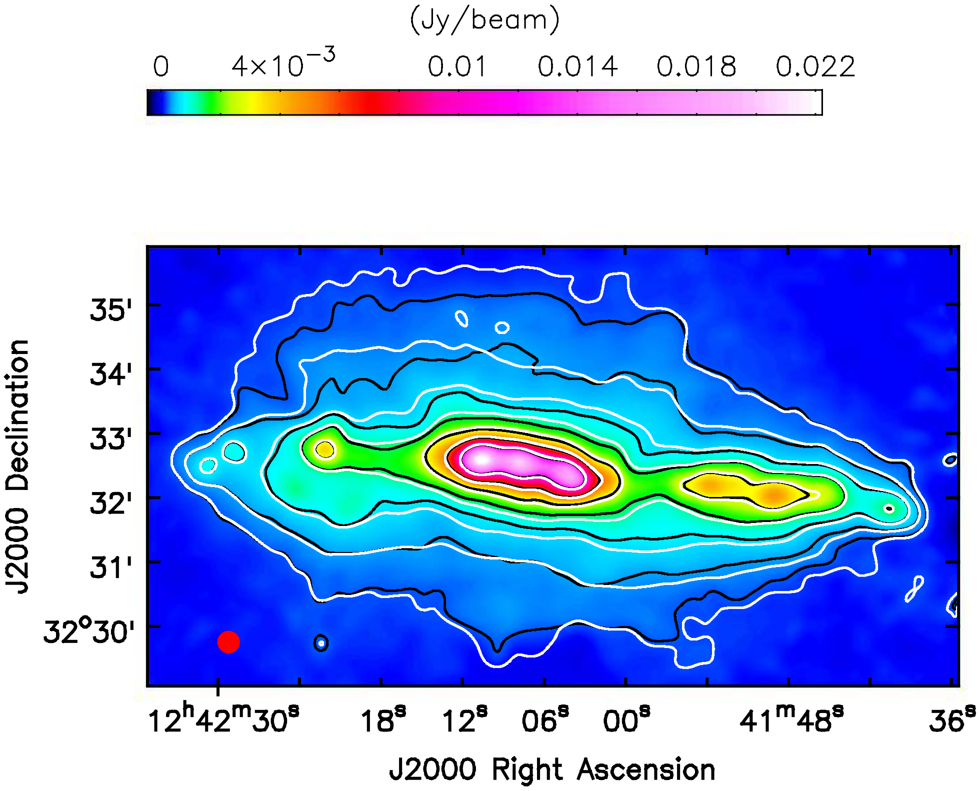

FIGURE 3.9— Merged (D array + Eff.) total power emission of NGC 4631 at 5.99 GHz. Black contours correspond to the image combined with the *ImMerge* algorithm in NOD3. White contours correspond to the image merged in AIPS with the *IMERG* task. Both images have an angular resolution of 20.″5. The colorscale is given by the merged image in NOD3. Both white and black contours levels are determined by: 60 μJy/beam $\cdot\,(3, 6, 12, 24, 48, 96, 192, 384)$

To compare the merged result we also tested combining the single-dish and interferometer data with the the Astronomical Image Processing System (AIPS) task *IMERG*. The main difference between *ImMerge* and the AIPS task is that the first combines the data in the image domain while the latter performs the combination in the spatial-frequency plane. The AIPS task Fourier transforms the high and low-resolution images into the u,v plane. Then it deconvolves the single-dish image and subsequently convolves it with the interferometer beam. The low-resolution visibilities are rescaled to the amplitudes of the high-resolution image and afterwards they are combined with the interferometer visibilities. Finally, the AIPS task transforms back the combined visibilities into the image plane. The merged Stokes I image of NGC 4631 at 5.99 GHz obtained with the AIPS task is shown in white contours in figure 3.9. This image has an integrated flux-density of 406±20 mJy. The most noticeable difference between the two combined images is that the result obtained with AIPS is more extended towards the northeast and southwest with respect to the combined image obtained with ImMerge, giving the galaxy a more asymmetric distribution in its halo. The asymmetry in the northern halo of NGC 4631 is even more pronounced in the 4.85 GHz combined map published by Mora & Krause (2013) because these authors combined their data with the AIPS algorithm and in addition, due to the considerable missing flux in their Effelsberg 4.85 GHz data in the northwestern area of the galaxy. Since radio continuum observations of most of the edge-on galaxies studied up to now reveal a more symmetric distribution of the halo emission, we believe that the ImMerge algorithm in more accurate in this respect. In addition, if we combine the data with the new CASA task *Feather*, we obtain a similar result to that of ImMerge. Therefore, all of the combined data presented throughout this work was merged with the NOD3 task.

The same procedure was followed to combine the single-dish and interferometer images at 1.57 GHz with the ImMerge task in NOD3. The total intensity image obtained by combining the Effelsberg and EVLA data at 1.57 GHz is shown in figures 4.2 and 4.4. The resulting integrated flux-density of the galaxy in the combined image is of 1232±84 mJy.

3.5 Rotation Measure Synthesis Technique

The Rotation Measure Synthesis Technique (RM-synthesis) is based on the theoretical description of Burn (1966). It was later developed by Brentjens & de Bruyn (2005); de Bruyn & Brentjens (2005) to recover extended polarized emission in the Perseus cluster. There are several publications that demonstrate and extend the effectiveness and importance of this technique, for instance Heald et al. (2009); Pizzo et al. (2011); Schnitzeler & Lee (2015).

Following Burn (1966), the Faraday depth, ϕ, of a source is defined as:

$$\phi(l)\ [rad \cdot m^{-2}] = 0.81 \int_{there}^{here} n_e \vec{B}\, d\vec{l} \tag{3.4}$$

where n_e is the electron density in cm^{-3}, and $\vec{B}$ is the magnetic field (in μG) along the line-of-sight $\vec{l}$ (in parsecs). The classical RM definition (section 1.2.2) and the Faraday depth are equivalent only when there is only one background source along the

LOS (which has no internal Faraday rotation) with a dispersive Faraday screen in the foreground. In the case when the RM is equivalent to the Faraday depth, equation 1.12 can be rewritten as $\psi(\lambda^2) = \psi_0 + \phi\lambda^2$. A more realistic scenario, however, consists of multiple emitting plasmas along the LOS, but then the classical RM definition is no longer valid. The concept of Faraday depth is more general, and with the proper resolution in Faraday space one can identify several polarized sources along the LOS.

According to Burn (1966), the monochromatic complex polarization vector is equal to:

$$P(\lambda^2) = \int_{-\infty}^{\infty} pI \, \exp(2i[\psi_0 + \phi\lambda^2])\mathrm{d}\phi \tag{3.5}$$

where p is the fractional polarization. The term pI is equal to $Q + iU$. Introducing the Faraday dispersion function, $F(\phi)$, equation 3.5 takes the form of a Fourier transformation:

$$P(\lambda^2) = \int_{-\infty}^{\infty} F(\phi) \, \exp(2i\phi\lambda^2)\mathrm{d}\phi \tag{3.6}$$

The function $F(\phi)$ is known as the *Faraday spectrum* or the *Faraday dispersion function*. Since there are no negative wavelengths and the bandwidth of all telescopes is limited, equation 3.6 has no solution. However, Brentjens & de Bruyn (2005) approached this problem by introducing a sampling function $W(\lambda^2)$, which represents the bandwidth of the telescope. This weighting function is nonzero at all λ^2 values where measurements are taken and 0 where there is no sampling. Including the sampling function, equation 3.6 becomes:

$$\widetilde{P}(\lambda^2) = W(\lambda^2)P(\lambda^2) = W(\lambda^2)\int_{-\infty}^{\infty} F(\phi) \, \exp(2i\phi[\lambda^2 - \lambda_0^2])\mathrm{d}\phi \tag{3.7}$$

With this equation one can derive the reconstructed Faraday spectrum:

$$\widetilde{F}(\phi) = K\int_{-\infty}^{\infty} \widetilde{P}(\lambda^2)\exp(-2i\phi[\lambda^2 - \lambda_0^2])\mathrm{d}\lambda^2 = \mathrm{F}(\phi)\star\mathrm{R}(\phi) \tag{3.8}$$

where K is one divided by the integral over $\mathrm{W}(\lambda^2)$ and "$\star$" denotes convolution. The function $R(\phi)$ is called the *RM Spread Function (RMSF)* which represents the response of the instrument, it is the equivalent of the point spread function when imaging a part of the sky. The RMSF is defined as:

$$R(\phi) = K\int_{-\infty}^{\infty} W(\lambda^2)\exp(-2i\phi[\lambda^2 - \lambda_0^2])\mathrm{d}\lambda^2 \tag{3.9}$$

Since our measurements are sampled in discrete frequency channels, equations 3.8

and 3.9 can be written as the following sums[4]:

$$\widetilde{F}(\phi) \approx K \sum_{i=1}^{N} \widetilde{P}_i \exp(-2i\phi[\lambda_i^2 - \lambda_0^2]) \tag{3.10}$$

$$R(\phi) \approx K \sum_{i=1}^{N} W(\lambda_i^2) \exp(-2i\phi[\lambda_i^2 - \lambda_0^2]) \tag{3.11}$$

$$K = \left(\sum_{i=1}^{N} W(\lambda_i^2) \right)^{-1} \tag{3.12}$$

Since each channel is imaged separately in Stokes Q and U, applying RM-synthesis to this 3D data cube (two coordinate axes and one frequency axis) leads to another 3D data cube with two coordinate axes (right ascension and declination) and a third axis determined by the Faraday depth.

The finite frequency band produces an RMSF with sidelobes, in a similar way to how the sidelobes of the telescope's psf (synthesized beam) in aperture synthesis observations originate. However, since the RMSF is well known, it is possible to deconvolve the Faraday depth spectrum. Therefore, these artifacts can be reduced. This is done with the deconvolution routine called *RM clean* (Heald et al. 2009). This algorithm searches for peaks in the Faraday spectrum and then subtracts an RMSF at their location. Consequently, the algorithm reconstructs the Faraday spectrum employing a Gaussian with the same FWHM as the RMSF.

When analyzing the Faraday depth cubes, it is important to keep in mind the following properties that are specific to any given observation. The maximum resolution in Faraday space one can achieve is given by the FWHM of the RMSF:

$$\delta\phi \approx \frac{2\sqrt{3}}{\Delta\lambda^2} \tag{3.13}$$

In addition, the largest scale in ϕ space to which one is sensitive:

$$scale_{max} \approx \frac{\pi}{\lambda_{min}^2} \tag{3.14}$$

Hence, if λ_{min}^2 is too large, sources which are extended in Faraday space will be observed as individual peaks. This is similar to the missing spacings problem in aperture synthesis. The maximum Faraday depth to which one has more than 50% sensitivity is determined by:

$$\| \phi_{max} \| \approx \frac{\sqrt{3}}{\delta\lambda^2} \tag{3.15}$$

---

[4] This requires that $\phi\delta\lambda^2 \ll 1$ (Brentjens & de Bruyn 2005), but (Schnitzeler & Lee 2015) showed that this condition can be relaxed considerably.

where $\delta\lambda$ is the width of an individual channel. According to Brentjens & de Bruyn (2005), in order to resolve Faraday thick sources in ϕ space so that one can distinguish internal structure, the main peak of the RMSF should be narrower than the maximum scale to which one is sensitive, i.e. $\lambda_{min}^2 < \Delta\lambda^2$. For our C-band observations, the maximum resolution in Faraday space we can achieve is $\delta\phi \approx 2065\,\mathrm{rad\cdot m^{-2}}$ and the maximum scale detectable is $scale_{max} \approx 1691\,\mathrm{rad\cdot m^{-2}}$. For the L-band observations, our maximum resolution in Faraday space is $\delta\phi \approx 107\,\mathrm{rad\cdot m^{-2}}$ and the maximum scale we can detect is $scale_{max} \approx 126\,\mathrm{rad\cdot m^{-2}}$.

To apply RM-synthesis to our EVLA data taken at C-band the self-calibrated visibilities were imaged per spectral window in Stokes Q and U employing the multi-scale deconvolution available in CASA. Multi-frequency synthesis is not necessary in this case since we are not imaging the entire band. Both pointings were mosaiced during the cleaning routine and Briggs robust weighting was applied in such a way that all images have the same angular resolution determined by the synthesized beam of the lowest central frequency. During the cleaning procedure the classical primary beam correction was applied automatically (not the wide-bandwidth PB-correction). Each of the images for Stokes Q and U were stacked into a cube and RM-synthesis was performed followed by the RM clean deconvolution.

For the L-band data a similar procedure was followed, but in this case the self-calibrated visibilities were imaged per channel since at higher frequencies the electric field vector rotates more rapidly and therefore, bandwidth depolarization is more severe. Each image was inspected for artifacts and any image contaminated with RFIs was discarded. The corresponding results are presented in chapter 6.

4

Analysis of the Total Radio Emission

> *“ A few years ago, the city council of Monza, Italy, barred pet owners from keeping goldfish in curved bowls... saying that it is cruel to keep a fish in a bowl with curved sides because, gazing out, the fish would have a distorted view of reality. But how do we know we have the true, undistorted picture of reality?”*
>
> Stephen Hawking

4.1 Comparison with other wavebands

The total radio emission of NGC 4631 at C-band is presented in figure 4.1 at a resolution of $2\overset{''}{.}7$ together with the Hα radiation of the galaxy. Contours of the C-band emission are displayed over the L-band radiation of the galaxy at an angular resolution of about $34''$ in figure 4.2. In addition, NGC 4631 is shown at L-band at a resolution of $10\overset{''}{.}13 \times 9\overset{''}{.}9$ in figure 4.3 overlayed on an optical image of the galaxy. The L-band emission is also depicted in figure 4.4 at a resolution of $15''$ in combination with the soft X-ray emission of the galaxy, and at a resolution of $35''$ in figure 4.5 over the HI emission.

A close-up view of the central region of NGC 4631 is shown in figure 4.1, Hα contours were overlayed on a colorscale of the total C-band emission. The Hα worms discovered by Rand et al. (1992) have been labeled “A”, “B” and “C”. These worms of Hα radiation have tentatively been considered as evidence that the central region is in a *chimney mode* (Norman & Ikeuchi 1989), wherein an expanding hot superbubble caused by a central starbust shocks dense gas in the galactic disk and in consequence, hot gas flows into the halo through the so-called chimneys. The worms can also be

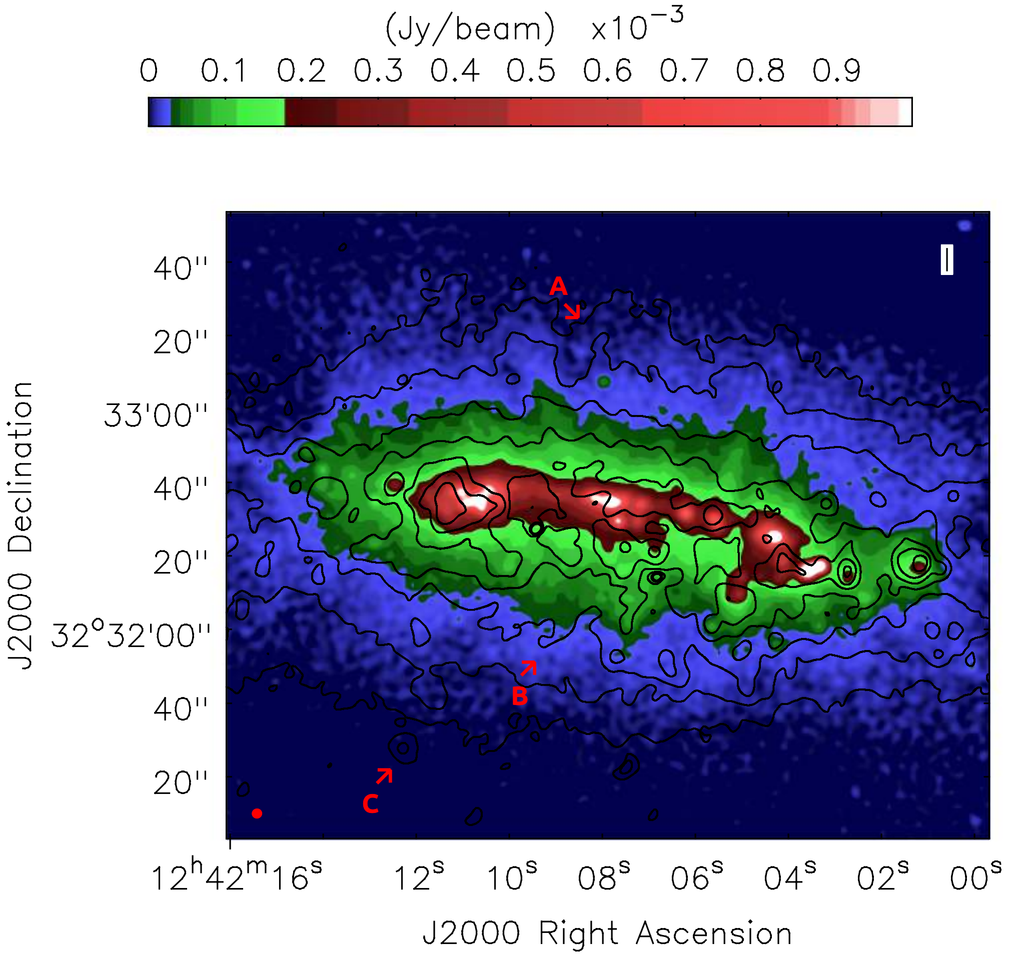

FIGURE 4.1— Colorscale of the total radio emission at C-band (D&C array) together with contours of the Hα emission. All data plotted has an angular resolution of 2.″7 FWHM. Contour levels of the Hα emission correspond to 4.5 μJy/beam $\cdot$ (3, 6, 12, 24, 48, 96, 192, 384). Hα data from Kennicutt et al. (2003). Hα worms have been labeled “A”, “B” and “C”.

traced in the total radio emission, as demonstrated in figure 4.1. The most obvious correlation is seen for the double-worm feature labeled “A”. The emission at L-band in the B array configuration is very similar to what is seen at C-band at high resolution (cf. fig 3.1 and 3.3), hence we refrain from showing it here.

As has already been pointed out by Golla & Hummel (1994), in the central region of the galaxy there is no clear coincidence between the radio peaks and the Hα complexes, as opposed to the outer parts of the disk (cf. fig. 5.1). This is probably due to dust attenuation and we will show in Chapter 5 that the central region has the largest level of extinction within the galaxy. The bright radio source to the southwest of the central region at $\alpha_{2000} = 12^h42^m03.5^s, \delta_{2000} = 32^\circ32'16.''5$, was identified by Golla (1999) as a possible background radio galaxy. In section 4.4 we discuss this feature together with another background radio galaxy to the south of NGC 4631.

The molecular emission also has strong correlation with the radio emission observed in the disk. The central radio radiation has a very bright molecular counterpart seen in the CO(J=3-2) emission, the *central molecular ring* as referred to by Irwin et al. (2011). In addition, the molecular emission in the outer parts of the disk also coincides with peaks seen in the radio. The extended molecular region in the western side of NGC 4631, *the kink*, coincides with the radio emission seen at position $\alpha_{2000} = 12^h41^m50^s; \delta_{2000} = 32^\circ32'$, and the eastern molecular *bulge* (Irwin et al. 2011) coincides with the radio peak in the eastern side of the galaxy at coordinates $\alpha_{2000} = 12^h42^m22^s; \delta_{2000} = 32^\circ32'45''$.

The known asymmetries of the emission of NGC 4631 can be seen at L-band and C-band in figure 4.2. The northern halo seems to have a larger z-extent than the southern halo. In addition, with respect to the center of the galaxy, the radio emission along the disk extends more to the west than to the east. These asymmetries have also been observed at other wavelengths, for instance at λ 2.8 cm (Dumke et al. 1995), at λ 3.6 cm (Mora & Krause 2013), at λ 18 and 22 cm (Heald et al. 2009), and also in the HI emission (Rand 1994).

Figure 4.3 displays at high resolution the prominent northwestern radio spur (hereafter denoted as *NW-radio spur*) that was discovered by Ekers & Sancisi (1977). The northeastern radio spur (*NE-radio spur*) and the southeastern radio spur (*SE-radio spur*) indicated by Hummel & Dettmar (1990) are also distinguished in this figure in much better detail at higher resolution. These spurs, however, seem to have counterparts at C-band only at low resolution $\sim 34''$ (cf. figure 4.2). Golla & Hummel (1994) speculate the NW-radio spur originates close to the eastern peak of the central triple source, but in our data (which is at higher resolution) this spur is clearly distinguishable only $1'.5$ above the plane ($\sim$ 3.3 kpc). At L-band the NW-radio spur bends towards the northeast at more or less the projected position of the companion dwarf galaxy and it can be traced up to about $3'.3$ ($\sim$7.4 kpc) above the center of the galaxy.

The X-ray emission of NGC 4631 is shown as a colorscale in figure 4.4 together with contours of the L-band emission. According to (Wang et al. 1995), the bright soft X-ray emission in the upper half of the galaxy appears to be confined within the northern radio spurs, it has been suggested that the magnetic field could be responsible for preventing this hot gas from flowing out of the galaxy (Wang et al. 1995; Irwin et al. 2011).

The HI emission of NGC 4631 is shown as a colorscale in figure 4.5 and the HI

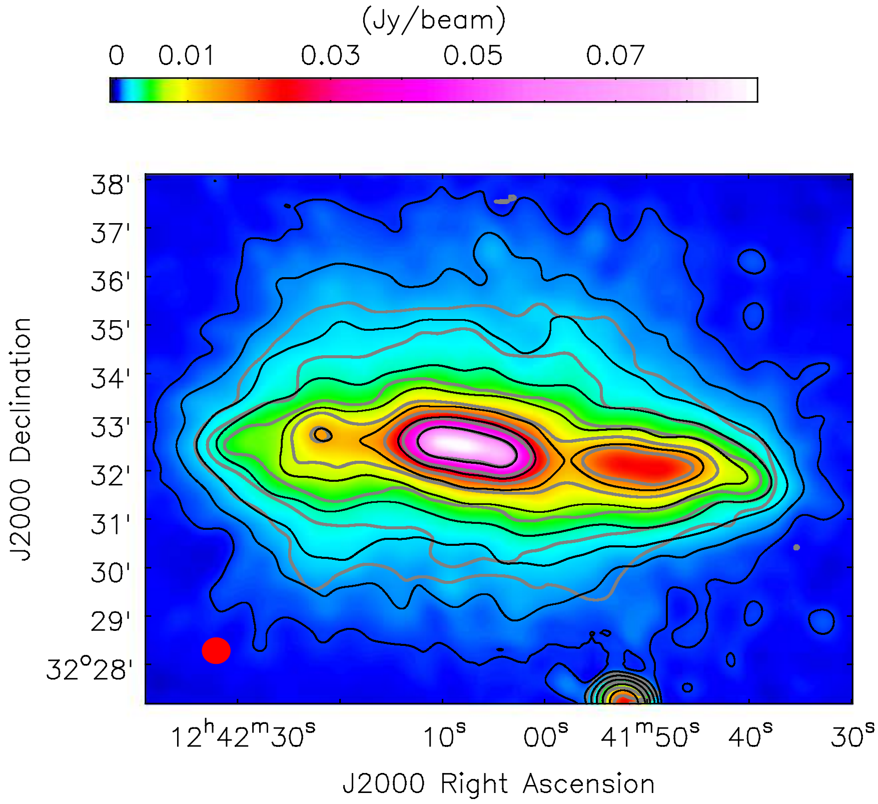

FIGURE 4.2— Colorscale of the total L-band emission (EVLA + Eff.) of NGC 4631 together with contours of the C-band radiation of the galaxy. Angular resolution is $34.''96 \times 32.''32$. Grey contours correspond to the C-band emission (EVLA + Eff.): 115 μJy/beam $\cdot$ $(3,6,12,24,48,96,192,384)$. Black contours correspond to the L-band emission (EVLA + Eff.): 140 μJy/beam $\cdot$ $(3,6,12,24,48,96,192,384)$.

spurs discovered by Weliachew et al. (1978) have been labeled 1-4. The projected length of the HI spurs 1, 2 and 4 is about 61 kpc, while spur 3 has an apparent length of 31 kpc (Rand 1994). The L-band emission displays correlation with the HI radiation, the radio emission seems to "follow" the HI spurs 2 and 4. The SE-radio spur appears to be the radio counterpart of the HI spur 2. In addition, the uppermost emission of the NW-radio spur is oriented towards the northeast in the same manner as the HI spur 4.

The radio disk also shows some correlation with the disk seen in HI (cf. our fig. 4.3 with fig. 6 of Rand 1994). Both the central and western radio concentrations in the disk have HI counterparts. With respect to the dwarf elliptical companion NGC 4627, there is radio emission that coincides with the position of the galaxy, however, no

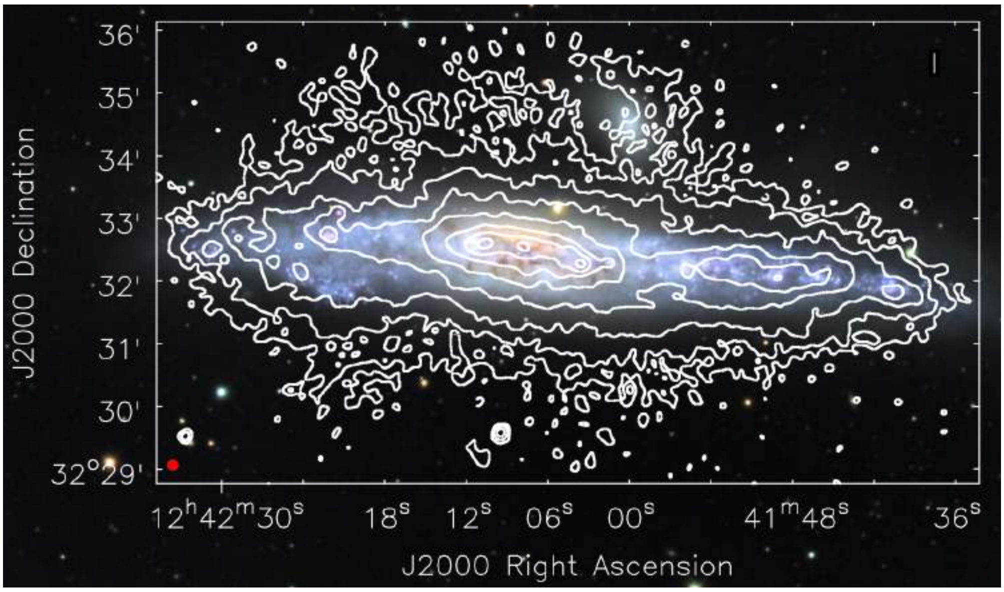

FIGURE 4.3— Total radio emission at L-band (D&C array) overlayed on an optical DSS image (blue band). Angular resolution is $10.''13 \times 9.''9$ FWHM. Contour levels of the L-band emission correspond to 38 μJy/beam $\cdot (3,6,12,24,48,96,192,384)$.

radiation can be unambiguously associated with the galaxy. Rand (1994) came to the same conclusion for the HI distribution.

4.2 Vertical scale heights

The observed brightness distribution of an edge-on galaxy is the result of its z-extent projected onto the plane of the sky with an inclination effect and a smearing effect caused by the beam. Since NGC 4631 is not seen perfectly edge-on, the disk emission is projected unto the halo. Therefore, to simulate this effect we have to take into account the inclination of the galaxy and the telescope beam by introducing an *effective beam*. The effective beam was determined by projecting a circular intensity distribution of the size of the disk of NGC 4631 to the inclination of the galaxy of 86°. This distribution was then convolved with a Gaussian function with a FWHM matching the resolution of the map to simulate the effect of the telescope beam. The effective beam is then the FWHM of the resulting distribution. The extraplanar emission is characterized as the emission that exceeds this effective beam size from the major axis.

The vertical scale heights were estimated from emission profiles that were obtained by flux integration along strips perpendicular to the major axis of the galaxy. These

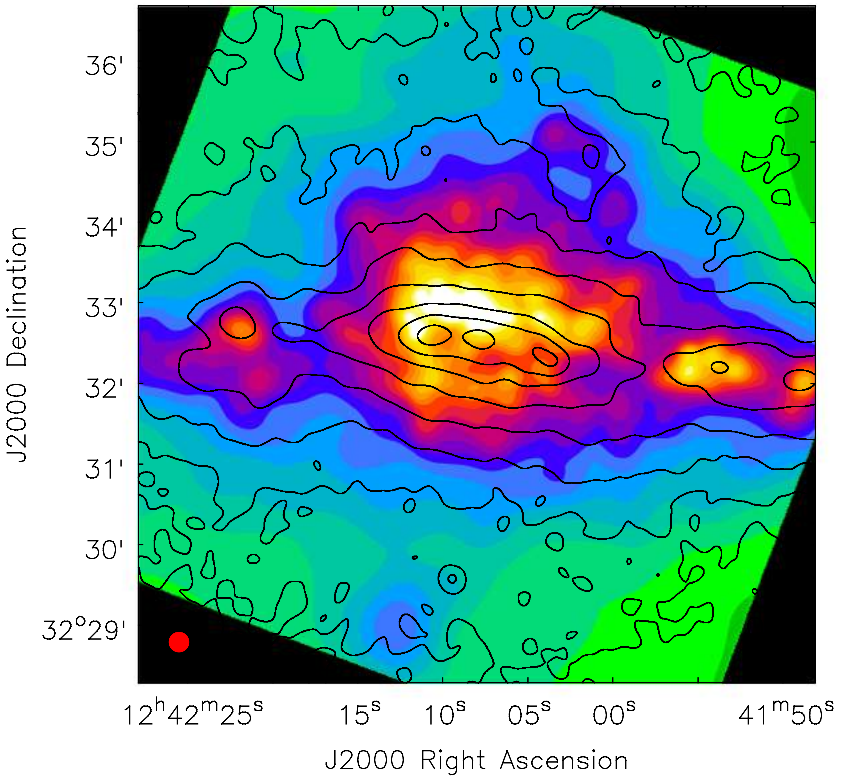

FIGURE 4.4— Total radio emission at L-band (EVLA + Eff.) over a colorscale of the soft X-ray emission. Angular resolution is 15″ FWHM. Contour levels of the L-band emission correspond to 60 μJy/beam $\cdot\,(3,6,12,24,48,96,192,384)$. X-ray data from Wang et al. (2001).

profiles were fitted with a model distribution consisting of an exponential convolved with the effective beam. Following Sievers (1988), an exponential distribution convolved with a Gaussian function takes the form:

$$\begin{aligned} W_{exp}(z) \;=\; & \frac{w_0}{2}\exp\left(-\frac{z^2}{2\sigma^2}\right)\cdot \\ & \left[\exp\left(\frac{\sigma^2-z\cdot z_0}{\sqrt{2}\sigma z_0}\right)^2 \mathrm{erfc}\left(\frac{\sigma^2-z\cdot z_0}{\sqrt{2}\sigma z_0}\right)+\exp\left(\frac{\sigma^2+z\cdot z_0}{\sqrt{2}\sigma z_0}\right)^2 \mathrm{erfc}\left(\frac{\sigma^2+z\cdot z_0}{\sqrt{2}\sigma z_0}\right)\right] \end{aligned} \tag{4.1}$$

where σ is the effective beam size, w_0 the maximum of the distribution, z_0 the scale height and the complementary error function:

$$\mathrm{erfc(x)} = 1-\mathrm{erf(x)} = \frac{2}{\sqrt{\pi}}\int_{\mathrm{x}}^{\infty}\exp(-\mathrm{r}^2)\mathrm{dr} \tag{4.2}$$

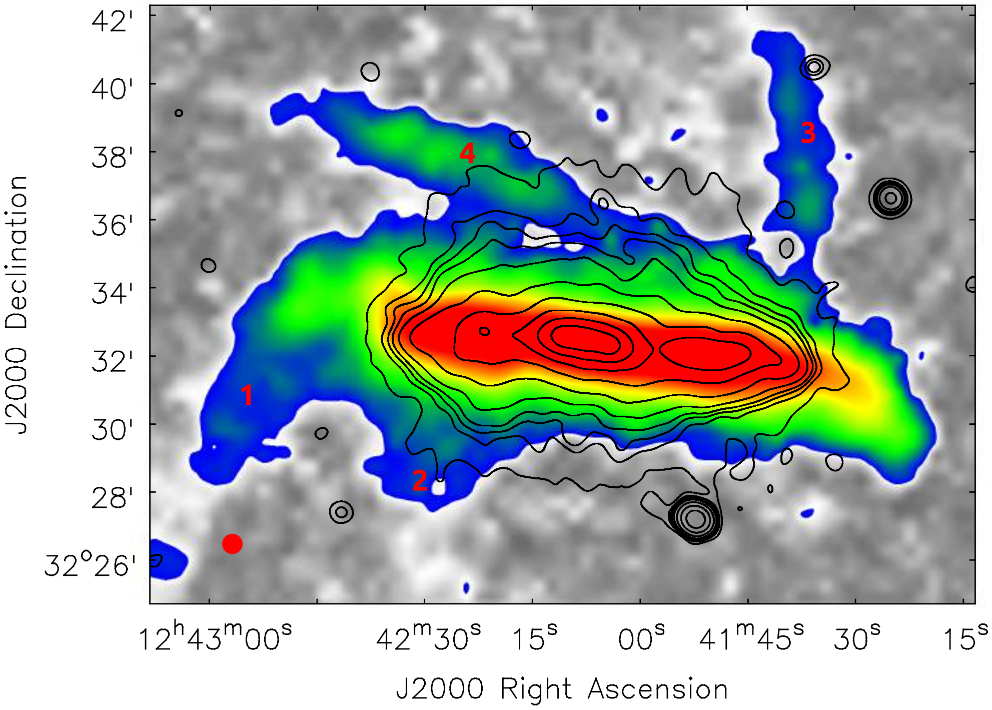

FIGURE 4.5— Total radio emission at L-band (EVLA + Eff.) over a colorscale of the HI radiation. All data plotted has an angular resolution of 35″ FWHM. Contour levels of the L-band emission correspond to 140 μJy/beam $\cdot$ $(3, 6, 8, 10, 14, 24, 48, 96, 192, 384)$. HI data from Rand (1994). HI spurs have been labeled 1-4.

The vertical scale heights were determined at C-band and at L-band at an angular resolution of 15″ (EVLA + Eff.). Since the radio distribution of NGC 4631 is known to have a north-south asymmetry, the profiles of the emission above and below the disk midplane were fitted separately. Flux integration was estimated along three strips parallel to the minor axis with a width of 180” each, centered on the nucleus, in order to analyze the radio spurs in the eastern and western side of the galaxy separately. A two-component exponential function fitted the data best at both wavelengths instead of a one-component exponential or a Gaussian profile.

The emission profiles and their errors together with the two-component fits to the profiles are shown in figure 4.11 for the C-band data and in figure 4.12 for the L-band data. In each of the figures 4.11.a, 4.11.b, 4.12.a, and 4.12.b the plot shown on the left panel corresponds to the eastern strip, the center panel to the profile of the central strip, and the right panel to the western strip. The x-axis of the plots give the distance from the major axis, negative numbers refer to the emission below the major axis (south =

S) and positive values to the emission above the major axis (north = N).

In the emission profiles shown in the figures 4.11.a and 4.12.a, we have plotted the values for both the northern and southern halves of the galaxy. However, to determine the scale heights for the northern section of NGC 4631, the points above the disk midplane were given larger weights in order to fit the northern profiles only. This is why the two-component exponential fit is more accurate for the northern profile of the galaxy. The same applies for figures 4.11.b and 4.12.b, but in this case the points below the major axis were given larger weights in order to fit the southern profiles only. The corresponding values for the scale heights for the thin and thick disks are summarized in Table 4.1.

TABLE 4.1— Vertical scale heights of the first (h_{thin}) and second (h_{thick}) components of the exponential fits to the total radio emission profiles. N = north and S = south. The western (W), central (C) and eastern (E) strips have a width of 180″ each.

Strip	**Range [″]**	**C-band**		**L-band**	
		h_{thin} [pc]	h_{thick} [pc]	h_{thin} [pc]	h_{thick} [pc]
NE	-270 to -90	254±34	4044±166	602±31	5113±185
NC	-90 to 90	209±50	2377±123	623±59	3881±336
NW	90 to 270	219±19	3863±148	616±29	4836±279
SE	-270 to -90	1619±112	5073±2533	1731±319	4325±1581
SC	-90 to 90	209±50	2478±228	623±59	3453±461
SW	90 to 270	306±46	2717±208	1023±59	4832±778
Mean		239±32[a]	3425±901	697±130[a]	4407±520

[a] Excluding SE strip, see text for details.

The first component of the exponential fit (third and fifth columns in Table 4.1) has the largest scale height in the SE strip at both wavebands. At C-band (L-band) it is larger by a factor of 5-8 (2-3) than the scale heights of the thin disk in the other parts of the galaxy. This might be related to the disturbance in the eastern side of the disk (refer to Chapter 2) and to the higher star formation activity in this region with respect to the other areas of the galaxy. The distribution of the Hα emission (see fig. 5.1) shows that in the eastern side of the disk there are HII regions below the major axis of the galaxy. This might indicate that the disk in the eastern side of the galaxy is warped and therefore, that we probably cannot detect a thin disk in the southeastern region of NGC 4631. Hence, we have excluded the southeastern strip when estimating the mean values of the thin disk scale height presented in Table 4.1.

The scale heights obtained for the different regions within NGC 4631 deviate from the values published by Mora & Krause (2013) at 4.85 GHz due to the more asymmetric distribution of the emission in their combined map. As has already been mentioned in section 3.4.2, we believe this is because of the algorithm they employed to merge their interferometer and single-dish data, and in addition due to the missing flux in their single-dish map.

For a sample of 3 edge-on galaxies, Dumke & Krause (1998) determined that all three galaxies have similar scale heights for the thin and thick disk independent of star formation activity in the disk and interaction state. Krause (2012) extended the study including 2 more edge-on galaxies (Heesen et al. 2009a; Soida et al. 2011) and concludes that for all five edge-on galaxies the thin disk has a mean value of 300±50 pc and the thick disk a mean value of 1.8 ± 0.2 kpc at λ 6.2 cm. Even though our measurements were not taken at exactly the same frequency all the scale heights of the thin disk observed at C-band, except that of the SE strip, are well in agreement with the mean value found for the other edge-on galaxies. With respect to the scale heights of the thick disk (second component), all scale heights obtained are significantly larger. The emission observed at both wavebands does not display the typical dumbbell structure visible in NGC 253, for example (Heesen et al. 2009a), and in NGC 4565 (Krause 2009). The dumbbell structure with its smaller extent of the emission above and below the central region of the disk and larger z-extents at larger radii seems to reflect dominating synchrotron losses in a magnetic field that is strongest along the central galactic plane of the galaxy (Heesen et al. 2009a). The galaxy NGC 4631 is different in this respect. This will be further discussed in section 4.5.

4.3 Total radio spectral index distribution

The distribution of the total radio spectral indices determined between C-band and L-band data (EVLA + Eff.) are shown in figure 4.6 at an angular resolution of about $34''$. Values were determined only above a 3σ threshold. The error in the spectral index determination was estimated by error propagation assuming that the dominating factor is the standard deviation in the maps (uncertainties due to the flux calibration were excluded). The corresponding error map is presented in figure 4.7, errors in the spectral index distribution increase with decreasing radio intensity. The central region of NGC 4631, together with the radio peak to the eastern side of the disk, have the flattest spectrum within the galaxy with an average value of $\alpha_{\text{tot}} = -0.65 \pm 0.015$. These regions are well known to coincide with HII complexes, as we will demonstrate in Chapter 5. The mean spectral index averaged over the entire disk is $\alpha_{\text{tot}} = -0.76 \pm 0.02$.

The central region has a spur-like extension to the southeast which seems closely connected in position with the HII region CM 67. This extension is also connected to a flat-spectrum area in the disk-halo interface (i.e. $\lesssim 1\overset{\prime}{.}3$ below the plane), where the spectral index ranges between -0.7 and -0.85. On the other hand, the spectral index in other areas of the disk-halo interface is steeper, -0.95 to -1.1. As mentioned in section 4.2, the southeastern region of the disk-halo interface contains HII regions that may account for this flattening of the spectrum. We will further discuss this in section 4.5.

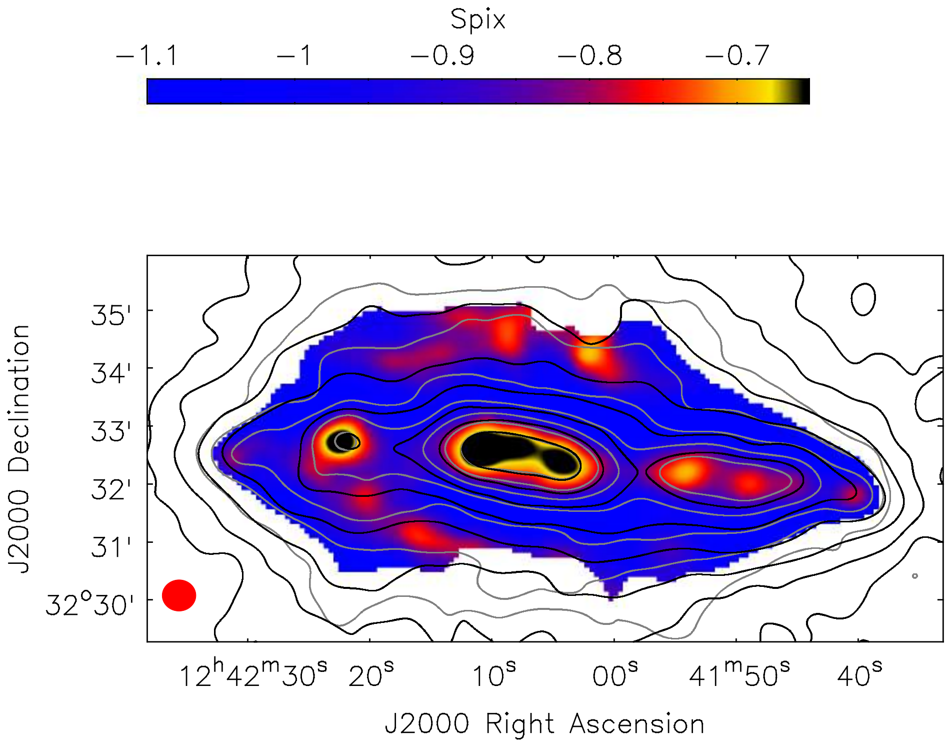

FIGURE 4.6— Total radio spectral indices between C-band and L-band (EVLA + Eff.). Angular resolution is 34.″96 × 32.″32. Grey contours correspond to the C-band emission: 115 μJy/beam $\cdot$ $(3,6,12,24,48,96,192,384)$. Black contours correspond to the L-band emission: 140 μJy/beam $\cdot$ $(3,6,12,24,48,96,192,384)$.

In the halo, the spectrum steepens up to values of -1.25±0.2 towards the outer boundaries. This is expected since the contribution of thermal radiation decreases with increasing distance from the midplane of the galaxy. However, there are several regions in the halo where the spectrum flattens. In the northwestern halo of the galaxy, at the bottom of the depression caused by the NW-radio spur, we have an average spectral index of about -0.69±0.17 which is comparable to that in the disk. Werner (1988) also observed a flattening of the spectrum at this location in the spectral index distribution estimated between his λ 49 and 21 cm data. This is located 23″ to the east of the dwarf elliptical companion NGC 4627, hence, it is difficult to conclude

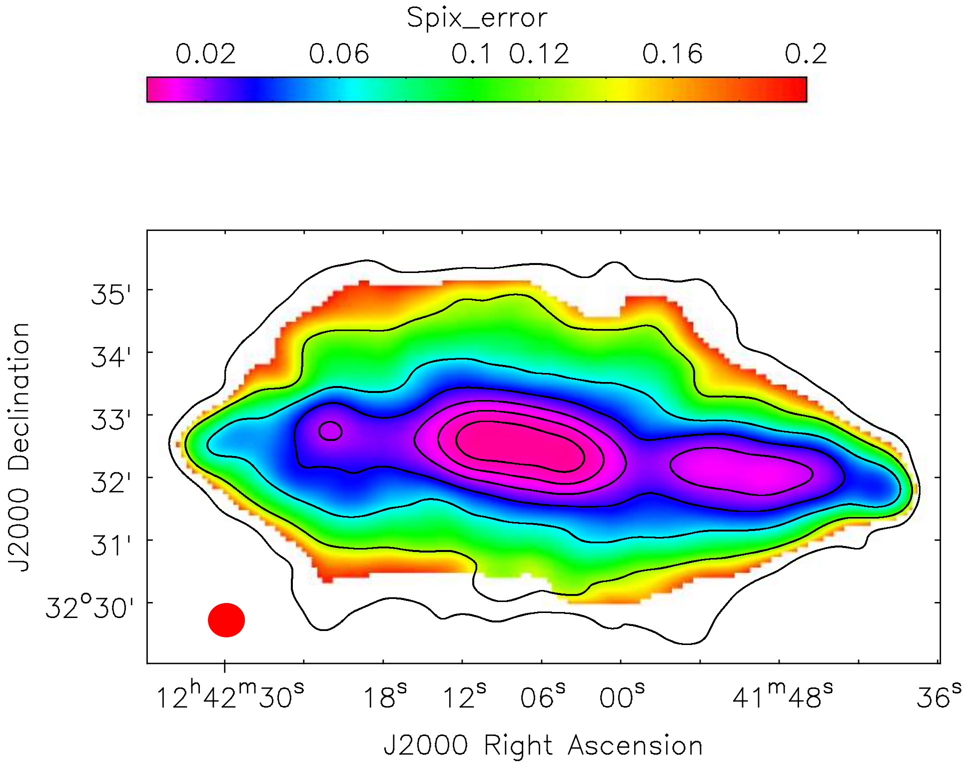

FIGURE 4.7— Error map for the total spectral indices between C-band and L-band (fig. 4.6). Angular resolution is 34.″96 × 32.″32. Contour levels of the C-band emission correspond to 115 μJy/beam $\cdot$ $(3,6,12,24,48,96,192,384)$.

whether they are physically related. According to Rand et al. (1992), there appears to be no detectable Hα emission for the dwarf galaxy, but these authors state that it cannot be completely ruled out since the optical continuum was over subtracted in this area. However, optical observations indicate NGC 4627 has recently formed stars (refer to Chapter 2), therefore, there is a possibility that thermal radiation coming from NGC 4627 might be responsible for the flattening of the spectrum in this region. There is, however, an X-ray source that coincides with the position of the flattening, CXO J124201.29+323417.5 (Liu 2011).

The other region in the halo where the spectrum seems to flatten is directly north of the center at position $\alpha_{2000} = 12^h42^m09^s, \delta_{2000} = 32°34'40''$. The average spectral index is in this area is -0.76±0.11. This feature coincides with what looks like a point source in the infrared. This can be clearly seen in figure 5.10 where we outline the underlying distribution of the 24 μm emission with respect to the radio emission. This feature actually forms part of a compact group of 4 galaxies known as SDSSCGB 45319 (McConnachie et al. 2009).

4.4 Background radio galaxies

In our data we have identified two radio galaxies in the vicinity of NGC 4631. One of them is located at the center of NGC 4631, in figure 4.8 we identify the location of the source and present its spectral index distribution. Unfortunately, we do not have sufficient angular resolution to resolve its inner components. We estimate the spectral index of the eastern lobe to be -0.67 ± 0.01 and the western lobe has a slightly flatter spectral index of -0.65 ± 0.01. Golla (1999) observed the central region of NGC 4631 with the VLA in the A&B configuration achieving a resolution of $0.35''$. At this resolution the object is resolved into at least 3 components that are well aligned.

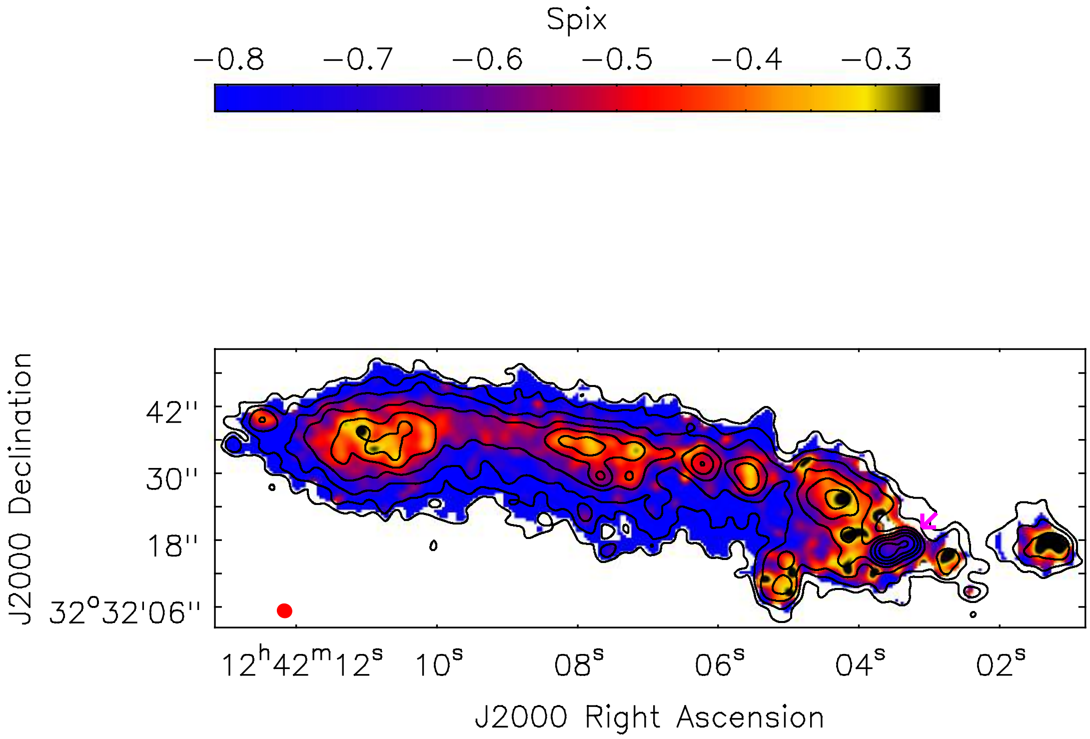

FIGURE 4.8— The background radio galaxy in the central region of NGC 4631 is indicated with a magenta arrow. The colorscale represents the spectral index distribution between C-band and L-band data. Angular resolution is $2.''7 \times 2.''5$. Contour levels of the total C-band emission correspond to $8.5\ \mu\mathrm{Jy/beam} \cdot (3, 6, 12, 24, 48, 96, 192, 384)$.

The other background radio galaxy is the bright source to the southwest of

NGC 4631 at $\alpha_{2000} = 12^h41^m52.3^s, \delta_{2000} = 32°27'14''$. In order to fully observe the galaxy within the C-band primary beam we imaged half of the bandwidth (4.979-5.99 GHz). We present the first high-resolution analysis of this source. Its spectral index distribution determined above 5σ threshold is shown in figure 4.9 and its corresponding error map in figure 4.10.

The two radio lobes can be clearly seen in figure 4.9. We could not, however, identify the compact core in our radio data. The spectrum in the northern lobe steepens from -0.71±0.01 in the outer parts, to -1.35±0.18 towards the nucleus of the galaxy. The southern lobe also steepens towards the core from about -0.78±0.04 in the extremities to -1.45±0.15 closer to the center. This spectral index distribution is typical of FR II radio galaxies (Fanaroff & Riley 1974) and is consistent with the backflow model (Leahy & Williams 1984; Leahy et al. 1989). According to this model, electrons are reaccelerated in the hotspots that give rise to a flat spectral index. These electrons then flow back towards the nucleus due to the pressure gradient created by the AGN jet, and therefore, the emission closer to the core is composed of an older population of CREs which make the radio spectrum steeper. This process has also been observed in other radio galaxies (Lara et al. 2000; Tamhane et al. 2015). The flattest feature in the spectral index distribution of the northern lobe suggests the existence of a faint hotspot at the end of the lobe, while a similar feature is not visible in the southern lobe perhaps due to a relativistic beaming effect.

This radio galaxy is also linearly polarized ($\sim 6\%$ at L-band), in Chapter 6 we present its rotation measures and magnetic field properties. No X-ray data is available in the literature for this galaxy except what may be a plausible candidate for its core, CXO J124152.3+322714, an X-ray source at position $\alpha_{2000} = 12^h41^m52.346^s, \delta_{2000} = 32°27'14.33''$. X-ray observations would provide valuable information on the physical properties of the environment surrounding the radio lobes, for example, the pressure of the intergalactic medium that the lobes are expanding into, estimates of the expansion timescale, the possible AGN power output, and the dominant energy loss mechanism of the lobes (i.e. synchrotron or IC).

4.5 Discussion

In section 4.1 we demonstrated there is some correlation between the Hα filaments and the radio continuum emission. Similar outflows have also been detected in the soft X-ray emission (Wang et al. 2001), the HI disk (Rand & van der Hulst 1993), dust (Alton et al. 1999) and CO emission (Rand 2000). This supports the idea that gas is being raised out of the plane by star formation and that there is a disk-halo interface which is strongly regulated by star formation.

With EVLA test observations at L-band (C array) Irwin et al. (2012a) claim that the NW-radio spur forms part of a loop that is related to a loop of X-ray hot gas in the northwestern halo (see fig. 7 of their paper). Inspecting our data carefully, we find unlikely that this spur is part of a loop. At C-band the NW-radio spur does not show any type of bending towards the northeast as it does at L-band (see fig. 4.2). On the other hand, figure 4.5 demonstrates the tight correlation between the uppermost emission of the NW-radio spur and the HI spur 4. According to Rand (1994), the HI spur 4 joins the disk at the western end and extends towards the northeast. This leads us to believe the NW-radio spur might be composed of two features along the LOS that look like one curved extension when projected onto the plane of the sky. One of the extensions may be oriented north-south having a counterpart at C-band. The other extension oriented towards the northeast could be located in the outskirts of the halo closely connected to the HI spur 4

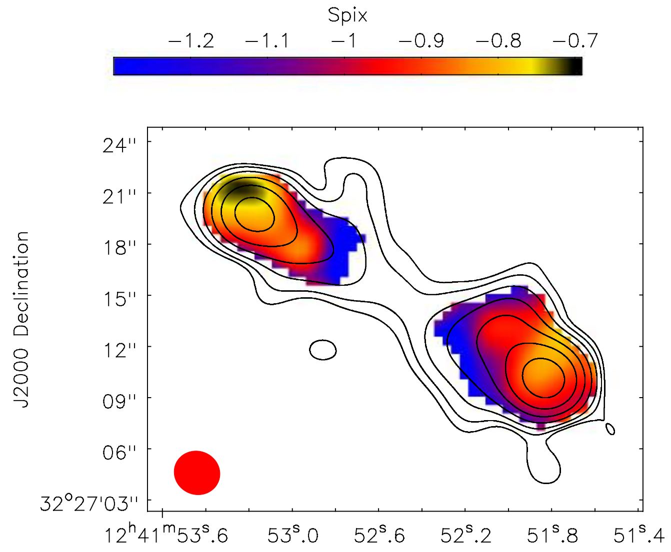

FIGURE 4.9— Background radio galaxy in the southwest of NGC 4631. The colorscale represents the spectral index distribution between C-band (5-6 GHz) and L-band data. Angular resolution is $2''.7 \times 2''.5$. Contour levels of the total L-band emission correspond to 34 μJy/beam $\cdot\,(3,6,12,24,48,96,192,384)$.

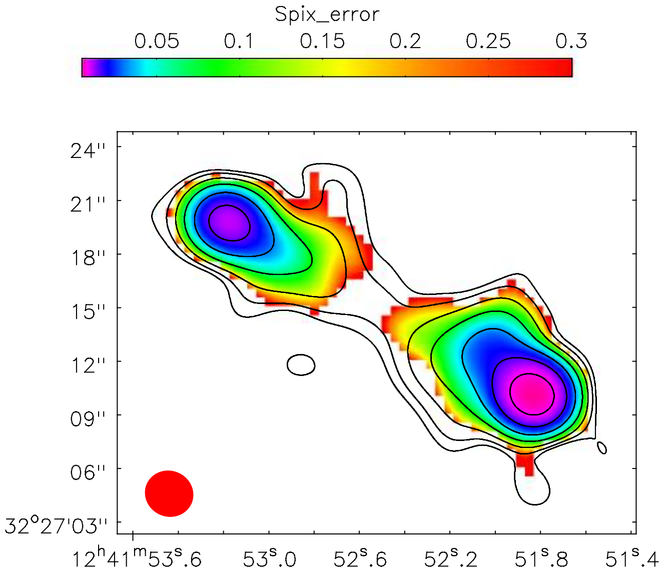

FIGURE 4.10— Error map for the total spectral indices shown in fig. 4.9. Angular resolution is $2''.7 \times 2''.5$. Contour levels of the total L-band emission correspond to 34 μJy/beam $\cdot\,(3,6,12,24,48,96,192,384)$.

An interesting question we would like to address: Why do the thick disk scale heights measured at C-band strongly deviate from the average value observed in other edge-on galaxies? Strong star formation in the disk cannot be entirely responsible for this deviation, as other galaxies with even higher SFR, like NGC 253, show the usual values published by Krause (2012). In addition, if star formation were solely accountable for this deviation we would observe a similar trend for the scale heights of the thin disk. However, the only scale height which is larger is that found in the southeastern part of NGC 4631, all the other thin disk scale heights observed at C-band agree with the mean value determined for the other edge-on galaxies.

Simulations of the interaction between NGC 4631 and its two companions (NGC 4656 and NGC 4627) by Combes (1978) indicate the material in the HI spur 1 and spur 4 comes from NGC 4631 (see fig. 4.5). Whereas that of the HI spur 2 and spur 3 originate from the now dwarf elliptical galaxy NGC 4627, which may have been a gas-rich galaxy before the encounter with NGC 4631. If so, material may also stream onto NGC 4631. An optical study of the vertical structure in NGC 4631 (Ann et al. 2011) detected the northwestern halo of the galaxy has the largest scale height of more than 2 kpc. These authors interpret this as diffuse stellar emission and speculate that tidal debris of the satellite galaxies that accreted to NGC 4631 may contribute to this diffuse stellar emission. Even extraplanar cold dust has been found up to about 10 kpc above the disk midplane in NGC 4631 (Neininger & Dumke 1999). Therefore, tidal interaction may help explain why the halo scale heights are much larger than those found in other galaxies.

Another galaxy with strong tidal interaction is the starburst galaxy M 82. Adebahr et al. (2013) determined scale heights at four different wavelengths for this galaxy and found the scale heights were smaller than the usual values and that they differed systematically between the northern and southern halves of M 82. Due to the gravitational interaction caused by the M81/M82-group core, the IGM is expected to be denser towards the south of M 82 and this may lead to higher cosmic ray losses and hence, to smaller scale heights in this region of the galaxy. According to Arshakian et al. (2009), tidal interaction or minor mergers may also induce star formation in the disk. Therefore, tidal interaction may influence the vertical scale heights either directly by dragging out material and magnetic field from the disk into the halo, or indirectly by inducing higher star formation in the disk and/or by modifying the loss processes of the cosmic rays in the halo as a result of the intergalactic material produced by the tidal interaction.

As mentioned in section 4.2, the radio halo in NGC 4631 does not show the characteristic dumbbell structure visible in other edge-on galaxies. These facts and the fact that the thick disk scale heights are significantly larger than usual, supports the view that convection may be strong in NGC 4631. Rand et al. (1992) draw the same conclusion from their Hα observations. The Hα emission is very irregular and disturbed with a patchy high-z structure. They could not detect a smooth, extended, diffuse Hα halo and suspected convection is strong and that matter is transported to large distances in the halo which is then responsible for the X-ray emission.

At both wavebands, we observed that the scale height of the first component to the exponential fit is considerably larger in the southeastern part of the galaxy than in the other areas of NGC 4631. In addition, the southeastern region of the disk-halo interface is found to be much flatter than in other regions of the galaxy. As mentioned in Chapter

2, the HI shell in the southeastern side of the plane corresponds to a disturbance in the disk which is not only seen in the Hα emission but also in the optical and UV. This disturbance of the disk emission is reflected both in the scale heights and in the flattening of the spectral index. This might also be an indication that the disk in the eastern side of the galaxy is warped and therefore, that we probably cannot detect a thin disk in this region within NGC 4631. An intriguing scenario to explain this disturbance was suggested by Rand & van der Hulst (1993), wherein NGC 4627 hit the disk of NGC 4631 creating this HI shell and forming the HI spur 2 as gas was stripped from the companion galaxy. NGC 5775 is another galaxy with strong tidal interactions which also presents several HI supershells. Lee et al. (2001) demonstrate the radio continuum spectral index is flatter around one of the shell rims in NGC 5775 and conclude that this cannot be caused by thermal gas but rather that it might be a product of shocks in these regions.

4.6 Conclusions

We combined new radio data of the edge-on spiral galaxy NGC 4631 taken with the EVLA and the Effelsberg telescopes at two different wavebands, C-band and L-band. The merging was done in the image domain to recover the missing spacings caused by the sampling of the EVLA antennae. At C-band we recovered ~27% of the total flux-density of the galaxy attributed to the large-scale structures. In addition, by combining single-dish and interferometer data we recovered missing flux even in the L-band diffuse emission which amounted to ~11% of the total flux-density of NGC 4631. In the previous chapter we derived the total integrated spectral index of the galaxy. In this chapter we compared the radio continuum emission of NGC 4631 with the radiation observed at other frequencies, estimated the radio vertical scale heights and derived the spectral index distribution of the galaxy. We also presented two background radio galaxies in the vicinity of NGC 4631 and analyzed their spectral index distribution. Our main conclusions are the following:

1. We fit a single power law with the total flux-densities of NGC 4631 measured with single-dish data at six different frequencies, obtaining a total integrated spectral index of $\alpha_{tot} = -0.81 \pm 0.03$. Within the errors the integrated spectral index agrees with that published by Hummel & Dettmar (1990) and Mora & Krause (2013).

2. The spectral index distribution of the background radio galaxy to the southwest of NGC 4631 is flat in the outskirts of the lobes and steepens towards the core. This spectral index distribution is typical of FR II radio galaxies and is consistent with the backflow model. According to this model, the electrons reaccelerated in the hotspots flow back to the nucleus due to the pressure gradient created by

the AGN jet, and therefore, the emission closer to the core is composed of an older population of CREs which make the radio spectrum steeper.

3. The mean vertical scale height in NGC 4631 observed at C-band for the thick disk (3.4 ± 0.9 kpc) is larger with respect to the mean thick disk found in five other edge-on spiral galaxies (Krause 2012). The scale heights of the C-band thick disk are on average larger by a factor of 1.9. There are several indications that convection may be strong in NGC 4631, which may originally be related to its tidal interaction with its neighbouring galaxies. Because of the tidal interaction, material may be dragged out or even stream onto NGC 4631. Hence, this interaction may explain why the halo scale heights deviate from those of the other galaxies without strong tidal interaction.

4. The disturbance in the eastern side of the disk of NGC 4631 has been strongly indicated to be caused by tidal encounters. This disturbance is reflected in the radio continuum emission in two ways that we have accounted for. Firstly, the scale heights of the first component to the exponential fits at both wavebands are larger in the southeastern region with respect to the other areas of NGC 4631. Secondly, the disk-halo interface in the southeastern side presents flatter spectral indices than in the other regions of the galaxy.

Fit to the emission in the **north**

(a)

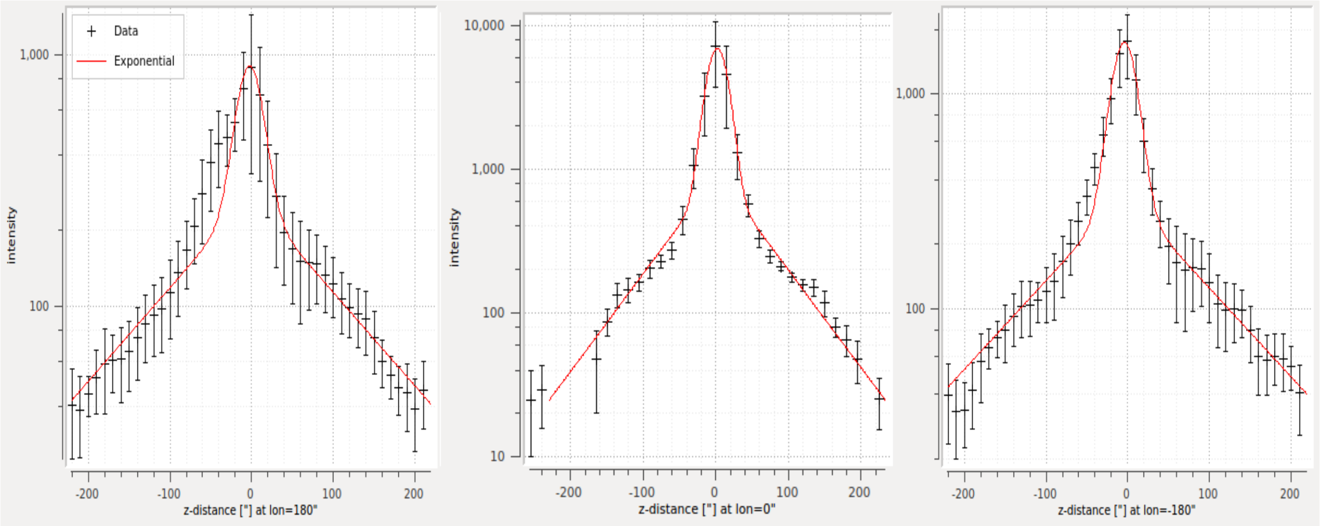

Fit to the emission in the **south**

(b)

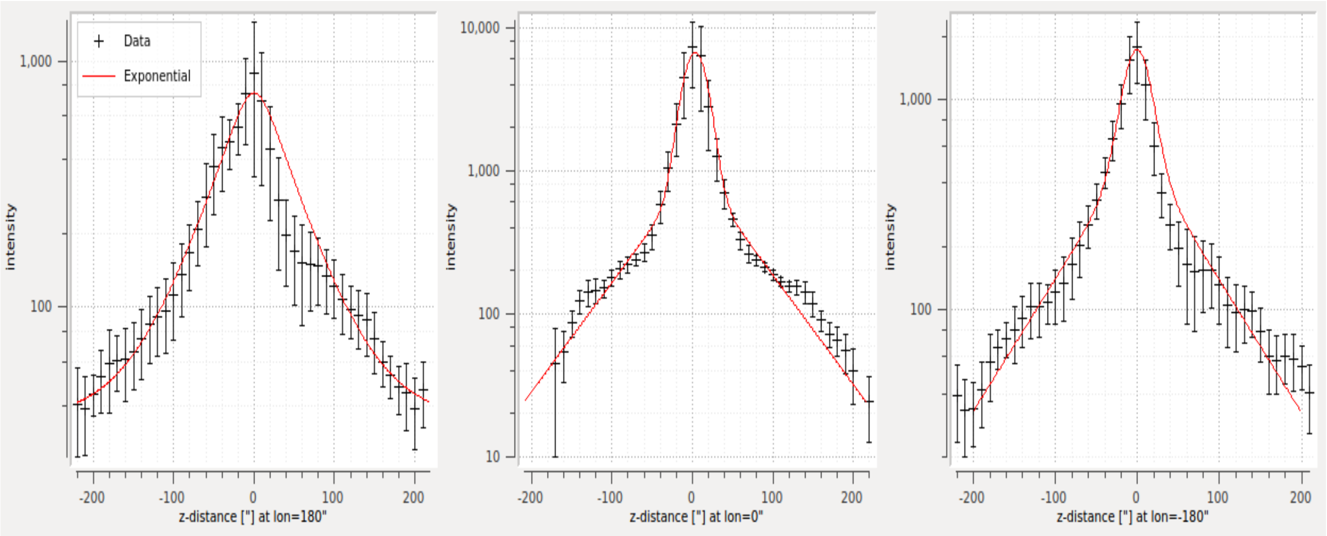

FIGURE 4.11— Total radio intensity profiles of the C-band emission (EVLA + Eff.) in μJy/beam. The measured points are averaged in 3 strips parallel to the minor axis of 180$''$width each, the left panel corresponds to the eastern strip (-270$''$ to -90$''$), the center panel to the central strip and the right panel to the western strip (90$''$ to 270$''$). The x-axis of the plots gives the distance from the major axis in [$''$], negative numbers refer to the emission below the major axis (south) and positive values to the emission above the major axis (north). The thick red lines represent the two-component exponential fits to the C-band data. In figure 4.11.a (4.11.b) the points above (below) the major axis were given larger weights in order to fit the northern (southern) scale heights.

Fit to the emission in the **north**

(a)

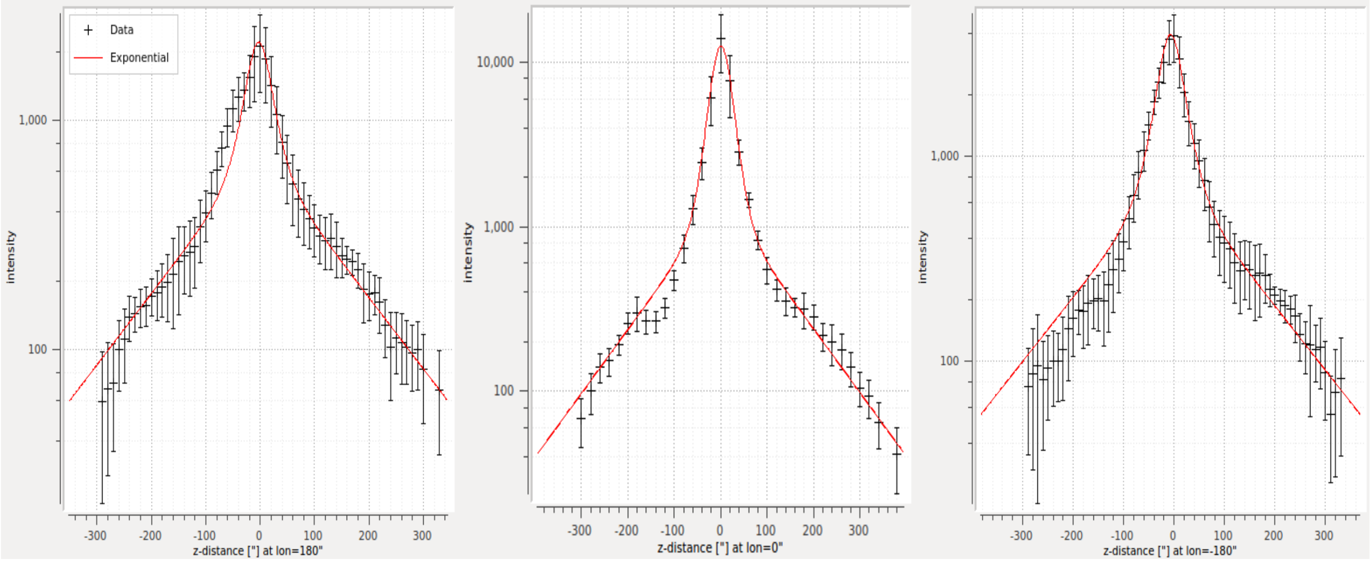

Fit to the emission in the **south**

(b)

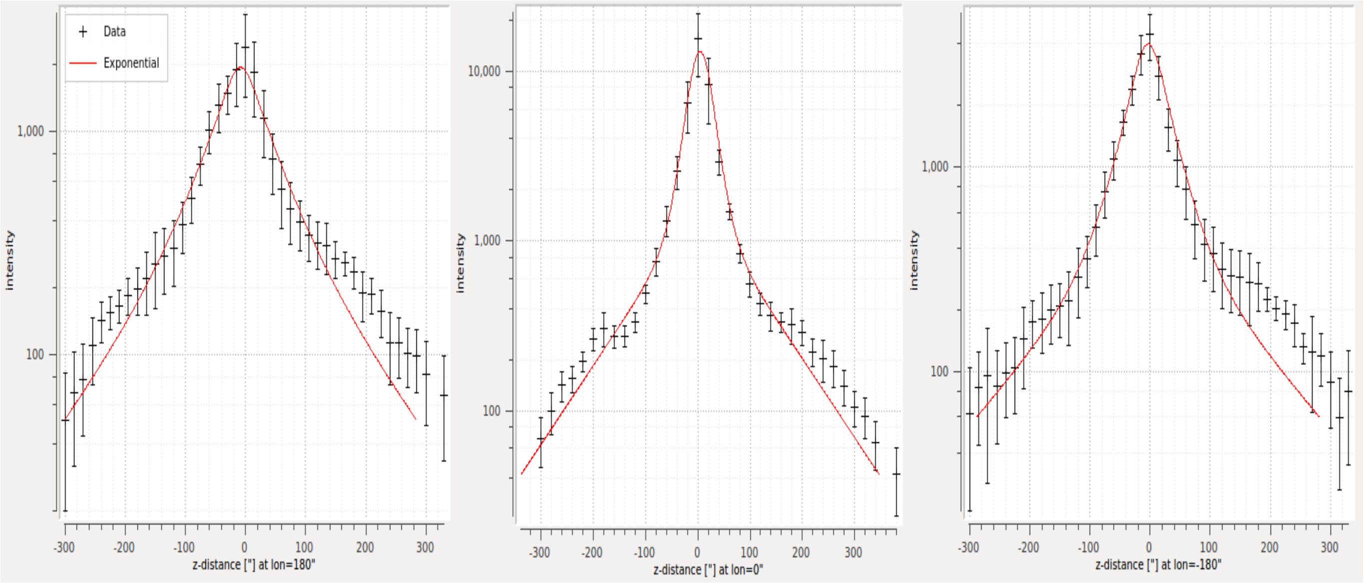

FIGURE 4.12— Total radio intensity profiles of the L-band emission (EVLA + Eff.) in μJy/beam. The measured points are averaged in 3 strips parallel to the minor axis of 180″width each, the left panel corresponds to the eastern strip (-270″ to -90″), the center panel to the central strip and the right panel to the western strip (90″ to 270″). The x-axis of the plots gives the distance from the major axis in [″], negative numbers refer to the emission below the major axis (south) and positive values to the emission above the major axis (north). The thick red lines represent the two-component exponential fits to the L-band data. In figure 4.12.a (4.12.b) the points above (below) the major axis were given larger weights in order to fit the northern (southern) scale heights.

5

Thermal Radio Emission

"If I had to choose a superhero to be,
I would pick Superman.
He's everything that I'm not!"
Stephen Hawking

The radio continuum emission in spiral galaxies emerges from two emission mechanisms, thermal free-free and nonthermal synchrotron emission. As mentioned in section 1.1.2, synchrotron emission can be used to infer properties of the magnetic field and study the propagation of cosmic rays in galaxies. However, to do this one must first estimate the thermal component and separate it from the total radio emission. For a sample of 74 galaxies, Niklas et al. (1996) have shown that $7 \pm 1\%$ of the integrated radio emission at 1 GHz is thermal in origin. Due to the power law behaviour of the synchrotron spectrum, it is expected that the thermal emission dominates with increasing frequency. Therefore, we emphasize the importance of this separation and its underlying implications.

Young massive stars emit the bulk of their energy at UV wavelengths. These UV photons ionize the interstellar gas creating what are known as HII regions, and these dense regions then re-emit their energy as emission lines. In addition, UV photons also interact with dust particles present in the interstellar medium and this interaction is responsible for dust emission at IR wavelengths.

Thermal free-free emission emerges in a photo-ionized medium, like HII regions or the diffuse ionized gas. Hydrogen recombination lines can be used to trace free-free emission as long as there is balance between the heating (ionization) and cooling (recombination) mechanisms in these ionized regions. Hydrogen lines can be observed over a wide spectrum from optical frequencies, as the Balmer series, to radio frequencies, as Radio Recombination Lines. However, the weak intensities of the Radio Recombination Lines makes it very difficult to detect them, specially from diffuse ionized gas. Among the optical recombination lines, the Hα emission line is the most commonly used because it is bright and easily detectable.

The most direct way to trace the thermal free-free emission in external galaxies would be through their Hα emission. However, this tracer suffers from severe attenuation due to dust grains present in the interstellar medium (see section 1.3). The Hα emission can be corrected for extinction with diagnostics like the Balmer decrement or the Paα/Hα ratio (Moustakas et al. 2006). Such high resolution spectrophotometry, however, is not easy to obtain. There are also calibrations that can be applied to correct for dust extinction, but all have a certain degree of uncertainty. In fact, the correction for dust extinction is the main contributor of systematic errors into measurements of global galaxy properties such as the star formation rate (SFR), metallicity, or age (Kennicutt 1998; Calzetti 2001; Bell 2002). For galaxies ongoing star formation this problem has an even greater impact since this process occurs in very dense areas (both of gas and dust) where stars are born. Hence, this produces high attenuation with large spatial variations in star forming galaxies.

An alternative approach to estimate the Hα correction for extinction in very dusty galaxies is through their infrared emission. The 24 μm IR emission is known to be dominated by radiation from warm dust, which are mostly heated by young massive stars located in HII regions. There are several studies that suggest that the 24 μm emission can be a useful indicator of ionized gas. For instance, inspection of data of nearby galaxies, M 51 (Calzetti et al. 2005) and M 81 (Pérez-González et al. 2006), revealed that the 24 μm emission of HII knots is tightly correlated with the extinction-corrected Paα. There is also the work of Dale et al. (2005) for 170 regions within 3 Spitzer Infrared Nearby Galaxies Survey (SINGS) galaxies (Kennicutt et al. 2003).

There are diverse calibrations in the literature that are based on linear or nonlinear relations between the 24 μm luminosity and the extinction-corrected Hα emission. These use a variety of samples composed of either galaxies or HII regions. However, this tracer too suffers from its own underlying uncertainties. One of the systematic errors arises due to the contribution of dust heating by the older stellar populations, referred to as the *IR cirrus problem* (Walterbos & Greenawalt 1996; Kennicutt 1998). The IR cirrus component introduces diffuse emission into 24 μm measurements. According to Dale et al. (2007), this diffuse component contributes with up to half of the total 24 μm emission in M 81. Moreover, in dust-poor environments, such as dwarf galaxies, the infrared radiation may be so low that it may lead to underestimating the thermal emission (see for example Wang & Heckman 1996). The same thing may be said for the outer disks and halos of galaxies.

For this reason, tracers combining both optical and IR observations have been proposed. As suggested by Kennicutt et al. (2007), the combination of Hα and 24 μm measurements can provide information on both the unobscured and obscured regions within galaxies. The basic idea is the amount of Hα radiation attenuated should scale with the luminosity reradiated in the IR. Hence, the observed Hα and 24 μm emission can be used to correct the Hα for extinction. Calzetti et al. (2007) demonstrated that combining the 24 μm emission with the uncorrected Hα emission for 33 SINGS galaxies may be one of the best tracers of the corrected Paα emission in HII regions. In addition, Kennicutt et al. (2009) apply the same methodology to their sample of integrated measurements of 205 galaxies and find that the extinction-corrected Hα derived from a combination of the observed Hα and 24 μm luminosities are in good agreement with the Hα emission corrected for extinction using the absorption-corrected Hα/Hβ ratios in the optical spectra.

There have been several spatially resolved studies that have estimated the thermal emission in spiral galaxies, for example refer to those of Tabatabaei et al. (2007); Basu et al. (2012); Leroy et al. (2012). However, there is an additional complication which originates from the fact that one is viewing NGC 4631 from an edge-on perspective. As a consequence, the galaxy might not be transparent in Hα emission, i.e. one might only be detecting line-emission from the near side of NGC 4631. Smith et al. (2001) conclude from HI and HII position-velocity curves, and from their extinction considerations, that the detected FUV emission of NGC 4631 originates from the outer edges of the galaxy. The farther photons have to travel through the galaxy the more dust particles they might encounter in their trajectory that can cause absorption. Hence, there may be significant missing Hα flux, specially in the disk where the LOS through the galaxy is the largest. This effect decreases with increasing wavelength, hence, the IR emission should not be severely affected.

Due to the complexity of the situation there is no definitive way to estimate the thermal emission in edge-on galaxies, specially at small spatial scales. To derive thermal estimates at high spatial resolutions one has to take into account the properties of the medium along the LOS. This is why this chapter focuses on comparing three different methods to derive the thermal emission of NGC 4631. The first method was developed by Tabatabaei et al. (2007) (hereafter denoted as T2007). These authors correct the Hα emission in M 33 for extinction by estimating the effective optical depth using the 70 and 160 μm color. The second method is based on the classical approach of correcting for extinction by combining Hα and IR measurements. The third method assumes that scaling the 24 μm emission by a certain value is sufficient to correct the Hα emission for extinction. This is the first time these three methods have been used to derive the thermal emission for an edge-on galaxy on a pixel-by-pixel basis.

5.1 Preparing the data

Since the data used for this study was observed with different telescopes and was processed with different reduction packages, it is necessary to convert maps to a common unit system. The following definitions are essential to achieve this:

- Gaussian beam area: if one assumes the primary beam pattern to be Gaussian, its beam area (solid angle) is then given by[1]

  $$\Omega\,[\mathrm{arcsec}^2 \cdot \mathrm{beam}^{-1}] = \frac{\pi}{4\ln(2)} \cdot \mathrm{FWHM} = 1.1331 \cdot \mathrm{FWHM}^2 \tag{5.1}$$

  The full width at half maximum (*FWHM*) is given in arcsec. The beam area can be easily converted to steradians per beam.

- Number of pixels per beam: the number of pixels in a given beam area can be defined as

  $$\mathrm{Number}_{\mathrm{pixels}}\,[\mathrm{pixel} \cdot \mathrm{beam}^{-1}] = \frac{\pi}{4\ln(2)} \cdot \frac{\mathrm{FWHM}^2}{\mathrm{Area}_{\mathrm{pixel}}} = 1.1331 \cdot \frac{\mathrm{FWHM}^2}{\mathrm{Area}_{\mathrm{pixel}}}, \tag{5.2}$$

  where $Area_{pixel}$ is the corresponding pixel area in arcsec^2.

5.1.1 Hα data

Ancillary Hα data for NGC 4631 was obtained from the SINGS survey (Kennicutt et al. 2003). Observations were performed with the Kitt Peak National Observatory 2.1-m telescope (filter: KP1563) in 2002. The data also contains [NII] (λ 6548, 6584 μm) line emission. The map was in units of counts-per-seconds ($DN \cdot pixel^{-1} \cdot sec^{-1}$), psf $1\overset{''}{.}2$ with a pixel size of $0\overset{''}{.}3$.

The subtraction of the foreground stellar continuum left some artifacts which affected the flux in the northern halo of the galaxy. These artifacts were removed with the help of a Gaussian fitting procedure in the data reduction system NOD3. The map was then convolved and regridded in AIPS to a beam size of $18''$ ($4\overset{''}{.}5$ pixel size). In addition, the map was renormalized to conserve the integrated number of counts-per-seconds of the initial map.

According to the SINGS *Fifth Data Delivery Guide* (FDDG)[2], one can convert to flux with the following expression:

---

[1] For more details refer to the book *Tools of Radio Astronomy* by Wilson et al. (2009).

[2] Available at `https://irsa.ipac.caltech.edu/data/SPITZER/SINGS/doc/sings_fifth_delivery_v2.pdf`

$$F\,[\mathrm{erg}\cdot\mathrm{sec}^{-1}\cdot\mathrm{cm}^{-2}] = \frac{3\cdot 10^{-5}\cdot\mathrm{CPS}\cdot\mathrm{PHOTOFLAM}\cdot d\lambda}{\lambda^2}, \tag{5.3}$$

where *PHOTOFLAM* is the flux conversion factor given in the header of the map and *CPS* is the counts-per-seconds value. The parameter $d\lambda$ is the full width at half maximum of the narrow-band filter and λ is the central wavelength, both values for each corresponding filter can be found in the FDDG and should both be given in Angstrom. Hα luminosities range between $3.5\cdot10^{37}$ and $4\cdot10^{38}$ erg/sec. The integrated Hα luminosity for NGC 4631 is of $2\cdot10^{41}$ erg/sec.

The map was converted to units of Jy/beam by using $F = F_\nu d_\nu = F_\nu\cdot c\cdot\left(\frac{d\lambda}{\lambda^2}\right)$ and by multiplying by the number of pixels within a beam (Eq. 5.2). The Hα distribution with a resolution of 18″ FWHM is plotted in figure 5.1.

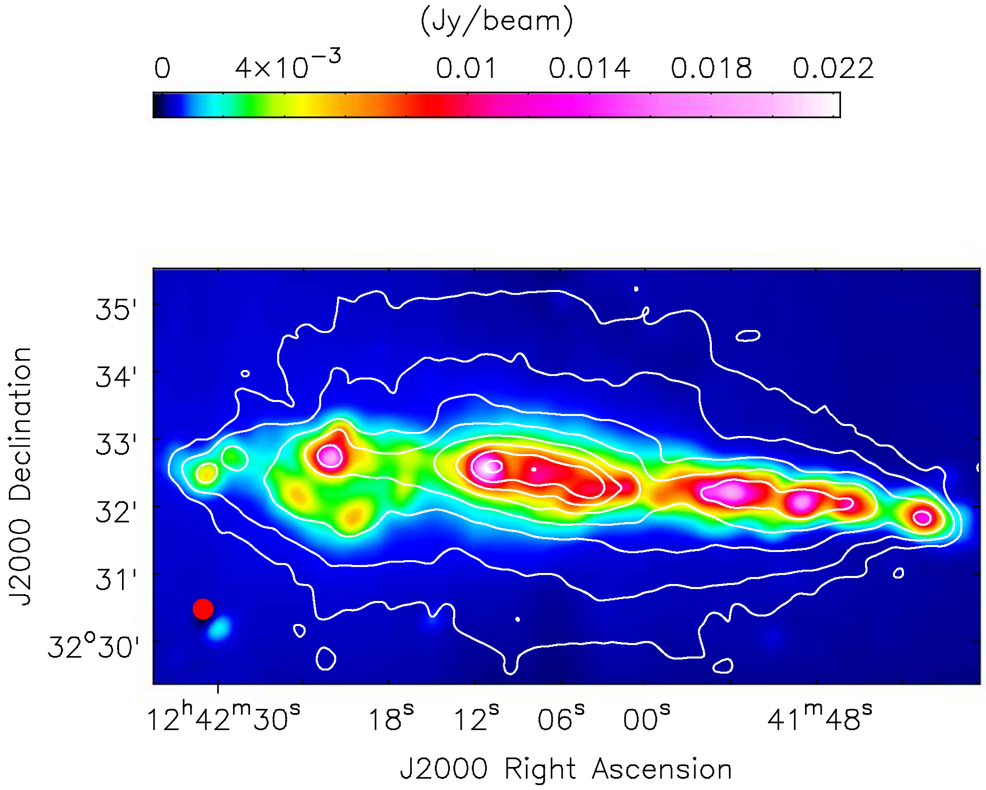

FIGURE 5.1— Hα emission of NGC 4631 at a resolution of 18″ FWHM. Contour levels of the total C-band emission (EVLA + Eff.) correspond to 45 μJy/beam $\cdot$ (3, 6, 12, 24, 48, 96, 192, 384). Hα data from Kennicutt et al. (2003)

5.1.2 PACS 70 and 160 μm data

Infrared data of NGC 4631 at 70 and 160 μm was available thanks to the project "Key Insights on Nearby Galaxies: a Far-Infrared Survey with the Herschel" (KINGFISH; Kennicutt et al. 2011). The source was observed with the *Photodetector Array Camera and Spectrometer (PACS; Poglitsch et al. 2010)* on board Herschel. Meléndez et al. (2015) present a detailed analysis of these observations together with data at other IR wavelengths. The 70 μm map had a resolution of 5.″76 x 5.″46 and a pixel size of 1.″4. Furthermore, the 160 μm map had a resolution of 12.″13 x 10.″65 and a pixel size of 2.″85. Both maps were in surface brightness units of Jy/pixel.

The maps were convolved to a Gaussian beam with a FWHM of 17″ using the kernels provided by Aniano et al. (2011). These images were then converted to units of Jy/beam with use of equation 5.2, and subsequently, they were smoothed and regridded in CASA to a resolution of 18″ (4.″5 pixel size).

5.1.3 MIPS 24 μm data

SINGS archival 24 μm data, observed in 2005 with the *Multiband Imaging Photometer for Spitzer (MIPS; Rieke et al. 2004)*, was available for NGC 4631. Bendo et al. (2006) explain the calibration procedure implemented, present a thorough analysis of the data and correlate with other Spitzer wavelengths. The data had a resolution of 6″, a pixel size of 1.″5 and was calibrated in units of MJy/sr.

The map was convolved to a Gaussian beam with a FWHM of 17″ using the kernels provided by Aniano et al. (2011). The map was converted to units of Jy/beam with equation 5.1, then it was smoothed and regridded in CASA to a beam size of 18″ (4.″5 pixel size). The 24 μm luminosities range between $5{\cdot}10^{36}$ and $7 \cdot 10^{39}$ erg/sec. The integrated 24 μm luminosity of NGC 4631 is of $1.4{\cdot}10^{42}$ erg/sec (Dale et al. 2007).

5.2 Method one: thermal estimate with $\mathbf{I}_{70\mu\mathrm{m}}/\mathbf{I}_{160\mu\mathrm{m}}$ dust ratio

5.2.1 Dust color temperature

The color temperature distribution of the dust in NGC 4631 was derived according to equation 1 in T2007. At high frequencies, Wien's approximation can be applied. Hence, the color temperature in Kelvin can be easily estimated with the following equation:

$$T[K] = \left(\frac{h}{k}\right) \cdot \frac{\nu_2 - \nu_1}{ln\left[\frac{F_1}{F_2} \cdot \left(\frac{\nu_2}{\nu_1}\right)^5\right]} \tag{5.4}$$

where F_1 and F_2 are the measured fluxes at 70 and 160 μm, respectively, and ν_1/ν_2 their corresponding frequencies. The parameters h and k are the Planck and the

Boltzmann constants. Only pixels above a threshold of 3σ were taken into account. The resulting dust color temperature distribution is plotted in figure 5.2. Temperatures range between 19 K and 28 K. The highest temperatures are found in the central area of the galaxy, where the star formation is expected to be strongest.

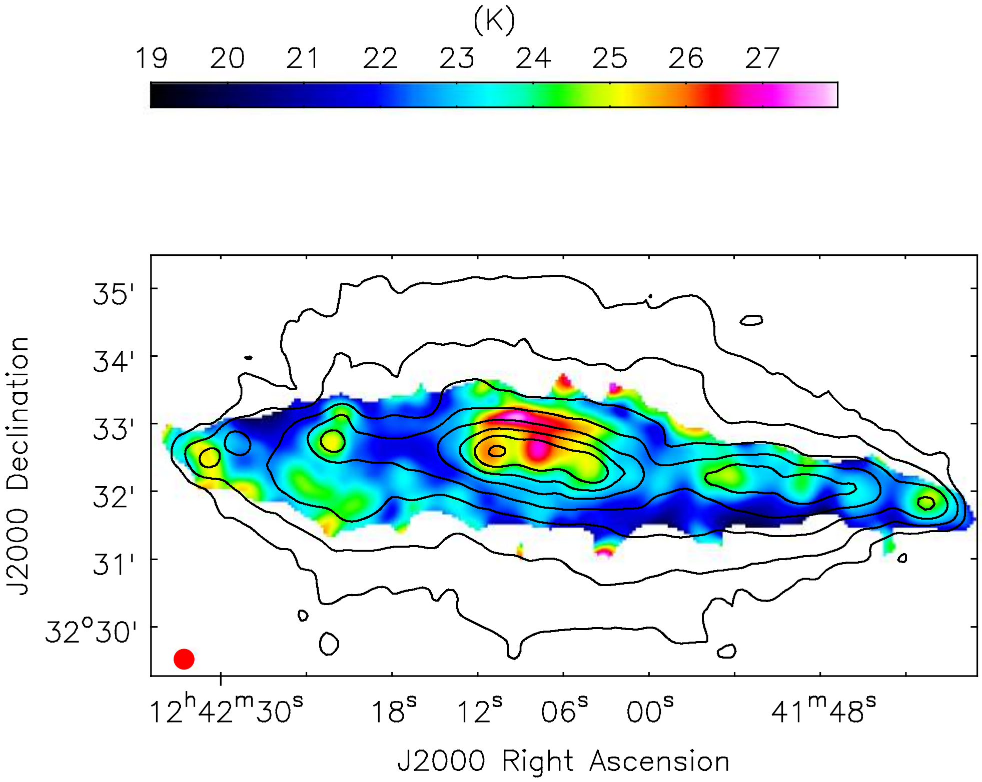

FIGURE 5.2— Dust temperature distribution of NGC 4631 at a resolution of 18″ FWHM. Color scale given in Kelvin. Contour levels of the total C-band emission (EVLA + Eff.) correspond to 45 μJy/beam $\cdot$ $(3,6,12,24,48,96,192,384)$.

Meléndez et al. (2015) also derived a dust temperature map of NGC 4631 at a spatial resolution of 36″ FWHM (18″ pixel size) by fitting the spectral energy distribution (SED) between 70-500 μm and by assuming a floating spectral index. Their values also range between ~18.8-27.5 K and the temperature distribution is very similar. Above the central region they detected a bubble-like feature of warm dust they call the *superbubble region* which extends up to 6.2 kpc (considering the adopted distance throughout this work) above the major axis. This supperbubble is appropriately centered at $\alpha_{2000} = 12^h42^m08^s, \delta_{2000} = 32°33'30''$ According to these authors the supperbubble contains about 4% of the total dust mass of the galaxy, it is characterized by a steeper spectral index and higher temperature than the dust in the disk. Traces of this bubble-like structure above the central region are visible in figure 5.2.

5.2.2 Optical depth at 160 μm and Hα wavelengths

The optical depth at 160 μm ($\tau_{160\mu\mathrm{m}}$) can now be derived with the dust temperature as described in section 4 of T2007. The distribution of optical depth is shown in figure 5.3.

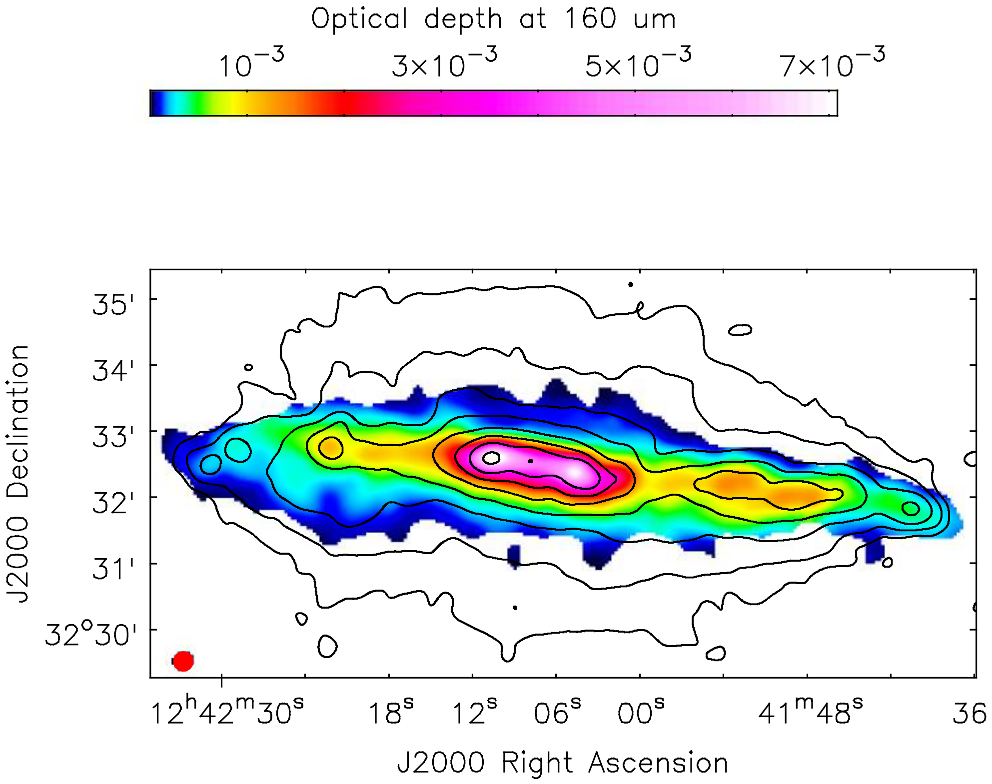

FIGURE 5.3— Dust optical depth at a wavelength of 160 μm ($\tau_{160\mu\mathrm{m}}$). Angular resolution is 18″ FWHM. Contour levels of the total C-band emission (EVLA + Eff.) correspond to 45 μJy/beam $\cdot$ $(3, 6, 12, 24, 48, 96, 192, 384)$.

To obtain the optical depth at the Hα wavelength (λ 0.656 μm), one has to take into account the ratio between the dust extinction coefficients per unit mass at 0.656 μm and 160 μm. These values were derived with the extinction curve for the dust model of the diffuse medium from Kruegel (2003). This model is relatively simple but it reproduces a sufficiently good interstellar extinction curve for our wavelength range of interest. We obtained a ratio of 2200 which was multiplied with the $\tau_{160\mu m}$-map to obtain the plot shown in figure 5.4, the optical depth at the Hα wavelength ($\tau_{H\alpha}$). By error propagation we obtain an average standard deviation in the $\tau_{H\alpha}$ measurements of about 7%. This value, however, does not take into account the calibration uncertainties of the data.

In the galactic disk, $\tau_{H\alpha}$ ranges between 1 and 17.5, which implies that the Hα emission is not transparent and that we are only detecting photons originating in a front layer of NGC 4631. This is not surprising since NGC 4631 is an edge-on galaxy. Unfortunately, one cannot estimate the thermal emission in regions where $\tau_{H\alpha} \geq 1$ with this method. In the halo, values decrease with higher z-extent down to about 0.02.

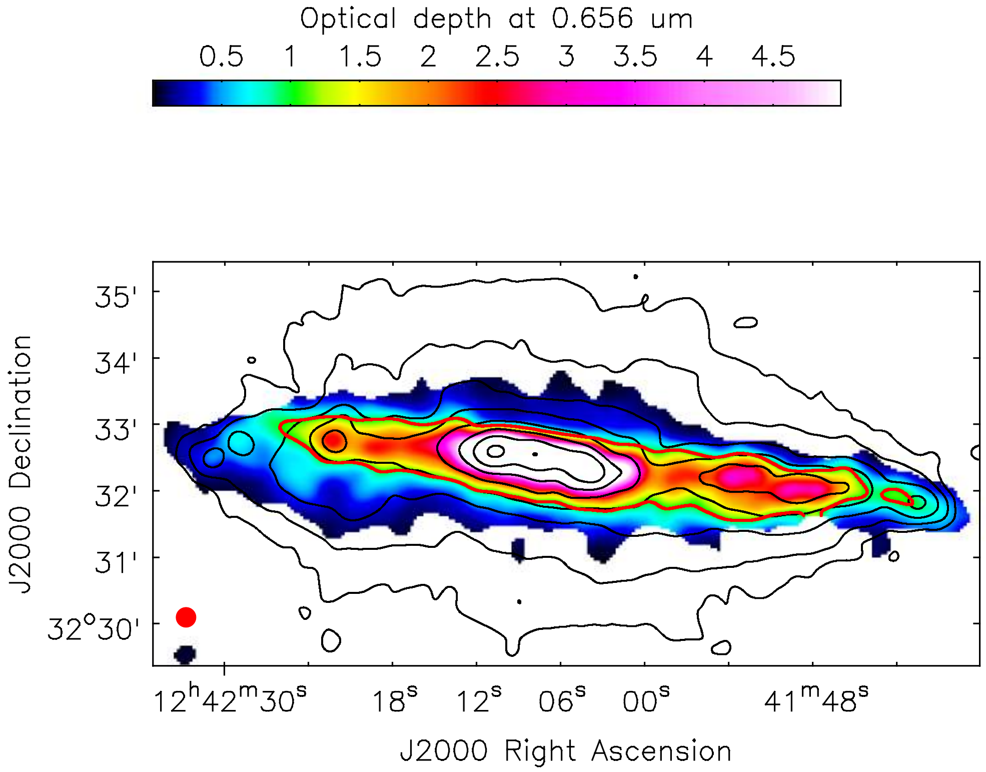

FIGURE 5.4— Dust optical depth at the Hα wavelength ($\tau_{H\alpha}$). Angular resolution is 18″ FWHM. Contour levels of the total C-band emission (EVLA + Eff.) correspond to 45 μJy/beam $\cdot$ $(3, 6, 12, 24, 48, 96, 192, 384)$. The red contour illustrates the limit $\tau_{H\alpha} = 1$. For better representation the colorscale has been saturated at $\tau_{H\alpha} = 5$.

5.2.3 Emission measures

Since the dust may not be uniformly mixed with the ionized gas we take into account an effective dust fraction along the LOS absorbing the Hα photons, so that the actual absorption is given by $\tau_{eff} = f_d \cdot \tau_{H\alpha}$. For simplicity, we assume a constant effective dust fraction throughout the galaxy of $f_d = 0.33$, obtained for the Milky Way by Dickinson et al. (2003). As T2007 have shown, the thermal fraction is not sensitive to the effective dust fraction, hence, for given purposes, assuming a constant value for the galaxy will not significantly affect the results.

Having derived the effective optical depth (τ_{eff}) responsible for the Hα extinction, one can now correct the Hα emission according to $\mathrm{H}\alpha_{corr} = \mathrm{H}\alpha_{\mathrm{obs}} \cdot \exp(\tau_{\mathrm{eff}})$. The emission measure (EM), for an optically thick medium, then follows from the extinction-corrected Hα emission (Valls-Gabaud 1998):

$$\mathrm{EM}[\mathrm{pc} \cdot \mathrm{cm}^{-6}] = \frac{\mathrm{H}\alpha_{\mathrm{corr}} \cdot \mathrm{Te_4}^{1.017} \cdot 10^{0.029/\mathrm{Te_4}}}{9.41 \cdot 10^{-8}} \tag{5.5}$$

The Hα_{corr} should be given in units of $\mathrm{erg} \cdot \mathrm{cm}^{-2} \cdot \mathrm{sec}^{-1} \cdot \mathrm{sr}^{-1}$, and $\mathrm{Te_4}$ is the electron temperature in units of 10^4 K. We adopt a typical value for the electron temperature of $\mathrm{Te_4} = 10\,000$ K.

5.2.4 Thermal emission

Subsequently, the optical depth for free-free emission and the brightness temperature of the radio continuum were derived as explained in T2007. We also adopt an electron temperature of 10 000 K to estimate the brightness temperatures. The brightness temperature ($\mathrm{T_B}$) was converted to flux-density using (Pacholczyk 1970):

$$\mathrm{S}_{\nu,\mathrm{th}}[\mathrm{Jy} \cdot \mathrm{beam}^{-1}] = 8.18 \cdot 10^{-7} \mathrm{T_B} \cdot \nu^2 \cdot \mathrm{FWHM}^2 \tag{5.6}$$

The frequency ν is in GHz, $\mathrm{T_B}$ in Kelvin and the FWHM in arcsec. The thermal emission in NGC 4631 obtained with this method is shown in figure 5.5, top panel (a) shows the thermal emission at C-band and bottom panel (b) at L-band.

5.2.5 Thermal Fraction

With the total emission radio maps presented in Chapter 4 (EVLA + Eff.), we estimated the thermal fraction obtained with this method. The thermal fractions for each corresponding frequency are plotted in figure 5.6.

For the optically thin regions ($\tau_{H\alpha} < 1$), values range at C-band from about 0.1% in the halo to 66% in the disk. The highest thermal fractions in the optically thin regime are found in the far western edge of the disk, where the HII regions CM 7,8,9 (Crillon & Monnet 1969) are located. Along the optically thick disk ($\tau_{H\alpha} \geq 1$) the thermal fractions range between 7% and 72%, except in the center of the galaxy where the thermal emission is excessively high. However, one cannot rely on the thermal emission obtained with this method for Hα optically thick regions.

5.3 Method two: thermal estimate with combination of Hα and 24 μm data

To correct the Hα radiation for extinction one can make use of a linear combination of the observed Hα (L(H$\alpha_{\rm obs}$)) and 24 μm (L(24 μm)) luminosity:

$$L(H\alpha_{corr}) = L(H\alpha_{obs}) + a \cdot \nu L_{\nu}(24\mu\mathrm{m}) \tag{5.7}$$

where the parameter a is the scaling coefficient. According to Kennicutt et al. (2009), faint galaxies with an integrated Hα luminosity below a value of 10^{42} erg/sec tend to have little dust and weak IR emission. Hence, in such galaxies the Hα contribution will dominate in equation 5.7. This might be the case for NGC 4631.

Kennicutt et al. (2009) obtained a scaling factor of a = 0.02±0.005 from integrated measurements of galaxies, and Calzetti et al. (2007) obtained a value of a = 0.031±0.006 from HII-dominated regions. According to the authors, both values appear to be independent of metallicity. It has been suggested that the difference between the two scaling factors could be due to the primary stellar population heating the dust, i.e. due to the IR cirrus problem. In HII regions the population of O-stars, which have ionizing lifetimes of about 5 Myr, dominate the gas ionization and the dust heating. On the contrary, for entire galaxies the gas ionization is still dominated by O-stars, but the dust can also be heated by older stars.

The sample of Calzetti et al. (2007) was composed of HII regions between a 24 μm luminosity range of $3{\cdot}10^{38}$ to $3 \cdot 10^{44}$ erg/sec. Taking this into consideration, we decided to make use of the scaling coefficient a = 0.031±0.006 estimated by Calzetti et al. (2007) for L(24 μm) $\geq 3 \cdot 10^{38}$ erg/sec, and we implemented the scaling factor a = 0.02±0.005 derived by Kennicutt et al. (2009) for L(24 μm) $< 3 \cdot 10^{38}$ erg/sec. Having corrected the Hα map for extinction, the same procedure was followed to derive the thermal emission and thermal fraction as described in sections 5.2.3, 5.2.4 and 5.2.5. The thermal emission obtained with this method is presented in figure 5.7 and the thermal fraction in figure 5.8. Only values above 3σ were used to obtain these plots.

This is the first time these calibrations have been applied to map the spatially resolved emission in an edge-on galaxy. Kennicutt et al. (2009) suggest to proceed with caution because at small scales the calibrations become more complex and it may depend on properties like the dust optical depth and attenuation geometry. Hence, applying these calibrations may introduce significant errors at high spatial resolution. Overall, structures follow those obtained in the thermal distribution estimated with method one (cf. fig. 5.6 and 5.8). The most noticeable feature is the drop of thermal fraction in the central region of NGC 4631. We believe this is due to severe attenuation, figure 5.4 displays that the Hα optical depth is highest for this region, which means that there is a higher concentration of dust here than anywhere else in the galaxy.

5.4 Method three: thermal estimate with only 24 μm data

Relaño et al. (2007) studied the use of 24 μm measurements as an indicator of the correction for extinction in the Hα intensities of HII regions in a wide sample of galaxies. Their sample was composed of HII regions between a 24 μm luminosity range of $1 \cdot 10^{38}$ to $3 \cdot 10^{44}$ erg/sec. They conclude that their relation between the 24 μm luminosity and the extinction-corrected Hα luminosity is independent of metallicity:

$$\log(L(H\alpha_{corr})) = \frac{\log(\nu L_\nu(24\ \mu\mathrm{m})) + (7.28 \pm 0.52)}{1.21 \pm 0.01} \tag{5.8}$$

Zhu et al. (2008) also studied this correlation but with galaxy integrated measurements for 379 galaxies of different types. These authors find the best nonlinear fit to be:

$$\log(L(H\alpha_{corr})/L_\odot) = \frac{\log(\nu L_\nu(24\ \mu\mathrm{m})/\mathrm{L}_\odot) + (0.06 \pm 0.07)}{1.18 \pm 0.02} \tag{5.9}$$

Once again we made use of the relation derived with HII regions estimated by Relaño et al. (2007) only for L(24 μm) $\geq 1 \cdot 10^{38}$ erg/sec (given the luminosity range of validity of Eq. 5.8). For the range L(24 μm) $< 1 \cdot 10^{38}$ erg/sec we implemented equation 5.9 derived by Zhu et al. (2008). Having corrected the Hα radiation for extinction, the same procedure was followed to derive the thermal emission and thermal fraction as described in sections 5.2.3, 5.2.4 and 5.2.5. The thermal emission is presented in figure 5.9 and the thermal fraction in figure 5.10. Top panel (a) corresponds to C-band with the same contours as in figure 5.4, bottom panel (b) corresponds to L-band with the same contours as in figure 5.5.b. The red contour delimits the boundary L(24 μm) = $1 \cdot 10^{38}$ erg/sec and the magenta dashed contour displays up to where there are reliable Hα measurements available. Only values above 3σ were taken into account.

With this method the thermal emission in the central region is higher compared to the estimate obtained with method two, values range between 21-60%. This is probably due to the fact that the central region has the largest concentration of dust. There are a few interesting questions that arise when considering the thermal emission derived with this method where we do not observe Hα emission. Is this thermal emission real and is it possible that the Hα observations are not sensitive enough to be detected in the halo? Or is this direct evidence of the contribution from the interstellar radiation field? The stellar populations not associated with current star formation events are known to contribute to the heating of the 24 μm emitting dust. However, Meléndez et al. (2015) state that the warm dust inside the superbubble (refer to section 5.2.1) may have been heated by UV radiation escaping the disk, X-ray emission or by shocks produced by outflows from the disk into the halo. Therefore, the emission in the halo above the central region might still be related to free-free radiation generated in the superbubble, while the emission at the outer edges of the halo may not be thermal at all and may be a result of dust heating by other mechanisms.

5.5 Comparison of methods

In Table 5.1 the integrated thermal flux-density ($S_{\rm th}$) and thermal fraction ($f_{\rm th}$) at C-band obtained with each of the three methods in particular areas of interest are displayed. For convenience we define the *central region* of the galaxy as the area within the fifth black contour in fig. 5.4 extending in right ascension between $12^h42^m00^s$ and $12^h42^m18^s$. Only pixels where the Hα emission is above 3σ were taken into account for this comparison. For the values extracted from the Hα optically thick region, corresponding to columns 4 and 5, the flux-density of the central region was excluded.

The standard deviation of the thermal flux-densities was determined by error propagation considering random errors in the maps, the uncertainty in the choice of the effective dust fraction ($f_{\rm d}$) and the deviation introduced by the errors of the calibration factors in the corresponding equations. We did not take into account the uncertainty in the determination of the electron temperature, which according to T2007 is the main error contributor. However, to relatively compare one method with respect to the other we believe this is sufficient. We consider the average standard deviation within the galaxy for each of the estimates.

TABLE 5.1— Comparison between the integrated thermal flux-density (S_{th}) and thermal fraction (f_{th}) for methods 1-3. All values obtained from the C-band data. The flux-density of the *central region* has been excluded in the area where $\tau_{H\alpha} \geq 1$.

Method	**Central Region**		$\tau_{H\alpha} \geq 1$		$\tau_{H\alpha} < 1$	
	S_{th}[mJy]	**f_{th}**	**S_{th}[mJy]**	**f_{th}**	**S_{th}[mJy]**	**f_{th}**
1	648±91	352±53%	15±2	30±4%	12±2	16±2%
2	37±5	20±3%	12±2	24±4%	12±2	17±3%
3	80±13	44±7%	20±3	40±6%	21±3	28±5%

The thermal emission where $\tau_{H\alpha} < 1$ obtained with method one and two are in excellent agreement, however, the thermal flux obtained with method three seems to be overestimated. This might be related to the fact that the 24 μm emission is not only produced by the dust heated by UV photons radiated by OB stars, there are also other contributors to the 24 μm emission as mentioned in the beginning of this Chapter. On the other hand, the Hα emission is optically thin in this region and it is a better tracer of the thermal emission. Since method one and two include Hα measurements, we obtain better approximations for the thermal emission with these two methods for the optically thin regime. For the region where $\tau_{H\alpha} \geq 1$ method three also overestimates the thermal emission with respect to method two. It is even higher than the thermal emission estimated with method one which is already expected to be overestimated since method one is no longer reliable for optically thick regions.

Smith et al. (2001) studied 48 star-forming regions within NGC 4631 at several wavelengths from the optical to the FUV. They present extinction-corrected Hα luminosities for 48 apertures that approximately include these HII regions. The extinction corrections were computed from the Balmer decrement and from the difference between the measured B-V colors and B-V colors determined from models of evolving star-forming clusters. In Table 5.2 we compare our observed (Hα_{obs}) and extinction-corrected Hα luminosities (Hα_{corr}) of the brightest star-forming regions with the values these authors obtained. The data is sorted according to the approximate HII regions complexes included in each aperture. Since Smith et al. (2001) do not state the size over which they integrated the apertures, this represents a rough comparison from which one can only obtain a general trend.

The standard deviation of the extinction-corrected Hα luminosities was estimated by propagating errors taking into account random errors in the maps, the deviation introduced by the different calibration factors in the corresponding equations and finally, the uncertainty in the determination of $\mathrm{f_d}$. We considered the average standard deviation within the galaxy. In addition, we included a 5% error due to the variation of the aperture sizes.

Overall, for the optically thin region our estimates of the extinction-corrected Hα luminosity are lower than those obtained by Smith et al. (2001). For the apertures located within the optically thick areas (excluding the central region), the resulting estimates obtained with method one and three matches closely the Hα_{corr} value computed by these authors. For the HII regions located in the central region, method two gives closer estimates to those obtained by Smith et al. (2001), while the other two methods overestimate the correction for extinction.

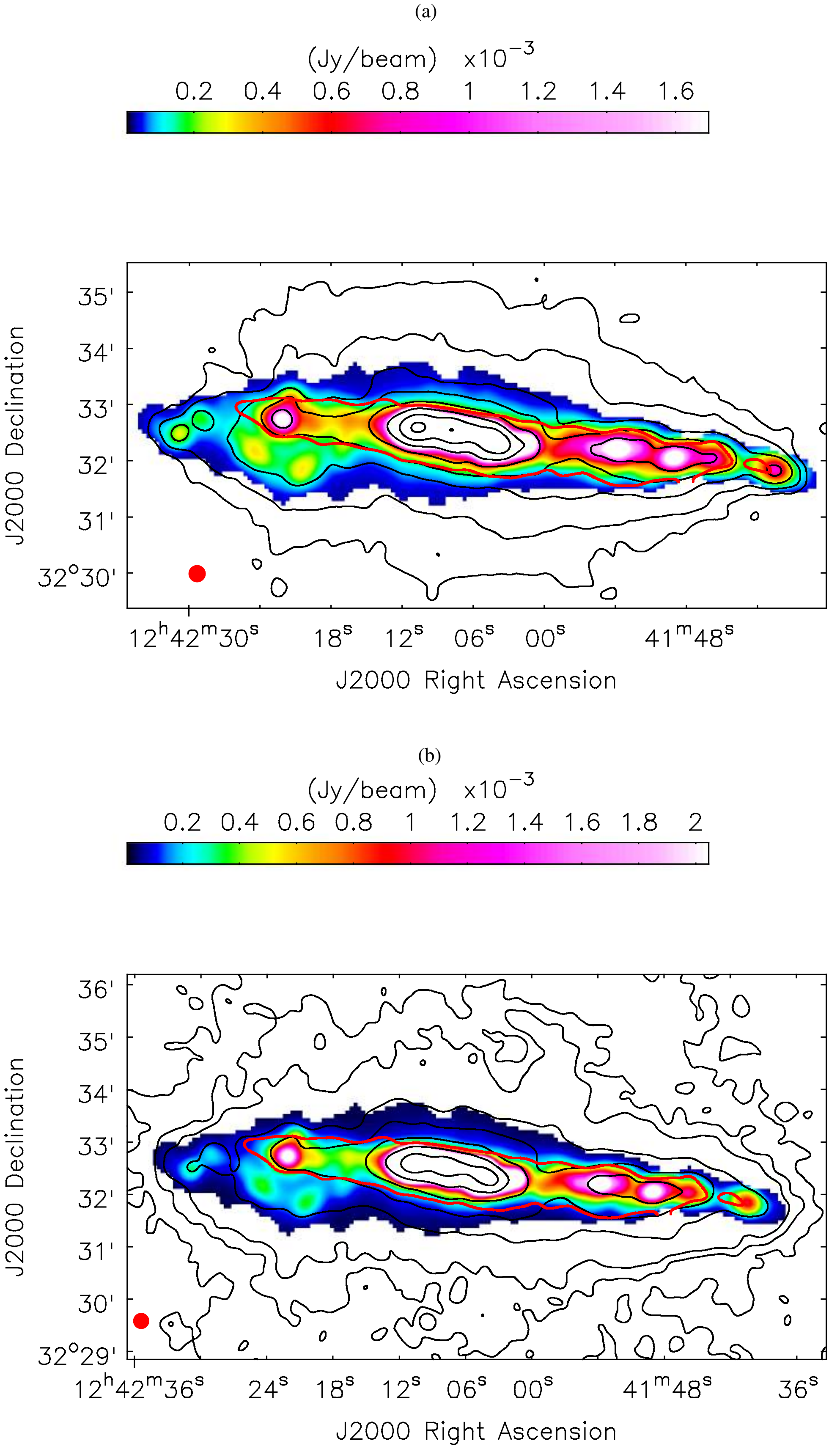

FIGURE 5.5— Thermal emission estimated with the $I_{70\mu m}/I_{160\mu m}$ (method one). Angular resolution is 18″ FWHM and the red contour illustrates the limit $\tau_{H\alpha} = 1$. Top figure (a) corresponds to C-band with the same contours as in figure 5.4. Bottom figure (b) corresponds to L-band, contours represent the total L-band emission (EVLA + Eff.): 65 μJy/beam $\cdot\ (3, 6, 9, 24, 48, 96, 192, 384)$.

(a)

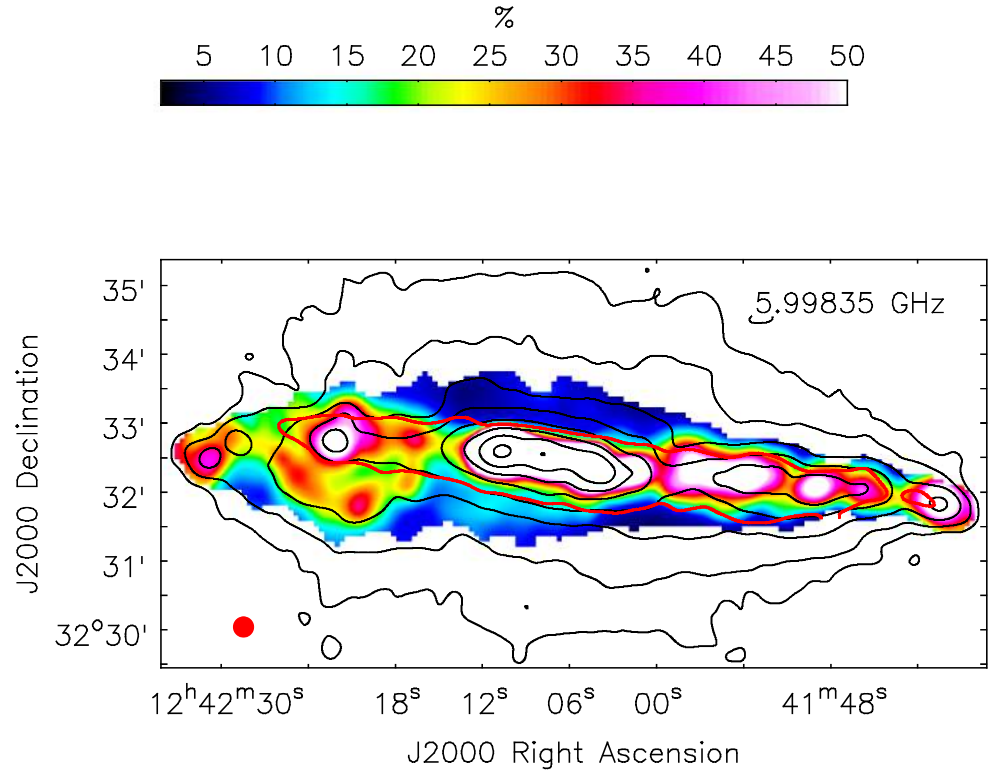

(b)

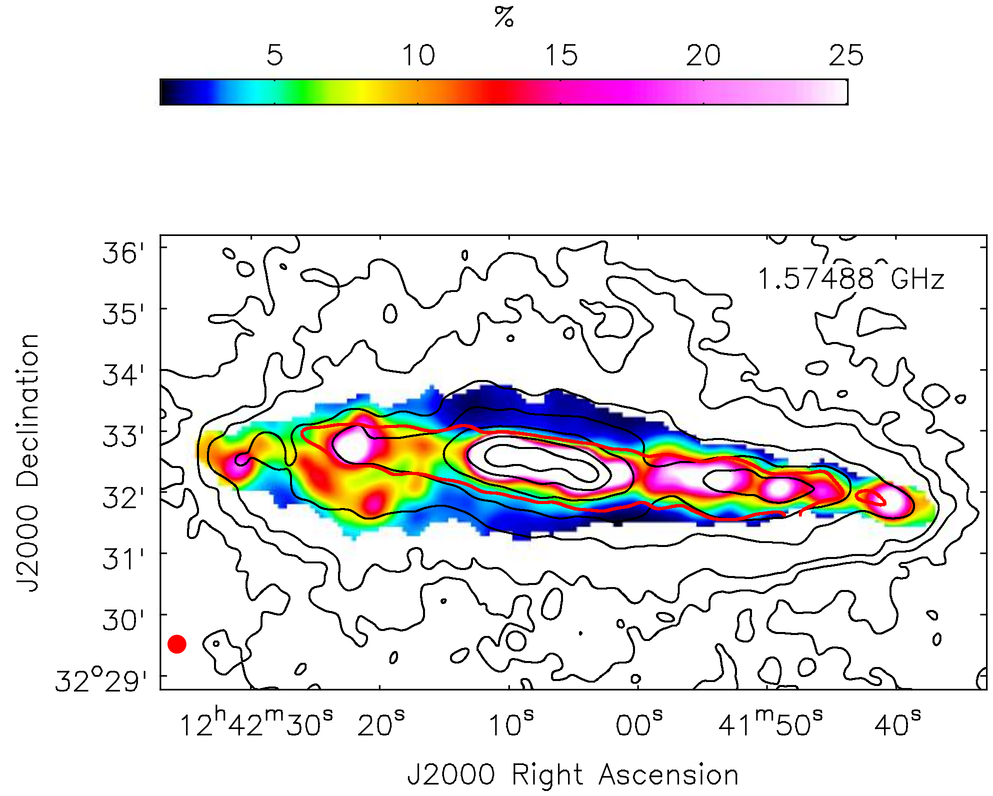

FIGURE 5.6— Thermal fraction estimated with the $I_{70\mu m}/I_{160\mu m}$ (method one). Angular resolution is 18″ FWHM and the red contour illustrates the limit $\tau_{H\alpha} = 1$. Top figure (a) corresponds to C-band with the same contours as in figure 5.4. Bottom figure (b) corresponds to L-band with the same contours as in figure 5.5.b.

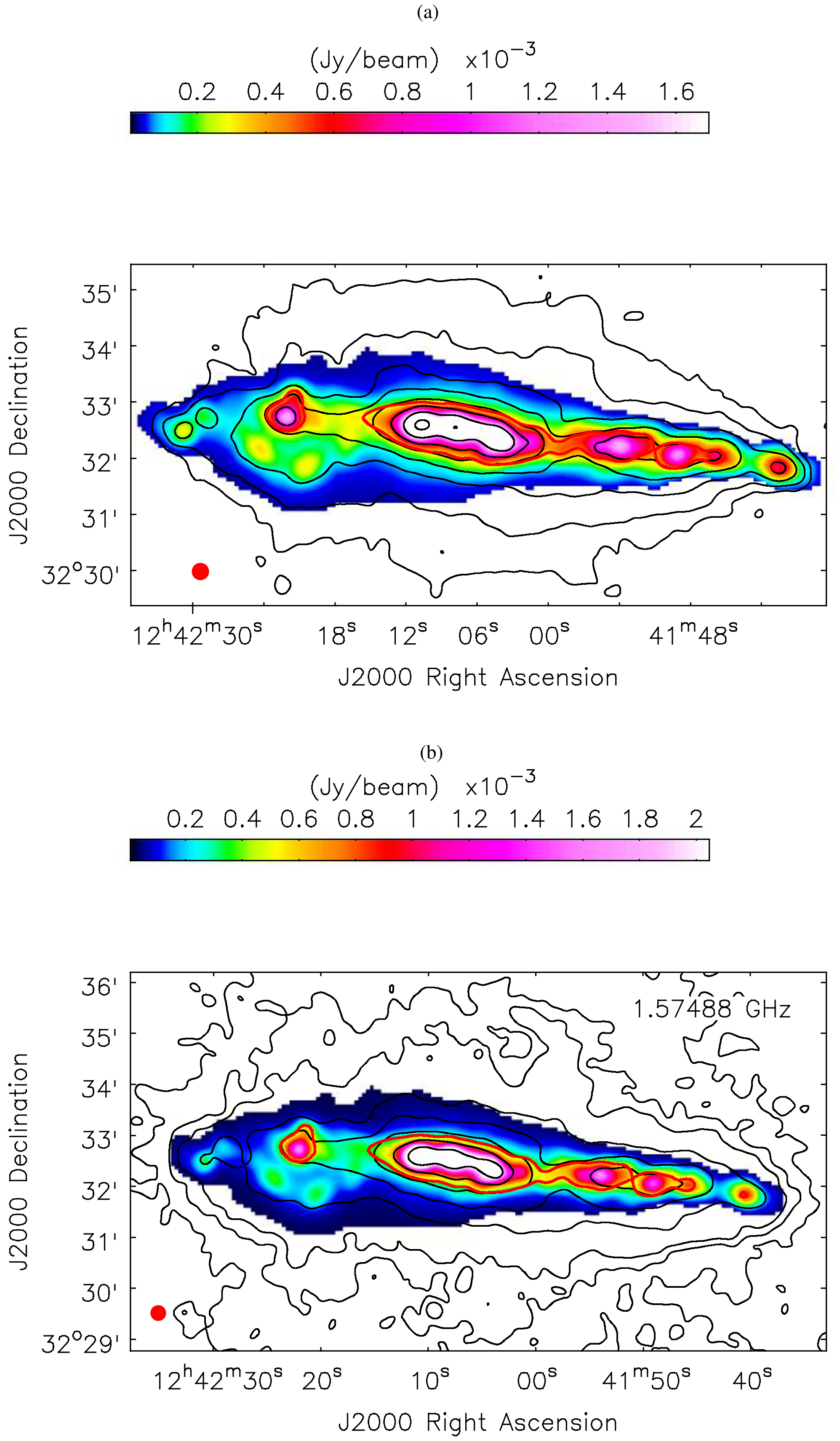

FIGURE 5.7— Thermal emission estimated with the combination of Hα and 24 μm data (method two). Angular resolution is 18″ FWHM and the red contour illustrates the limit L(24 μm) = $3{\cdot}10^{38}$ erg/sec. Top figure (a) corresponds to C-band with the same contours as in figure 5.4. Bottom figure (b) corresponds to L-band with the same contours as in figure 5.5.b.

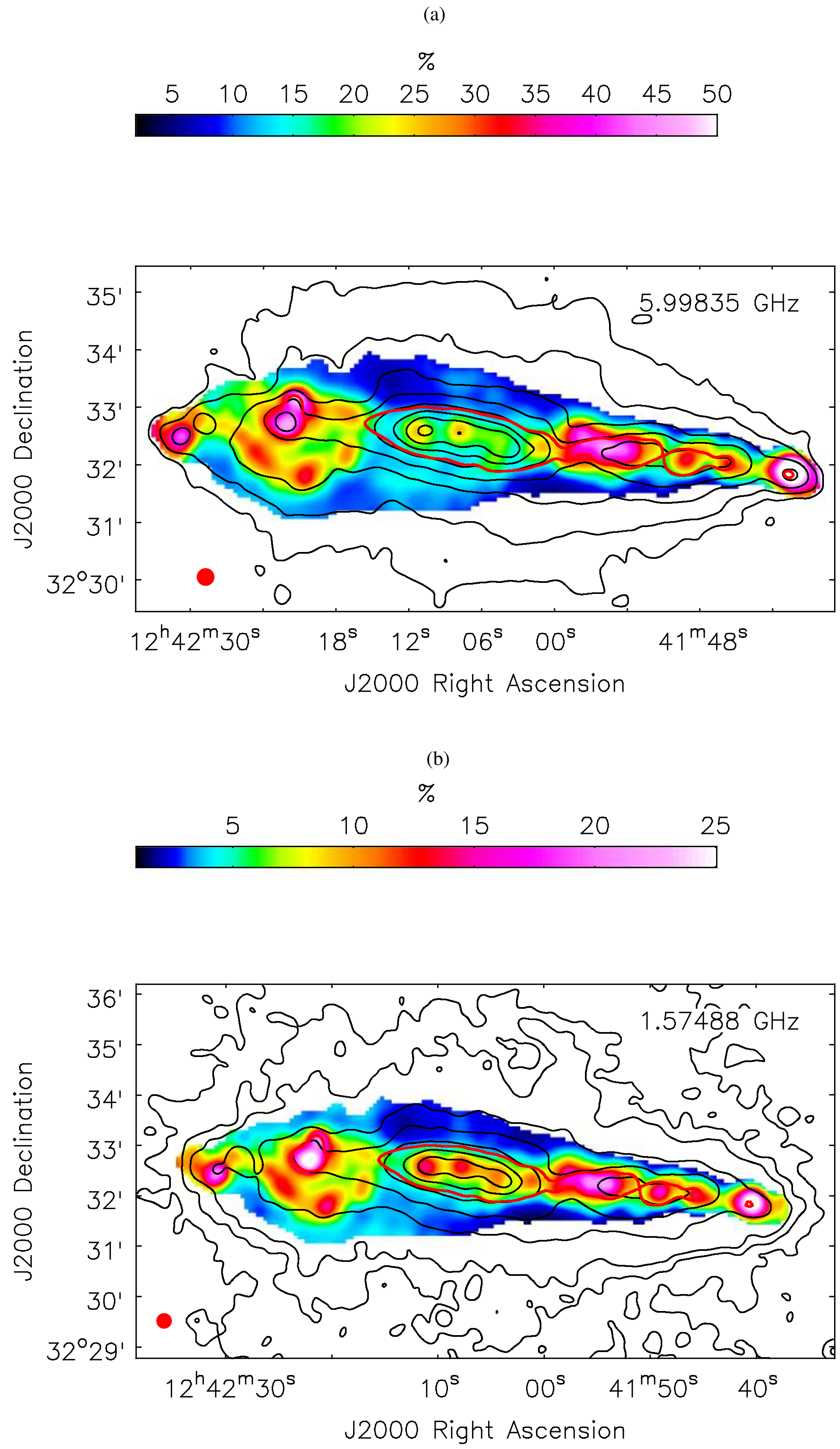

FIGURE 5.8— Thermal fraction estimated with the combination of Hα and 24 μm data (method two). Angular resolution is 18″ FWHM and the red contour illustrates the limit L(24 μm) = $3{\cdot}10^{38}$ erg/sec. Top figure (a) corresponds to C-band with the same contours as in figure 5.4. Bottom figure (b) corresponds to L-band with the same contours as in figure 5.5.b.

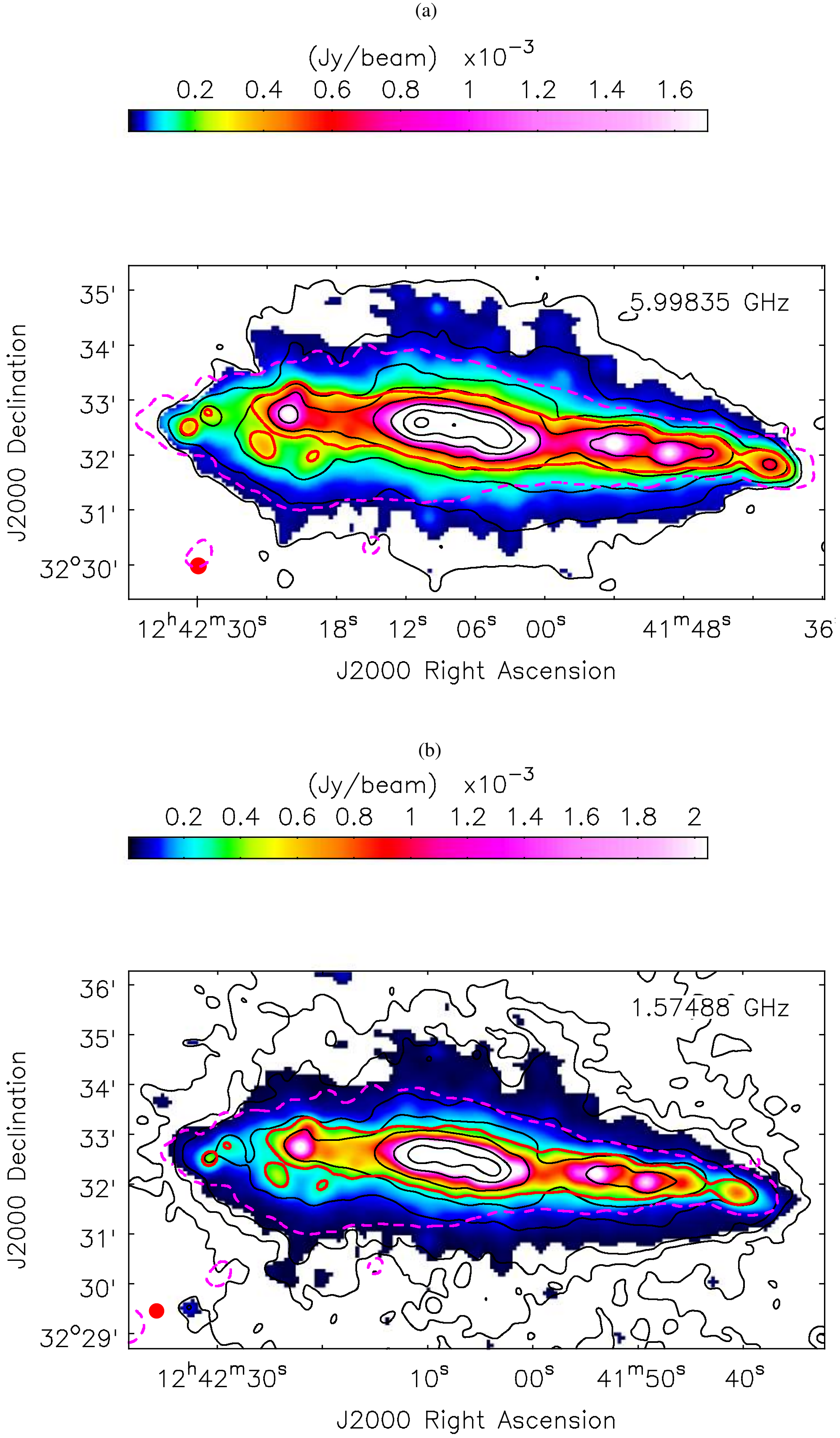

FIGURE 5.9— Thermal emission estimated with the 24 μm data (method three). Angular resolution is 18″ FWHM and the red contour illustrates the limit L(24 μm) = $1{\cdot}10^{38}$ erg/sec. The magenta dashed contour represents the 3σ cut of the Hα emission. Top figure (a) corresponds to C-band with the same contours as in figure 5.4. Bottom figure (b) corresponds to L-band with the same contours as in figure 5.5.b.

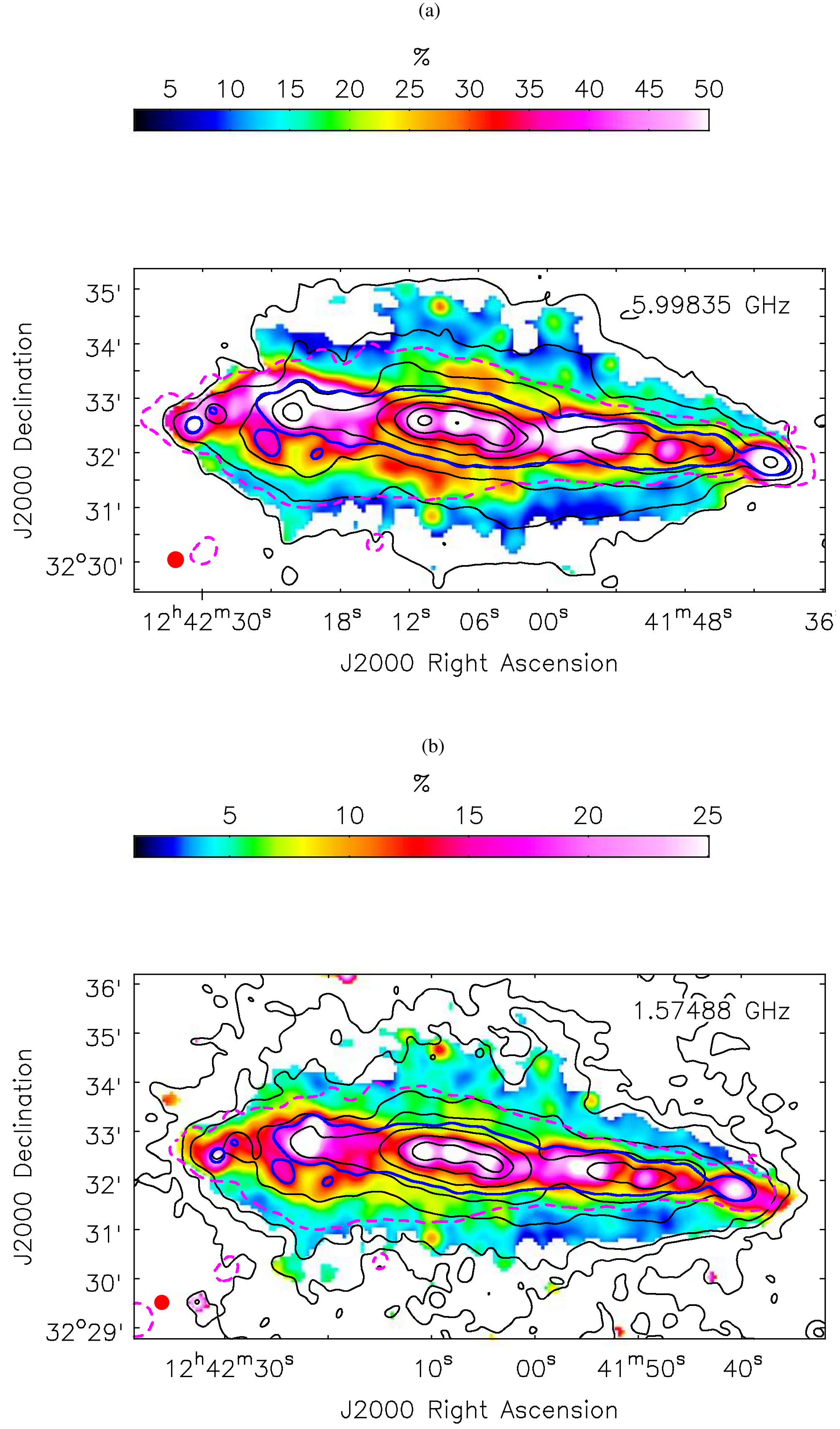

FIGURE 5.10— Thermal fraction estimated with the 24 μm emission (method three). Angular resolution is 18″ FWHM and the blue contour illustrates the limit L(24 μm) = $1{\cdot}10^{38}$ erg/sec. The magenta dashed contour represents the 3σ cut of the Hα emission. Top figure (a) corresponds to C-band with the same contours as in figure 5.4. Bottom figure (b) corresponds to L-band with the same contours as in figure 5.5.b.

TABLE 5.2— Hα observed (Hα_{obs}) and extinction-corrected (Hα_{corr}) luminosity for different regions within NGC 4631. The data is sorted according to the HII region complexes included in each aperture. All values given in units of $1 \cdot 10^{39}$ erg/sec. M1- method one, M2- method two, M3- method three.

	Central Region			$\tau_{H\alpha} \geq 1$			$\tau_{H\alpha} < 1$		
	CM 65,66,67	**CM 45,46**	**CM 52**	**CM 81**	**CM 37,38**	**CM 23,24**	**CM 85,83**	**CM 7,8,9**	**CM 77b**
Hα_{obs}	3.6±0.4	2.4±0.2	0.9±0.1	4.5±0.5	3.9±0.4	7.1±0.7	1.9±0.2	5.1±0.5	0.7±0.1
Hα_{corr}[a]	10.4±2	6.9±4.4	2.5±0.6	13.3±1.9	11.2±2.3	20.4±2.4	5.4±0.5	14.5±2.4	1.9±0.9
Hα_{corr}- M1	1566±282	16.9±3	55±10	10.8±2	11.5±2.1	18.8±3.4	2.4±0.4	6.8±1.2	0.7±0.1
Hα_{corr}- M2	15.3±2.8	4.9±0.9	5±0.9	7.2±1.3	6.3±1.1	10.6±2	2.4±0.4	6.8±1.1	0.7±0.1
Hα_{corr}- M3	40.3±8.1	11.7±2.3	15.4±3.1	12±2.4	10.8±2.2	17.8±3.6	3.4±0.7	7.3±1.5	0.6±0.1

---

[a] from Smith et al. (2001).

5.6 Final considerations for the thermal emission of NGC 4631

Method one cannot be utilized for optically thick regions and unfortunately, the entire disk of NGC 4631 is optically thick. Furthermore, method three overestimates the thermal emission with respect to the other two methods for both the optically thin and optically thick regions. The thermal emission obtained with method two is in excellent agreement with the results estimated with method one for the optically thin regime and in addition, the extinction correction obtained for the HII regions in the center of the galaxy agree with values estimated by Smith et al. (2001). Therefore, the best approximation of the thermal emission in NGC 4631 is obtained by employing method two which combines both Hα and 24 μm measurements. In the rest of this Chapter we take into account only the thermal emission estimated with this method for further analysis.

Taking into account all the uncertainties mentioned in the previous sections that contribute to the standard deviation, and additionally considering an electron temperature variation of ± 2000 K, we obtain that the average error in the thermal flux is about 19% for C-band and 17% for L-band.

Integrating the thermal emission (method two) in ellipses we obtain a total thermal flux-density of 61 ± 13 mJy at C-band and 70 ± 13 mJy at L-band. Golla et al. (1996) published a very rough estimate of the thermal flux-density of NGC 4631 at C-band (56 mJy). These authors state that at very high resolution ($1\farcs45$) the radio and Hα emission are uncorrelated due to attenuation effects, so a robust approximation of the thermal flux-density can be obtained by adding the thermal emission obtained from their Hα data and the thermal component in their radio data. They estimated the thermal component in their C-band data by assuming a constant nonthermal spectral index and a global thermal fraction at C-band of 50%. Even though their value is a very simplistic estimate, it is surprisingly close to our integrated thermal flux-density.

The error in the thermal fraction estimates is maximum 19% (15%) at C-band (L-band). The nonthermal emission obtained by subtracting the thermal component from the total radio maps is shown in figure 5.11. Within NGC 4631, the thermal contribution to the radio emission ranges between 4-60% (1-30%) at C-band (L-band). The highest values coincide with the HII regions CM 7,8,9 located at the far western edge of the galaxy. Tabatabaei et al. (2007) also report a thermal fraction at λ 3.6 cm (λ 20 cm) of up to $77.8\pm4.6\%$ ($74.6\pm3.4\%$) in HII region complexes of M 33. By integrating the emission of the entire galaxy we obtain a global thermal fraction at C-band of $15\pm3\%$ and at L-band of $6\pm1\%$. These values agree with those published by Mora & Krause (2013).

In figure 5.12 the thermal emission at C-band estimated with method two is shown as a colorscale together with contours of the soft X-ray emission. The plot shown in figure 5.12 displays an overall correlation between the coronal gas and the thermal emission of NGC 4631. The brightest X-ray feature is located above the central region, Wang et al. (1995) found this X-ray feature appears to be connected to Hα filaments emerging from the galaxy's disk. The red circles in this figure indicate the approximate size of the HI supershells (refer to Chapter 2) found by Rand & van der Hulst (1993). The bright thermal peak to the east of the central region ($\alpha_{2000} = 12^h42^m22^s, \delta_{2000} = 32°32'44\farcs5$), where the HII region CM 81 is located, coincides not only with an X-ray and radio peak, but also with the HI supershell 1. The HI supershell 2, located close to the HII regions CM 37, 38, also coincides with an emission peak seen in the thermal, X-ray and radio ($\alpha_{2000} = 12^h41^m55^s, \delta_{2000} = 32°32'15\farcs5$).

We have also plotted in figure 5.12 the brightest X-ray sources that have been found in NGC 4631 with an X-symbol. Source *ULX1* ("$No.$ 7" in Read et al. (1997)) and *ULX5,ULX6* ("$X5,X4$" in Soria & Ghosh (2009); "$H7,H8$" in Vogler & Pietsch (1996)) are believed to be related to the HI supershells. In addition, the *ULX3* coincides spatially with the HII region CM 67. Soria & Ghosh (2009) conclude that the sources ULX 3-6 are consistent with accreting stellar-mass black holes with masses $\lesssim 50\ \mathrm{M}_{\odot}$. The source *ULX8* was identified by Vogler & Pietsch (1996) ("$H10$") to be tentatively located in the outer spiral arm of NGC 4631.

5.7 Discussion

Analyzing the resulting thermal emission of NGC 4631 obtained with method two one gets the impression the thermal fraction in the central area of the galaxy is of the same order of magnitude or even less than in the outer disk (see fig. 5.8). NGC 4631 is known to have star formation widely distributed along its disk and not concentrated solely in the central region as in other galaxies. However, there are still several indicators that the center of the galaxy is probably undergoing the highest star formation activity with respect to the outer disk. The strongest molecular emission, known as the *central molecular ring* by Irwin et al. (2011), is concentrated in the central region of the galaxy and coincides with the brightest radio emission. In addition, the strongest X-ray emission is located over this central molecular ring. Furthermore, the Hα optical depth is most intense in the central region, which leads us to believe there is still more thermal emission in this region originating in the inner layers of NGC 4631 that we cannot detect.

Martin & Kern (2001) performed narrowband imaging in the [O III] and Hα lines, together with long-slit spectroscopy of the halo in NGC 4631. These authors conclude the halo gas is composed of multiple phases with different ionization conditions, which in some cases are separated by dust. Therefore, the ionization in some areas may be higher with respect to the values we can measure. If we take into consideration the emission in the disk, this picture becomes much more complicated due to the longer LOS. Hence, a more elaborated approach in which stars and dust are mixed together in a complex geometry at distinct positions along the LOS will be needed to derive better extinction calibrations. On the other hand, the same stars responsible for the thermal emission, when reaching the end of their lives become the source of cosmic ray electrons that gyrate around magnetic field lines producing nonthermal synchrotron emission. So areas close to high star formation regions are also known to have strong synchrotron emission. Cosmic ray electrons can remain visible, typically, for as long as 10^8 years after the star formation event that produced them (but with the presence of a strong magnetic field this may be less). Therefore, it is difficult to propose an overall percentage of the thermal emission in the central region, and in addition, to infer which of the two components really dominate at C-band for this area within NGC 4631.

There are several galaxies that contain a layer of diffuse ionized Hydrogen, known as diffuse ionized gas (DIG). Example of these galaxies is our Milky way (Reynolds 1990) and the edge-on galaxy NGC 891 which has an Hα halo extending up to at least 5 kpc above the plane (Hoopes et al. 1999). In addition, UGC 9242 is another galaxy with diffuse Hα emission extending 4-5 kpc above the midplane (Hoopes et al. 1999). DIG is less dense than HII regions, with an electron density of $n_e \approx 0.2$ cm^{-3} versus $n_e \approx 10^2 - 10^4$ cm^{-3} in HII regions, but has a similar temperature of about ~ 8000 K (Reynolds 1990).

In our maps we indeed see a layer of thermal emission, which might be produced by DIG, extending north up to $\sim$ 2 kpc above the major axis in the central region and stretching south to about ~ 3 kpc in the eastern part of the galaxy. However, we could not detect any thermal emission at the position of the dwarf elliptical companion, NGC 4627, to confirm that the spectrum of NGC 4631 flattens at this position due to thermal emission from the companion galaxy (refer to section 4.3). Donahue et al. (1995) may have found Hα emission extending up to 18.2 kpc above the central region of NGC 4631. They even report the tentative detection of an Hα sheet of emission between NGC 4631 and its companion galaxy NGC 4656. These results, however, were never confirmed with follow-up observations.

According to nuclear starburst models (Tomisaka & Ikeuchi 1988; Heckman et al. 1990), the supernova heated gas blown out into the halo through superbubbles and chimneys might give rise to the X-ray halo seen in NGC 4631. In this context, if the hot gas cools it may become a source of Hα line radiation. For NGC 891 it has been suggested that the huge Hα halo might be originated by a combination of cooled X-ray gas and leakage of photons from OB stars located in the disk (Bregman & Pildis 1994; Rand 1997; Hoopes et al. 1999). However, Rand et al. (1992) suggest that the hot gas in NGC 4631 might not have had time to cool down due to its higher level of star formation activity compared to NGC 891. These authors conclude that NGC 4631 has higher star formation activity since this galaxy has higher radio and Hα luminosities, but comparable FIR luminosity to NGC 891. This might explain why the Hα halo is not as extended in NGC 4631 as it is NGC 891.

What still remains unclear is the source of ionization of the DIG layer in NGC 4631. Is it photoionized by the escape of UV photons from the disk, could it be ionized as the result of shocks in the halo or is there really ongoing star formation at such z-extent? Martin & Kern (2001) compare different models to address these questions. They found evidence for a multiphase structure to the DIG, including a dusty component, and two other components with low and high ionization. They tentatively relate the high ionization component to shocks. In addition, with models of cooling clouds they conclude that the radiative cooling of the X-ray emission could generate part of the DIG.

5.8 Conclusions

We derived the thermal emission and thermal fraction of NGC 4631 on a pixel-by-pixel basis at two frequencies with three different approaches. Method one is based on the technique developed by Tabatabaei et al. (2007), which consists of correcting the Hα emission for extinction with the $I_{70\mu m}/I_{160\mu m}$. The second method combines Hα and 24 μm data to correct for extinction and uses the calibrations estimated by Calzetti et al. (2007) and Kennicutt et al. (2009). Method three corrects for extinction using only 24 μm measurements and the calibrations derived by Zhu et al. (2008) and Relaño et al. (2007). In addition, we separated the nonthermal component of the radio emission. The main conclusions are the following:

1. The dust temperature estimates, derived with 70 and 160 μm measurements, are well in accordance with those calculated with SED fitting between 70-500 μm (Meléndez et al. 2015).

2. The Hα emission is optically thick along the entire disk of NGC 4631 and it becomes optically thin with higher z-extent. Hence, the Hα emission detected in the region of the disk probably originates in the outer layers of NGC 4631. Therefore, the thermal/nonthermal separation method developed by Tabatabaei et al. (2007) should be applied with caution to edge-on galaxies due to the optically thick nature of the disk emission.

3. The calibration of Kennicutt et al. (2009) to correct the Hα emission for extinction with a combination of Hα and 24 μm measurements yields results similar to method one in optically thin regions. Therefore, we state that this calibration can be used at small spatial scales for optically thin regions.

4. The calibrations of Zhu et al. (2008) and Relaño et al. (2007), which scale the 24 μm luminosity to the extinction-corrected Hα emission (method three), overestimate the correction for extinction in the optically thin and optically thick regions when compared to results obtained with the other two methods.

5. The purpose of using three different methods to estimate the thermal emission of NGC 4631 was to determine the best approach to account for dust extinction in the context of edge-one galaxies. We conclude that the most promising approach to estimate the thermal emission for NGC 4631 is achieved by employing method two, i.e. using the calibrations that combine Hα and 24 μm data to correct for extinction. This is the first time the thermal and nonthermal distribution has been derived for an edge-on galaxy.

6. The integrated thermal flux-density of NGC 4631 is 61±13 mJy at C-band and 70±13 mJy at L-band. This corresponds to a global thermal fraction at C-band (L-band) of 15±3% (6±1%). These values agree with those in the literature.

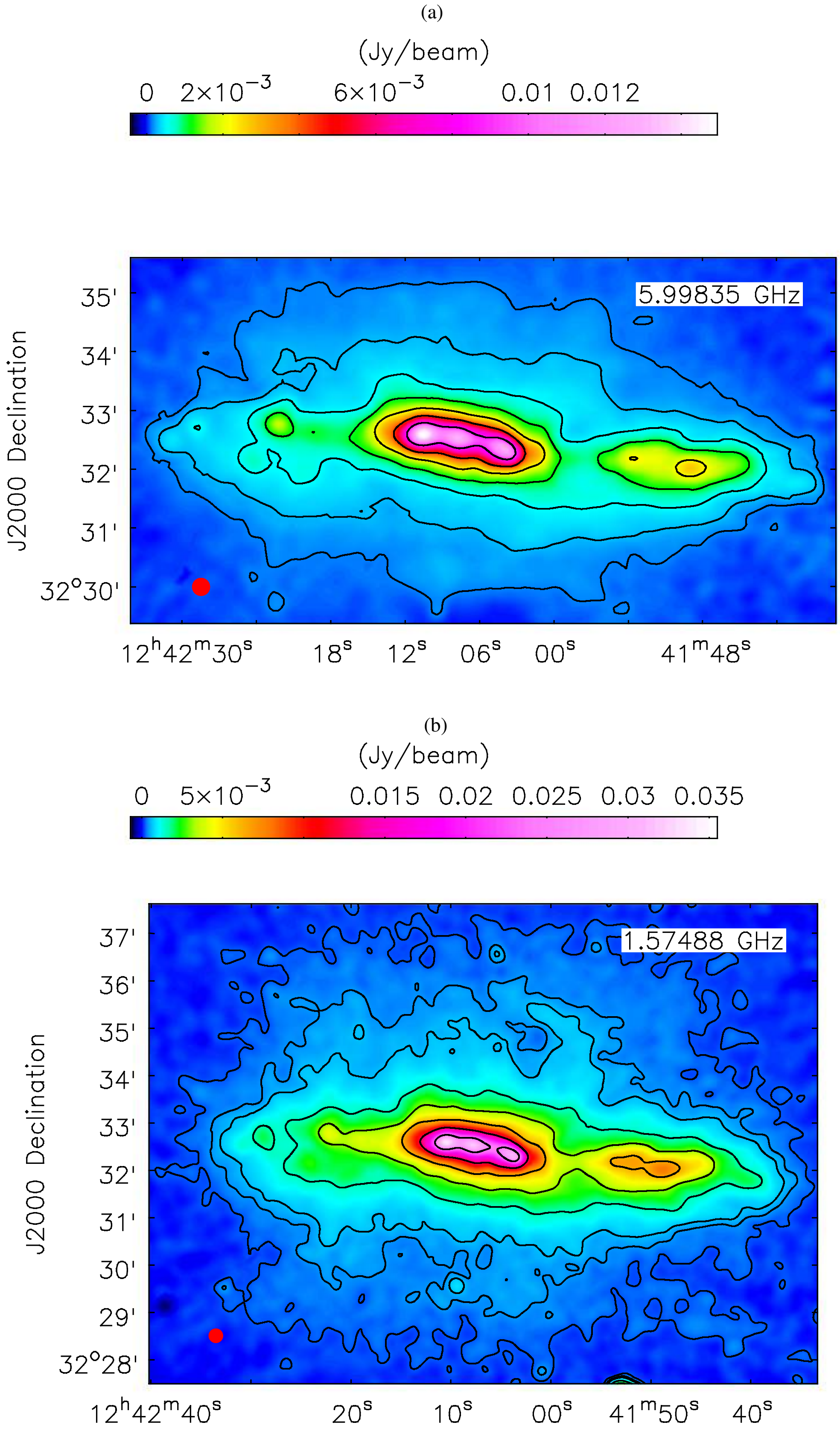

FIGURE 5.11— Nonthermal emission estimated with method two. Angular resolution is 18″ FWHM. Top figure (a) corresponds to C-band, contours represent the C-band nonthermal emission: 45 μJy/beam $\cdot$ $(3,6,12,24,48,96,192,384)$. Bottom figure (b) corresponds to L-band, contours represent the L-band nonthermal emission: 65 μJy/beam $\cdot$ $(3,6,9,24,48,96,192,384)$

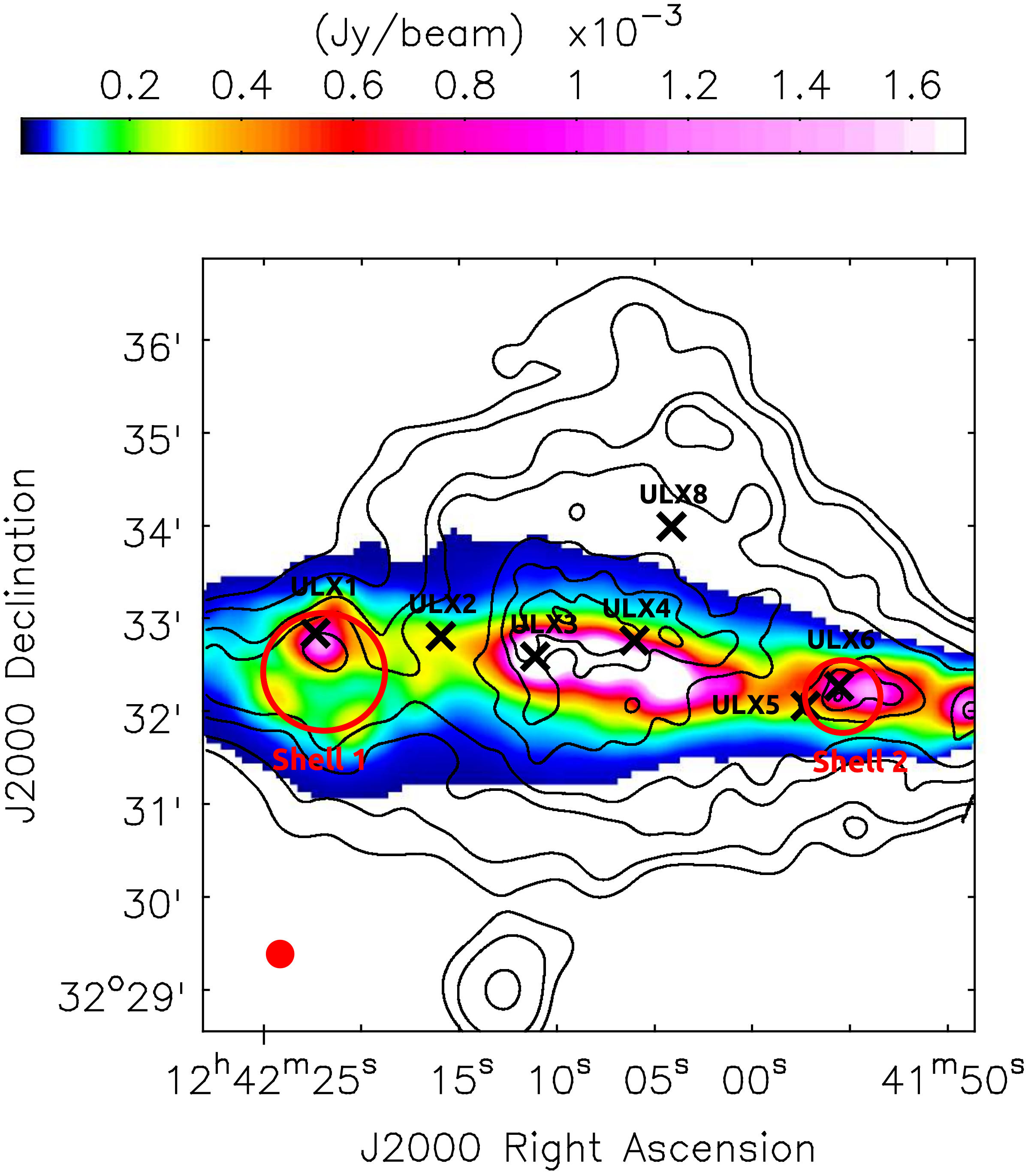

FIGURE 5.12— Thermal emission at C-band estimated with method two (18″ FWHM). Contours corresponds to the soft X-ray emission from Wang et al. (2001). The brightest X-ray sources are marked with an X-symbol and the red circles represent the approximate size of the HI supershells.

6

Synchrotron Emission and Polarization Properties

> *"Your theory is crazy,*
> *but it's not crazy enough to be true!"*
> Niels Bohr

In Chapter 5 we separated the thermal and nonthermal components of the radio emission. This is important as only through synchrotron emission we are able to directly quantify the properties of the magnetic field and the cosmic ray propagation within NGC 4631. In section 6.1 of this chapter we analyze the synchrotron emission derived as a result of this separation and in section 6.2 we study the characteristics of the polarized emission together with the magnetic field direction, orientation and strength in NGC 4631.

6.1 Results and analysis of the synchrotron emission

The synchrotron emission obtained by subtracting the thermal radiation from the total radio maps was shown in figure 5.11 for both C-band and L-band. This is the first time the distribution of the nonthermal emission has been derived for an edge-on galaxy on a pixel-to-pixel basis. In section 6.1.1 we describe its vertical scale heights, and in section 6.1.2 we analyze the spectral distribution of the nonthermal emission between C-band and L-band.

6.1.1 Vertical scale heights

Cosmic ray electrons are believed to be accelerated by supernova explosions in star forming regions. These CREs propagate into the halo giving rise to a large vertical synchrotron distribution which can be quantified as the scale height. The vertical scale heights of the synchrotron emission were determined at C-band and L-band at an angular resolution of 15″ following the same methodology described in section 4.2. The emission profiles were derived in a similar manner as for the total power radiation, i.e. along 3 strips perpendicular to the disk midplane of 180″ width each, in order to compare the effect of the thermal subtraction. Once again the two-component exponential model fitted the data best at both wavelengths. The corresponding values for the scale heights of the thin and thick disks are summarized in Table 6.1.

TABLE 6.1— Vertical scale heights of the first (h_{thin}) and second (h_{thick}) components of the exponential fits to the profiles of the synchrotron emission. N = north and S = south. The western (W), central (C) and eastern (E) strips have a width of 180″ each.

Strip	Range [″]	C-band		L-band	
		h_{thin} [pc]	h_{thick} [pc]	h_{thin} [pc]	h_{thick} [pc]
NE	-270 to -90	258±40	3992±146	660±33	5139±174
NC	-90 to 90	281±38	2259±144	664±59	4144±356
NW	90 to 270	343±21	3870±151	716±34	4866±276
SE	-270 to -90	1800±92	4669±2224	1995±98	4237±1603
SC	-90 to 90	281±38	2479±169	664±59	3337±320
SW	90 to 270	595±50	2928±287	1256±59	5043±766
Mean		291±26[a]	3366±811	676±20[a]	4461±555

---

[a] Excluding the SE and SW strips, see text for details.

It seems we have not detected a synchrotron-emitting thin disk in the southeastern side of the galaxy since the scale height of the first component to the fit in the SE strip is larger by a factor of 3-7 (2-3) at C-band (L-band) than the scale heights of the thin disk in the other parts of the galaxy. As mentioned in section 4.2, we believe this might be associated with the disturbance in this side of the disk and/or it might be an indication that the eastern part of the disk is warped. Both scenarios seem to be related to the gravitational interaction the galaxy is undergoing. Furthermore, in the southwestern side of the galaxy we have the second largest scale height of the first component at both wavebands. The scale height of the SW region is about a factor of 2 at both frequency bands larger than the thin disk scale heights in the other areas of the galaxy (excluding the SE strip). It is interesting to point out this is where the smaller HI supershell is located (see fig. 5.12). Thus, it might also not be possible to detect a thin disk in the southwestern area of NGC 4631. We have therefore excluded the southeastern and southwestern strips when estimating the mean values of the thin disk scale height presented in Table 6.1.

On average, the scale heights of the nonthermal thin disk at C-band are $\sim 22\%$ (excluding the SE and SW strips) larger than those of the total radio thin disk (cf. Table 4.1). This is expected since the total radio scale heights are influenced by thermal emission and the CREs that produce synchrotron emission propagate farther away from the star-forming regions than the nonrelativistic electrons that produce thermal emission. Since the thermal contribution is not as large at L-band as it is at C-band, the thin disk scale heights increased on average only by about 9% at L-band (excluding the SE and SW strips). The scale heights of the thick disk (second component) at both frequencies, however, remained constant within the errors since the thermal emission is concentrated towards the disk and has a lower impact in the halo. The scale heights of the nonthermal emission at L-band are higher than those at C-band. This is due to the fact that the high energy CREs lose their energy faster than the lower energy ones, and therefore, the low energy particles manage to propagate to higher distances above the plane.

6.1.2 Spectral index distribution

The nonthermal spectral index distribution plotted in figure 6.1 was derived taking into account the nonthermal emission at C-band and L-band. Values were clipped at 3σ of the Hα emission from which the thermal radiation was derived, and in addition, pixels were clipped at 3σ of the total power maps. The largest error in the nonthermal spectral index values is 0.13 and decreases with increasing intensity. This error includes the uncertainty related to the standard deviation in the total radio maps and a 19% (17%) uncertainty in the C-band (L-band) thermal flux estimate (refer to section 5.6).

TABLE 6.2— Ratio between the total and nonthermal spectral index ($\alpha_{\mathrm{tot}}/\alpha_{\mathrm{nth}}$) obtained in spatially resolved regions of NGC 4631. The thermal fractions at C-band ($f_{\mathrm{th,Cband}}$) have also been included.

Region	$\mathbf{f_{th,Cband}}$	$\alpha_{\mathbf{tot}}/\alpha_{\mathbf{nth}}$
CM 7,8,9	$55 \pm 10\%$	0.64
CM 81	$42 \pm 8\%$	0.72
Hα optically thick[a]	$24 \pm 5\%$	0.85
Central region	$20 \pm 4\%$	0.88
Hα optically thin	$17 \pm 4\%$	0.91

---

[a] Excluding central region.

The ratio between the total and nonthermal spectral index obtained in spatially resolved regions of NGC 4631 is shown in Table 6.2. For convenience we define

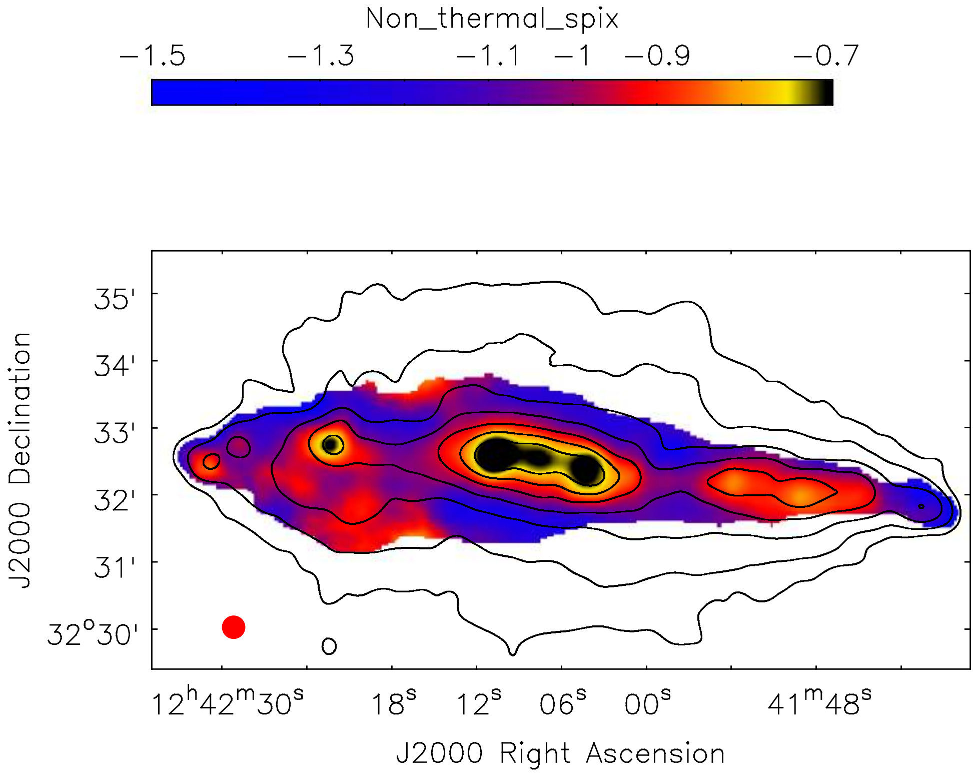

FIGURE 6.1— Nonthermal spectral index distribution derived between C-band and L-band. Values were clipped at 3σ of the Hα emission from which the thermal radiation was derived, and they were also clipped at 3σ of TP. All data plotted has an angular resolution of 20.5″. Contour levels are given by the C-band total power emission: 60 μJy/beam $\cdot\,(3,6,12,24,48,96,192,384)$.

the *central region* of the galaxy as the area within the fifth black contour in fig. 6.1 extending in right ascension between $12^h42^m00^s$ and $12^h42^m18^s$. As expected, the ratio $\alpha_{\rm tot}/\alpha_{\rm nth}$ is below unity for all areas where we managed to estimate a thermal flux. The higher the thermal fraction the steeper the nonthermal spectral index is with respect to the total spectral index. For a thermal fraction of 20% at C-band, we have a correction of about 12% in the spectral index values between L-band and C-band due to the thermal contribution.

Cosmic ray electrons in supernova remnants are believed to have an average spectrum of about −0.5, as expected from Fermi acceleration (Green 2002). This value, however, might be a bit steeper or flatter depending on the type of SNR. In the disk, the flattest spectral index is $\sim -0.7 \pm 0.05$ which implies that the CREs might have already propagated from their source of origin or this might be an indication of dominating synchrotron losses. We will discuss this further in section 6.3.1.

6.2 Results and analysis of the polarized emission

6.2.1 Polarized intensities and orientation of the intrinsic magnetic field in the sky plane

The RM-synthesis algorithm was utilized to derive the polarization properties of NGC 4631, please refer to section 3.5 for details concerning the algorithm. At C-band, the RM-synthesis cubes were sampled between -2000 to 2001 $\mathrm{rad \cdot m^{-2}}$ with a stepsize of 10 $\mathrm{rad \cdot m^{-2}}$. At L-band, the cubes were sampled between -1000 to 1001 $\mathrm{rad \cdot m^{-2}}$ with a stepsize of 5 $\mathrm{rad \cdot m^{-2}}$. The resulting resolution and scale in Faraday space at each corresponding frequency band are presented in Table 6.3.

TABLE 6.3— Maximum Faraday resolution ($\delta\phi$) and maximum scale in Faraday space ($scale_{max}$) at each corresponding frequency band obtained with RM-synthesis.

Frequency Band	$\delta\phi$ [$\mathrm{rad \cdot m^{-2}}$]	$scale_{max}$ [$\mathrm{rad \cdot m^{-2}}$]
C-band	2065	1691
L-band	107	126

In order to remove the sidelobes, the cubes were cleaned with the RM-clean algorithm (Heald et al. 2009) down to the 5σ level of the Q/U cubes. To apply the bias correction to the polarized intensity cube the average value for each pixel along the Faraday axis was estimated in areas free of emission and this approximation was then subtracted from the polarized intensity cube.

The polarized intensity at any given pixel was determined by taking the amplitude of the strongest peak along the Faraday axis of the bias-corrected polarized intensity cube. The position of this peak defines the Faraday depth value (rotation measure). The polarization angles were extracted from the Q and U cubes at the same position along the Faraday axis and were corrected with the corresponding Faraday depth value to obtain the intrinsic magnetic field orientation. The polarization angles were determined only where Stokes Q and U exceeded a 5σ threshold.

Estimates of the polarized emission obtained at C-band are shown in figures 6.2 and 6.3, at an angular resolution of $7''$ and $20.''5$, respectively. The degree of polarization is presented in figure 6.4. This is the first time the polarized emission of NGC 4631 has been observed at such high resolution. In general, the results agree with those of Golla & Hummel (1994). Thanks to the higher sensitivity of our observations and to the application of the RM-synthesis algorithm, we recovered more polarized emission at this wavelength with respect to previous observations.

At high resolution, the four peaks of polarized emission described by Golla & Hummel (1994) are now resolved into a complex of smaller features. With respect to the eastern peak of the triple radio source (see Chapter 2) at position $\alpha_{2000} = 12^h42^m11^s; \delta_{2000} = 32°32'30''$, the northwestern quadrant of the galaxy has the brightest polarized intensities and the highest degree of polarization. A similar trend can be observed at λ3.6 cm (fig. 7.2).

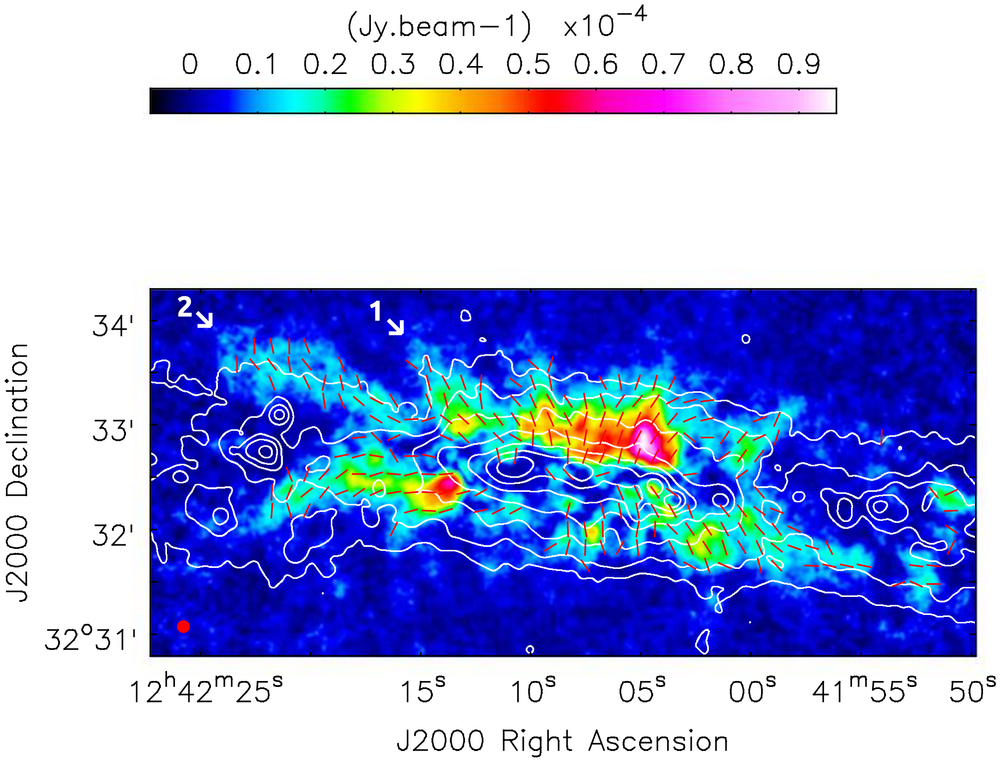

FIGURE 6.2— Polarized emission of NGC 4631 at C-band (C&D array) with intrinsic magnetic field vectors obtained with RM-synthesis. Polarization angles were clipped at 5σ of Stokes Q/U. Contours correspond to the C-band total power emission (EVLA + Eff.). All data plotted has an angular resolution of $7''$. Contour levels are given by 19 μJy/beam $\cdot$ (3, 6, 12, 24, 48, 96, 192, 384). Polarized spurs in the northeastern quadrant have been labeled 1-2.

The linearly polarized emission obtained at L-band is presented in figure 6.5 at a resolution of $20''.5$, and in figure 6.6 at a resolution of $51''$. The corresponding degrees of polarization are depicted in figures 6.7 and 6.8. Even though the polarized intensities were derived with interferometer data only, the polarized emission observed at C-band shows signs of being only slightly affected by missing short spacings. At L-band this effect is almost negligible since the missing large-scale flux in the L-band total power emission was of only 11% (refer to section 4.6) and structures in polarized emission are usually on smaller scales.

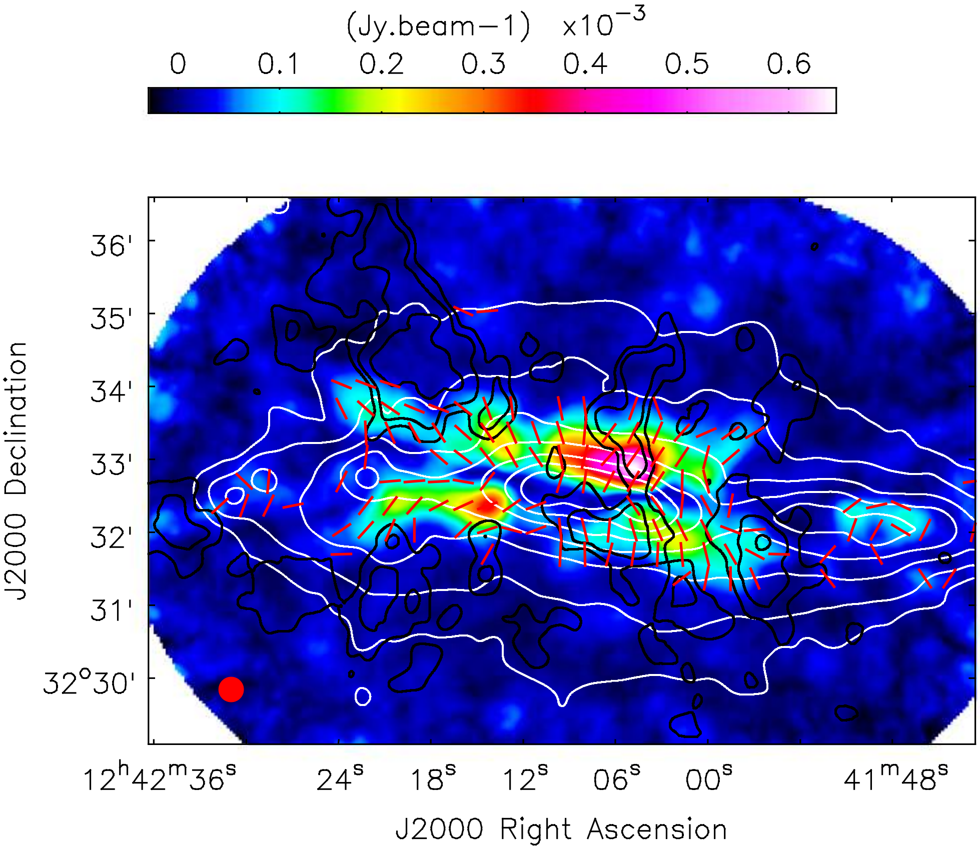

FIGURE 6.3— Polarized emission of NGC 4631 at C-band (D array) with intrinsic magnetic field vectors obtained with RM-synthesis. Polarization angles were clipped at 5σ of Stokes Q/U. All data plotted has an angular resolution of 20.″5. White contours correspond to the C-band total power emission (EVLA + Eff.): 60 μJy/beam · (3, 6, 12, 24, 48, 96, 192, 384). Black contours correspond to the polarization detected at L-band (C&D array): 35 μJy/beam · (3, 4.5, 7).

Due to the increase of Faraday depolarization effects with decreasing frequency, the polarized emission at C-band is more concentrated towards the inner halo than at L-band. Opposed to what is observed at C-band, the highest polarized intensities and polarization fractions at L-band are found in the northeastern quadrant of the galaxy. This is attributed to a spur-like feature observed at L-band that extends towards the northeastern halo of NGC 4631. This spur is clearly visible in figure 6.5, it has a polarization degree of up to 45%. As has already been pointed out in the literature, this feature coincides with the NE-radio spur observed in total power (refer to section 4.1). Furthermore, at the base of this spur one can distinguish it has spur-like counterparts at C-band (spur 1 in fig. 6.2 and also see fig. 6.3) and at λ3.6 cm (refer to fig.

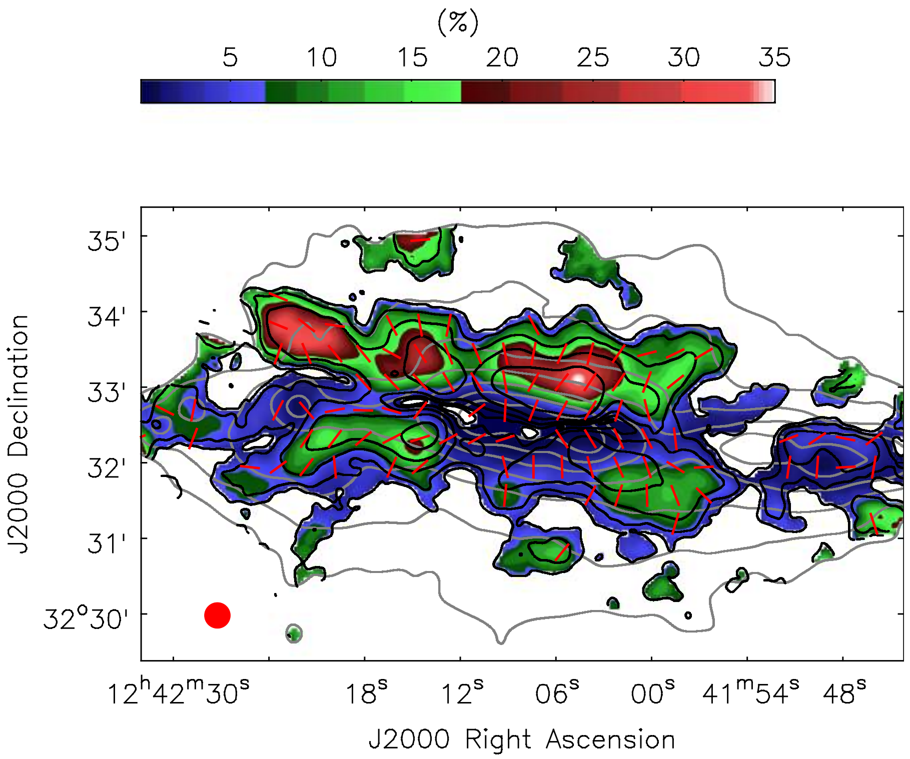

FIGURE 6.4— Degree of polarization at C-band with intrinsic magnetic field vectors. Values were clipped at 2σ of PI and 3σ of TP. Polarization angles were clipped at 5σ of Stokes Q/U. All data plotted has an angular resolution of 20.″5. Black contours correspond to the C-band (D array) polarized emission: 8 μJy/beam $\cdot\,(2,4,8,16,32)$. Grey contours corresponds to the C-band total power emission (EVLA + Eff.): 60 μJy/beam $\cdot\,(3,6,12,24,48,96,192,384)$.

7.2) that originate in the eastern end of the central region. The C-band counterpart has a polarization fraction of up to 27%. The polarization observed at C-band at high resolution (fig. 6.2) shows the spur is connected to the total radio emission that coincides with the HII region CM 67. Golla & Hummel (1994) speculate this spur might originate from this HII region, CM 67, but their data did not have enough angular resolution to determine if the features were indeed connected.

There is another spur-like feature in the southeastern quadrant of the galaxy. At C-band it emerges from the eastern side of the central region, extends towards the east and then bends southeast. It has an average degree of polarization of about 12% at C-band. At high resolution (see fig. 6.2), there is no clear connection with the HII region CM 67, this spur appears visible only 21″ southeast of the eastern peak of the triple radio source. It has a counterpart clearly observable at λ3.6 cm (see fig. 7.2), which

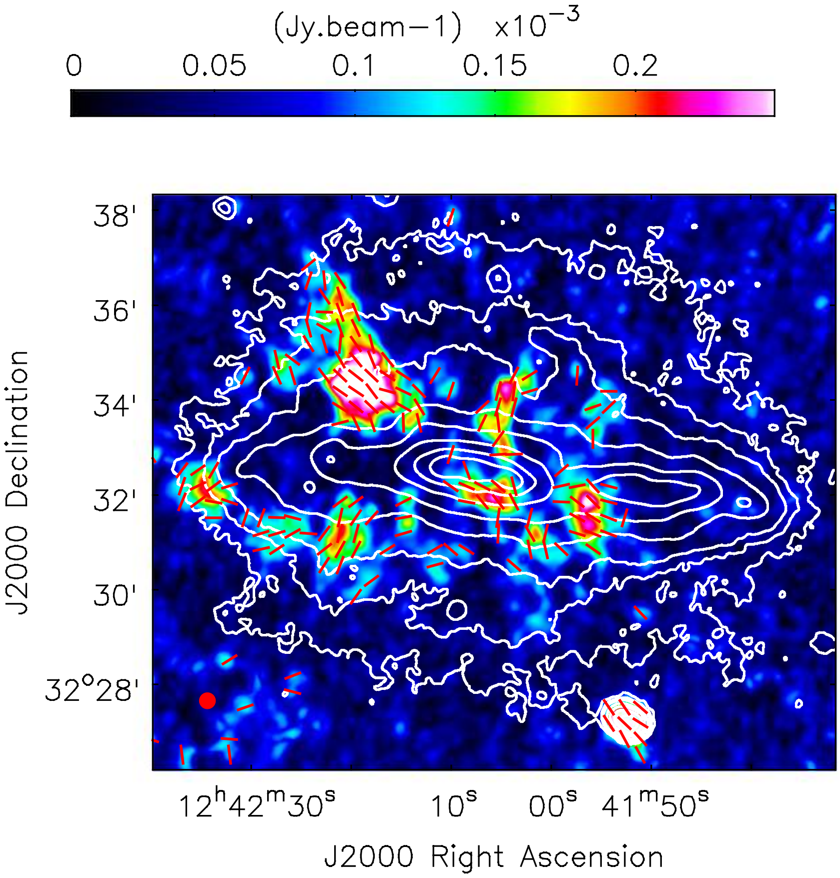

FIGURE 6.5— Polarized emission of NGC 4631 at L-band (C&D array) with intrinsic magnetic field vectors obtained with RM-synthesis. Polarization angles were clipped at 5σ of Stokes Q/U. Contours correspond to the L-band total power emission (EVLA + Eff.). All data plotted has an angular resolution of 20.″5. Contour levels are given by 70 μJy/beam · $(3,6,10,24,48,96,192,384)$.

also extends to the east and then bends southeast. Figure 6.3 indicates this spur might extend at L-band farther out into the southeastern halo, down to a declination of about $\delta_{2000} = 32°30'$ with a polarization degree of up to 21%. It appears to be connected to the SE-radio spur (refer to section 4.1) observed in total power in figures 6.3 and 6.5.

We would like to emphasize a spur-like peculiarity in the C-band and λ3.6 cm (fig. 7.2) polarized emission located in the northeastern quadrant of the galaxy. It is also anchored in the eastern part of the central area of the galaxy and extends to the northeast. It has a polarization fraction of up to 33% at C-band (at 20.″5). The L-band polarized emission displays potential structure as an extension of this spur at

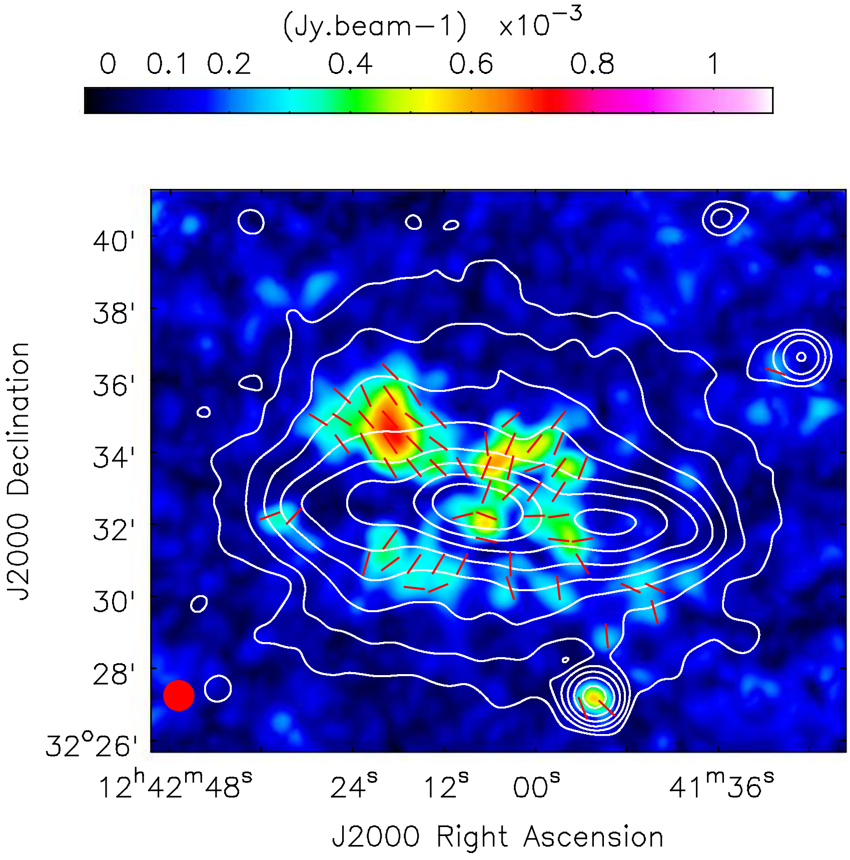

FIGURE 6.6— Polarized emission of NGC 4631 at L-band (D array) with intrinsic magnetic field vectors obtained with RM-synthesis. Polarization angles were clipped at 5σ of Stokes Q/U. Contours correspond to the L-band total power emission (EVLA + Eff.). All data plotted has an angular resolution of $51''$. Contour levels are given by 190 μJy/beam $\cdot\,(3,6,12,24,48,96,192,384)$.

$\alpha_{2000} = 12^h42^m27^s$; $\delta_{2000} = 32^\circ34'30''$ (see fig. 6.3) having a polarization degree of up to 44% (fig. 6.7).

The intrinsic magnetic field orientation in the plane of the sky derived with the C-band data is shown as red vectors in figures 6.2, 6.3 and 6.4. The intrinsic magnetic field vectors derived with the L-band data are presented in figures 6.5, 6.6, 6.7 and 6.8. The polarization angles were corrected for Faraday rotation with the Faraday depths presented in the following section. At both wavebands, we can distinguish that the overall magnetic field structure in the halo is X-shaped in NGC 4631. At L-band it is better visible at lower resolution (fig. 6.6). In addition, at C-band the magnetic field in the halo is also characterized by strong vertical components above and below

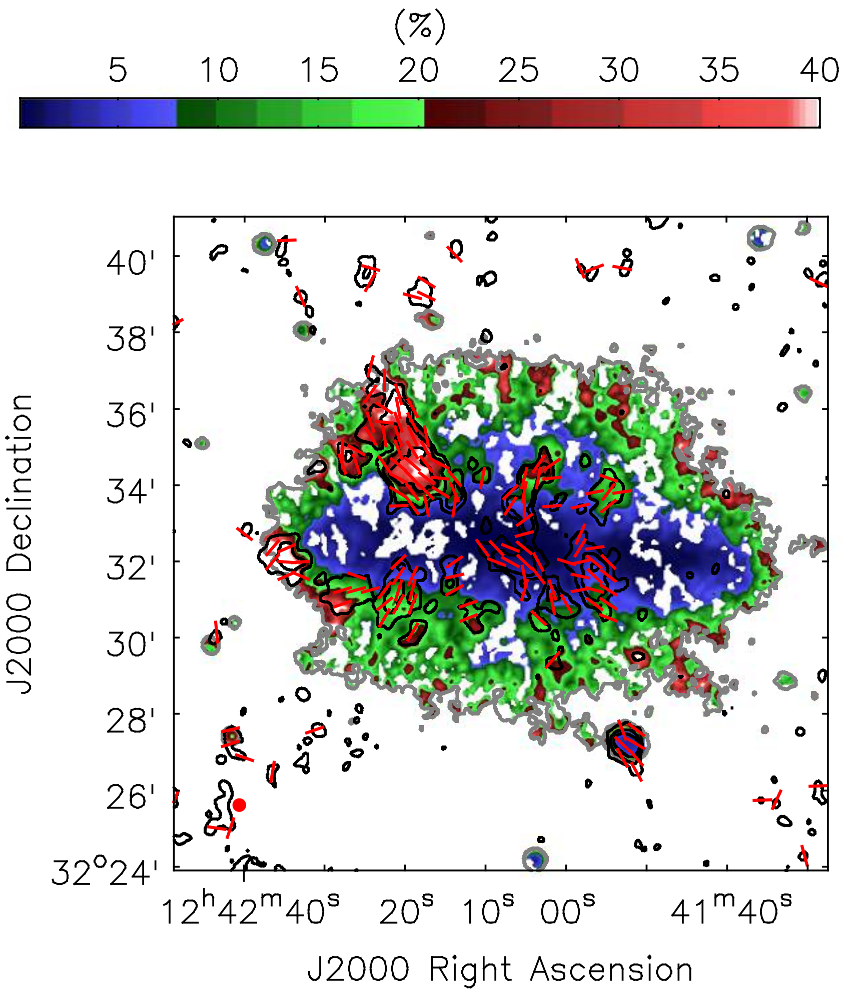

FIGURE 6.7— Degree of polarization at L-band with intrinsic magnetic field vectors. Values were clipped at 2σ of PI and 3σ of TP. Polarization angles were clipped at 5σ of Stokes Q/U. All data plotted has an angular resolution of 20.5″. Black contours correspond to the L-band (C&D array) polarized emission: 35 μJy/beam$\cdot(3, 4.5, 7)$. Grey contour corresponds to the L-band total power emission (EVLA + Eff.): 70 μJy/beam$\cdot(3)$.

the central region of the galaxy which are almost perpendicular to the major axis of NGC 4631. The vertical components above the central area of the galaxy had already been observed in NGC 4631 (Golla & Hummel 1994), but the vertical components below the major axis had never been seen at high resolution. Thanks to the higher sensitivity of our observations and to the fact that we were able to apply RM-synthesis with our wide bandwidth data this has now been detected.

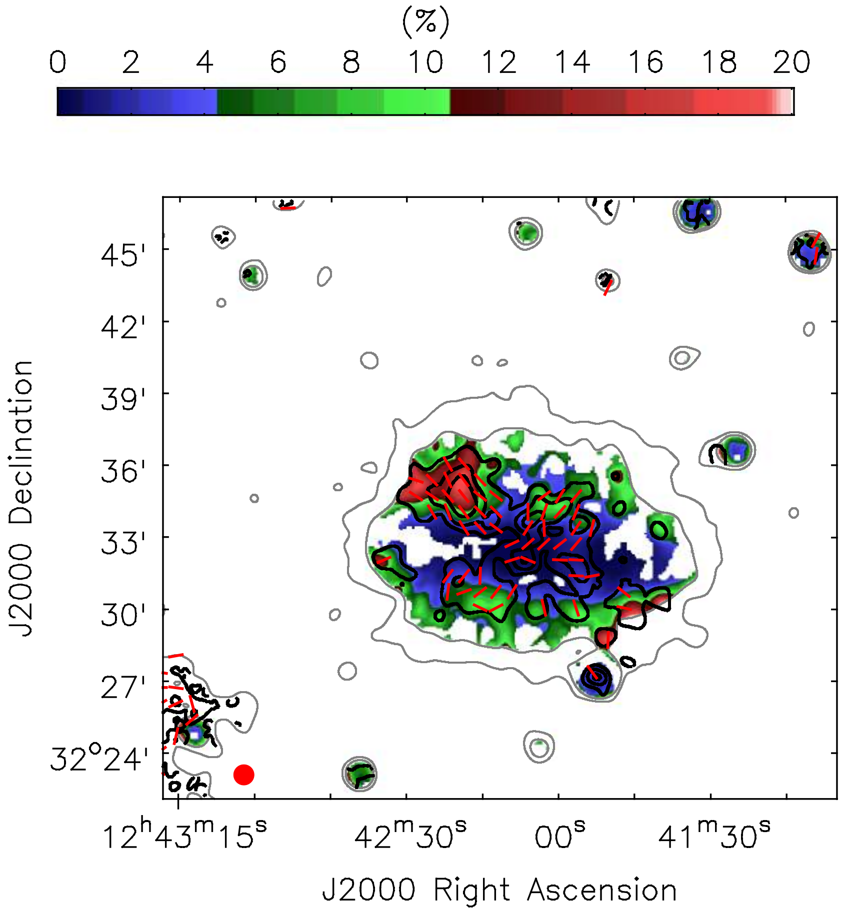

FIGURE 6.8— Degree of polarization at L-band with intrinsic magnetic field vectors. Values were clipped at 2σ of PI and 6σ of TP. Polarization angles were clipped at 5σ of Stokes Q/U. All data plotted has an angular resolution of $51''$. Black contours correspond to the L-band (D array) polarized emission: $60\ \mu\mathrm{Jy/beam} \cdot (3,6,9)$. Grey contours corresponds to the L-band total power emission (EVLA + Eff.): $190\ \mu\mathrm{Jy/beam} \cdot (3,6)$.

Along the central part of the disk observed at L-band, there are several magnetic field vectors parallel to the midplane of the galaxy. The orientation of the vectors support the idea that the magnetic field along the central region of the galaxy is parallel to the major axis of NGC 4631. This however, is probably caused by a layer of emission observed in the front side of the disk, since the central region is too thick for L-band polarized emission coming from the nuclear region of the galaxy to be observed. We will discuss this further in section 6.3.2.

At C-band, the magnetic field in the disk is only clearly seen in the eastern side of the galaxy, it is plane-parallel to the major axis of the galaxy. Figure 6.4 demonstrates the disk is highly depolarized at C-band. In the central region of the galaxy we find a average degree of polarization of $\sim 1.3\%$, however, the eastern and western sides of the disk have a higher polarization fraction of about 5.8% and 2.4%, respectively. The RM-synthesis algorithm may be able to reduce the bandwidth depolarization and the differential Faraday rotation depolarization, but it cannot account for Faraday dispersion or beam depolarization. Chapter 7 has been dedicated to discussing the disk magnetic field orientation in NGC 4631 with $\lambda 3.6$ cm data. As we will demonstrate in section 6.3.2, at this wavelength observations are less affected by Faraday depolarization effects and therefore, the magnetic field along the midplane is more clearly visible.

The orientation of the magnetic field of the PI spur in the southeastern halo mentioned above (see fig. 6.5) seems to be aligned with the HI spur 2 (see fig. 4.5). Since this is also parallel to the X-shaped halo field, it is difficult to distinguish which part of the halo magnetic field might be related to the HI spur 2. Therefore, we cannot determine whether these features are actually related and if the magnetic field lines are coupled to the outflowing gas.

6.2.2 Distribution of the Faraday depths

The Faraday depths obtained at C-band are shown in figure 6.9 at a resolution of $7''$ and in figure 6.10 at $20\overset{''}{.}5$. Overall, the Faraday depths at C-band obtained with RM-synthesis agree with those estimated in section 7.2.1 by applying the classical approach of deriving RM values with the observed polarization angles at $\lambda 3.6$ and 6.2 cm. In addition, the Faraday depths obtained with the L-band data are shown in figure 6.11 ($20\overset{''}{.}5$ FWHM) and in figure 6.12 ($51''$ FWHM). Results are well in agreement with those obtained by Heald et al. (2009) with Westerbork observations. The Galactic foreground component is negligible in the direction of the sky in which NGC 4631 is located, Heald et al. (2009) obtain $\mathrm{RM_{fg}} = -4 \pm 3$ rad $\cdot$ m^{-2} and Oppermann et al. (2012) estimate $\mathrm{RM_{fg}} = -0.3 \pm 2.7$ rad $\cdot$ m^{-2}.

The Faraday depths at C-band range between -400 and 400 rad $\cdot$ m^{-2}. At L-band they range between -40 and 40 rad $\cdot$ m^{-2}, since observations at this frequency band are limited by the maximum observable scale. Missing spacings in Faraday space can create artifacts affecting the detected Faraday depths as demonstrated by Schnitzeler et al. (2015). In addition, we are probably probing different Faraday screens along the LOS at C-band and at L-band, we will discuss this further in section 6.3.2. At C-band (L-band) the mean error in the Faraday depth is about 80 rad $\cdot$ m^{-2} (9 rad $\cdot$ m^{-2}), however, errors decrease to 30 rad $\cdot$ m^{-2} (6 rad $\cdot$ m^{-2}) in areas of high polarized intensity.

At both frequency bands the Faraday depths observed at low resolution do not

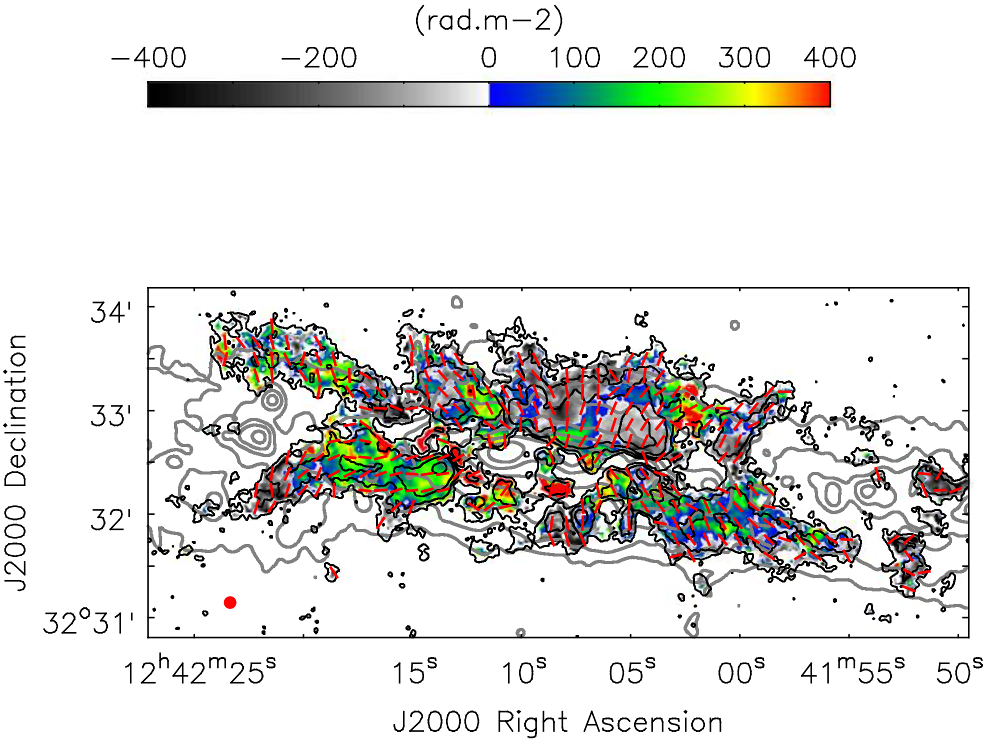

FIGURE 6.9— Faraday depths obtained with the C-band (C+D array) data with intrinsic magnetic field vectors. Faraday depths and polarization angles were clipped at 5σ of Stokes Q/U. All data plotted has an angular resolution of 7$''$. Black contours correspond to the C-band polarized emission: 3.5 μJy/beam $\cdot$ (2,4,8,16,32,64). Grey contours corresponds to the C-band total power emission (EVLA + Eff.): 19 μJy/beam $\cdot$ (3,6,12,24,48,96,192,384).

show strong variations of field direction on scales of several hundred parsecs, implying there is a regular magnetic field in the halo of NGC 4631. As the Faraday depth distribution in the disk shows no type of symmetry with respect to the major or minor axis of the galaxy, we cannot associate it with a specific parity of the presumably dynamo generated magnetic field in the disk.

In figure 6.13 we present a profile of the Faraday depths at C-band in the northern disk-halo interface of the galaxy extending from about $\alpha_{2000} = 12^h42^m02^s$ to $\alpha_{2000} = 12^h42^m17.6^s$. The profile shows that the Faraday depths vary smoothly from $\sim$ 200 rad $\cdot$ m^{-2} to about -150 rad $\cdot$ m^{-2} in a quasi-periodic pattern. The Faraday depth distribution in the northern halo of the galaxy indicates that the magnetic field along the LOS has a systematic change in direction on scales of about 1.9 kpc (half wavelength). This might be due to filaments of emission ejected from star forming regions in the disk which are coupled to the magnetic field. If this were the case,

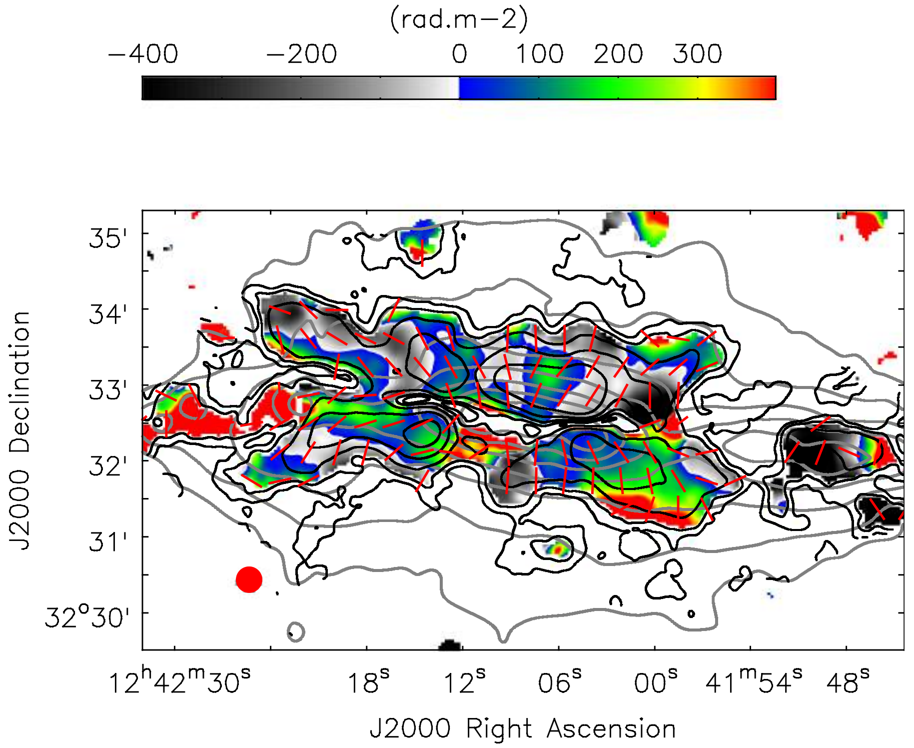

FIGURE 6.10— Faraday depths obtained with the C-band (D array) data with intrinsic magnetic field vectors. Faraday depths and polarization angles were clipped at 5σ of Stokes Q/U. All data plotted has an angular resolution of 20.″5. Black contours correspond to the C-band polarized emission: 8 μJy/beam $\cdot$ (2, 4, 8, 16, 32). Grey contours corresponds to the C-band total power emission (EVLA + Eff.): 60 μJy/beam $\cdot$ (3, 6, 12, 24, 48, 96, 192, 384).

however, we would expect the filaments to have random Faraday depth signs and in consequence, we would not observe a quasi-periodic pattern in the Faraday depth profile. Another possible explanation is that these features may be attributed to magnetic loops extending out of the sky plane. Why this phenomenon occurs only in the northern halo of the galaxy remains unclear. The first indication of a Parker loop in a nearby spiral galaxy was found by Beck et al. (1989) in M 31 on scales of 2.25 kpc (half wavelength). Later on, Beck (2015) found indications of Parker loops in IC 342 on scales of about 2 kpc. Detail modeling of the magnetic field in NGC 4631, taking into account the polarization properties of the galaxy, may give more insight on the origin of these features.

At 20.″5 resolution the background radio galaxy to the southwest of NGC 4631 (see section 4.4 for details) appears as a point-source with an average degree of polarization

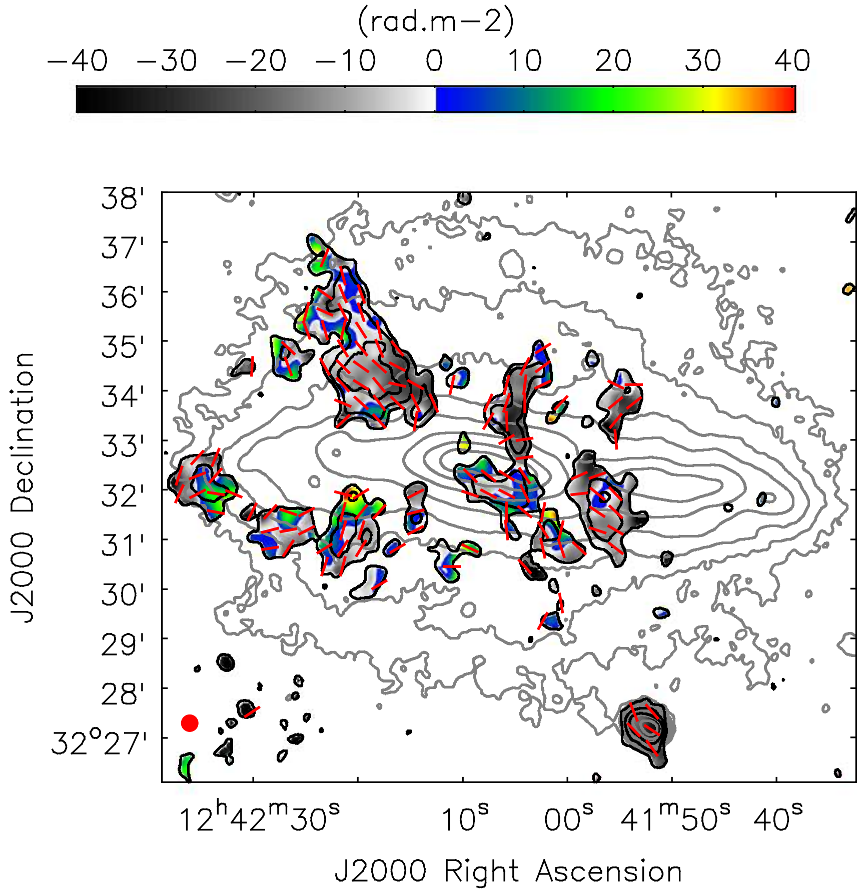

FIGURE 6.11— Faraday depths obtained with the L-band (C&D array) data with intrinsic magnetic field vectors. Faraday depths and polarization angles were clipped at 5σ of Stokes Q/U. All data plotted has an angular resolution of 20$''$.5. Black contours correspond to the L-band polarized emission: 35 μJy/beam $\cdot$ (3, 4.5, 7). Grey contours corresponds to the L-band total power emission (EVLA + Eff.): 70 μJy/beam $\cdot$ (3, 6, 10, 24, 48, 96, 192, 384).

of 6% at L-band. The Faraday depths are rather uniform over the two lobes with an average value of -21 ± 13 rad $\cdot$ m^{-2}. The intrinsic magnetic field is orientated parallel to the radio galaxy's main axis. Within the uncertainties, the observed Faraday depths indicate that they might be of Galactic origin, although the background radio galaxy is so closely located to NGC 4631 that contribution from the halo of NGC 4631 cannot be excluded.

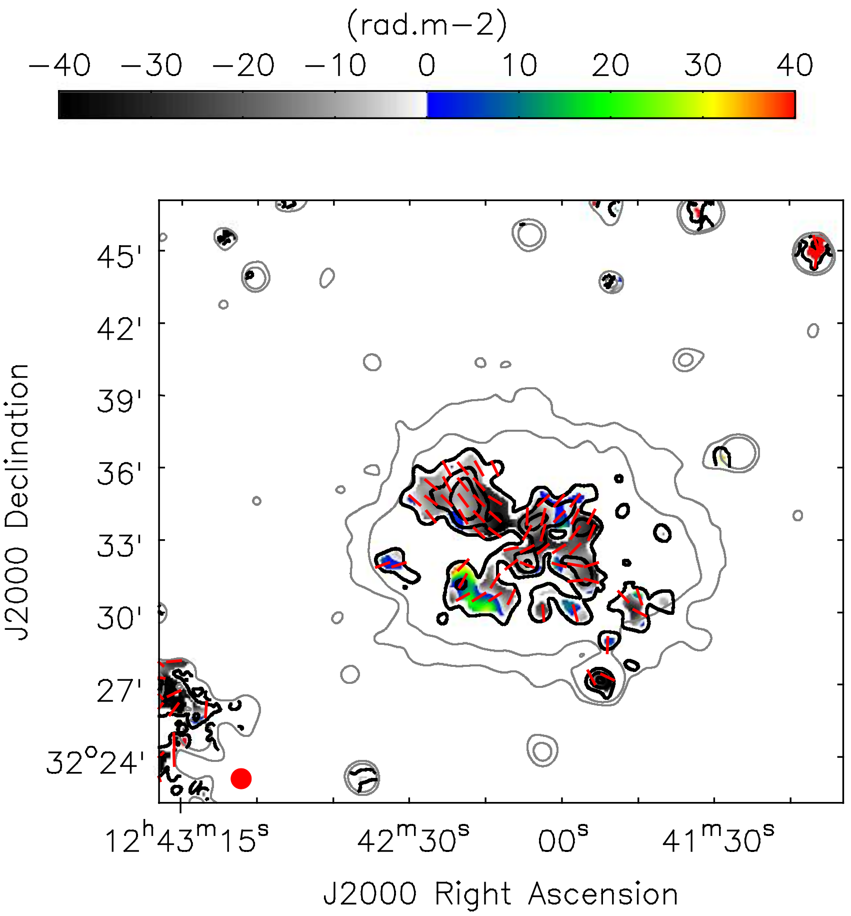

FIGURE 6.12— Faraday depths obtained with the L-band (D array) data with intrinsic magnetic field vectors. Faraday depths and polarization angles were clipped at 5σ of Stokes Q/U. All data plotted has an angular resolution of $51''$. Black contours correspond to the L-band polarized emission: 60 μJy/beam $\cdot\,(3,6,9)$. Grey contours corresponds to the L-band total power emission (EVLA + Eff.): 190 μJy/beam $\cdot\,(3,6)$.

6.2.3 Observed Faraday depolarization distribution

The observed Faraday depolarization (wavelength-dependent) in NGC 4631 was determined by taking into account the polarization at both frequency bands and the nonthermal spectral index as follows:

$$\mathrm{DP}_{\mathbf{obs}}(\mathrm{L},\mathrm{C}) = \frac{\mathrm{PI}_{\mathrm{Lband}}}{\mathrm{PI}_{\mathrm{Cband}}} \cdot \left(\frac{\nu_{\mathrm{Cband}}}{\nu_{\mathrm{Lband}}}\right)^{\alpha_{\mathrm{nth}}} \tag{6.1}$$

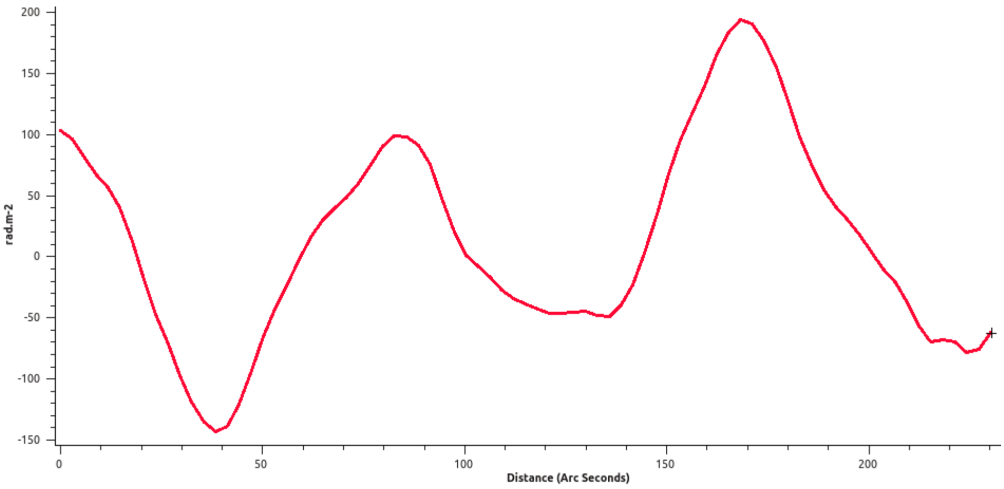

FIGURE 6.13— Profile of the Faraday depth distribution observed at C-band in the northern area of the disk-halo interface. The magnetic field of NGC 4631 has a systematic change in direction on scales of about 1.9 kpc. The mean error in the Faraday depth values is 36 $\text{rad} \cdot \text{m}^{-2}$.

The observed Faraday depolarization at a resolution of $20.5''$ is presented in figure 6.14. It was determined from data truncated at 2σ of the polarized intensity maps. Values range between 0 and 1, $\text{DP} = 0$ indicates complete depolarization while $\text{DP} = 1$ means no depolarization. The polarized intensity maps at both frequency bands have the same angular resolution. Therefore, the beam depolarization affects both maps similarly and cancels out. Bandwidth depolarization can be minimized by reducing the channel width of the utilized receiver and by implementing the RM-synthesis technique (section 1.2.2). If we simulate bandwidth depolarization for our frequency setups, by comparing the polarized intensity we recover after running RM-synthesis to the emitted polarized intensity if we increase the Faraday depth of the simulated source, we find that bandwidth depolarization starts to play a role only for sources with $|\text{RM}| > 10^4$ $\text{rad} \cdot \text{m}^{-2}$ at both C-band and L-band (see also fig. 4 in Schnitzeler & Lee 2015). Therefore, we can assume that bandwidth depolarization is negligible compared to the Faraday depolarization effects.

As one would expect, the depolarization increases towards the midplane of the galaxy. The thermal emission of NGC 4631 (fig. 5.12) indicates the thermal electrons are concentrated in the disk of the galaxy in the star forming regions. Since star formation causes the magnetic field to become more turbulent, the interstellar medium in the disk may be considerably more turbulent producing internal Faraday dispersion. The long LOS through the disk may also cause depolarization by differential Faraday rotation and Faraday dispersion within NGC 4631. The eastern half of the disk-halo interface of the galaxy seems to be more depolarized than the western half, this might

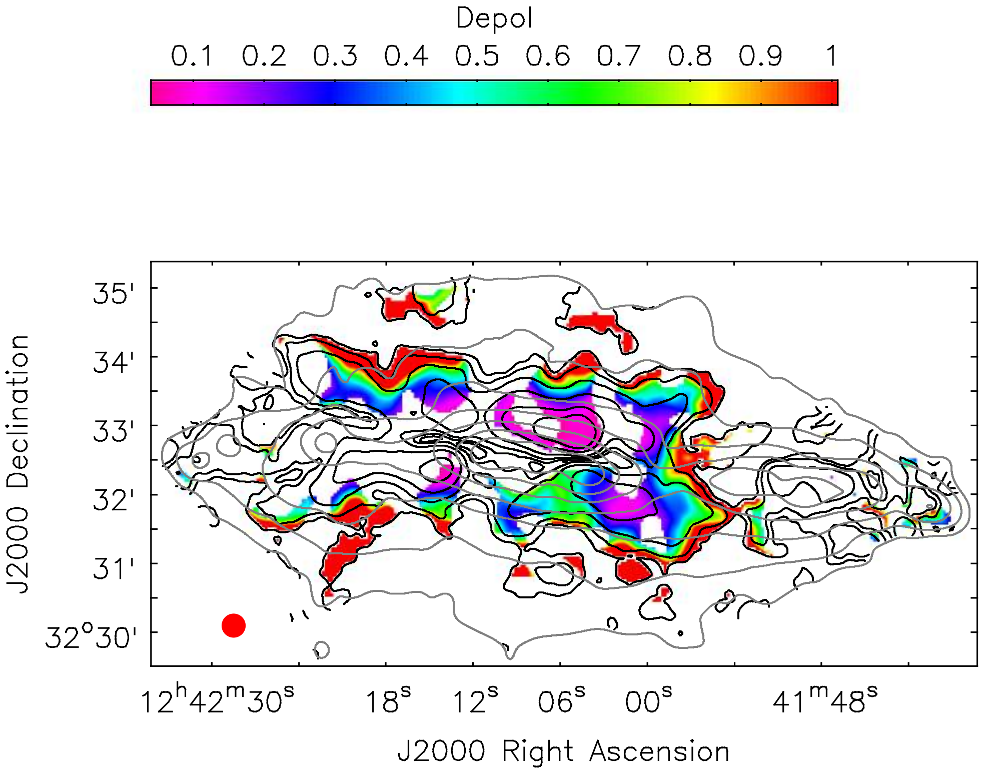

FIGURE 6.14— Depolarization distribution in NGC 4631. Values were clipped at 2σ of PI (at both frequencies). All data plotted has an angular resolution of $20.5''$. Black contours correspond to the polarization detected at C-band (D array): 8 μJy/beam $\cdot\,(2,4,8,16,32,64)$. Grey contours correspond to the C-band total power emission (EVLA + Eff.): 60 μJy/beam $\cdot\,(3,6,12,24,48,96,192,384)$.

be related to the fact that the eastern part of the disk-halo interface of NGC 4631 has a higher thermal fraction than the western region (see figure 5.8), which implies that depolarization due to internal Faraday dispersion may be stronger in this side of the galaxy.

6.2.4 Magnetic field strengths

With the synchrotron intensity and the nonthermal spectral index we can now estimate the strength of the total magnetic field in NGC 4631. Assuming equipartition between the total energy densities of cosmic rays and that of the magnetic field, the magnetic field strength can be derived using the revised equipartition formula described in Beck & Krause (2005):

$$B_{eq} = \left(\frac{4\pi(2|\alpha_{nth}|+1)(K_0+1)\, I_\nu\, E_p^{1-2|\alpha_{nth}|} (\nu/2c_1)^{|\alpha_{nth}|}}{(2|\alpha_{nth}|-1) c_2(|\alpha_{nth}|)\, L\, c_4(i)} \right)^{1/(|\alpha_{nth}|+3)} \tag{6.2}$$

where K_0 is the ratio of the number densities of relativistic protons and electrons, I_ν is the nonthermal intensity at frequency ν, E_p is the rest mass energy of protons, L is the pathlength through the synchrotron emitting region and $|\alpha_{nth}|$ is the absolute value of the nonthermal spectral index. The constants c_1, c_2, c_3 and $c_4(i)$ (depends on the inclination of the magnetic field) are defined in Beck & Krause (2005).

We assume a ratio of proton-to-electron number density of $\mathrm{K}_0 \simeq 100$. The pathlength was modeled as a combination of two oblate spheroidals, one corresponding to the disk since most of the emission is concentrated in this region, and another spheroidal corresponding to the halo. The x-axes coincides with the major axis of the galaxy, the y-axes with the minor axis and the z-axes represents the pathlength through NGC 4631. Since the radio emission of NGC 4631 extends up to 15 kpc in radius along the major axis, we assume the maximum pathlength through the galaxy to be twice this value. In the central area of the galaxy we estimate the largest pathlength of 30 kpc and it decreases to about 7 kpc towards the outer edges of the disk. In the halo we have the largest pathlength of ~ 22 kpc close to the central region of the galaxy and it decreases to about 4 kpc towards the outer edges of the halo. The magnetic field, however, shows weak dependence on the pathlength $B \propto L^{[-1/(|\alpha_{nth}|+3)]}$. Therefore, our assumptions concerning the pathlength through NGC 4631 will not have a large impact on the total magnetic field strength but since we are dealing with an edge-on galaxy it would be incorrect to assume a constant pathlength throughout the source.

Equation 6.2 diverges for $|\alpha_{\mathrm{nth}}| \leq 0.5$, but this does not affect our results since our nonthermal spectral indices range between $|\alpha_{\mathrm{nth}}| = 0.7 - 1.5$ (see section 6.1.2). Steep spectral index values of $|\alpha_{\mathrm{nth}}| > 1$ arise due to dominant energy losses of cosmic ray electrons (CREs). In these regions of steep spectral index, the energy spectral index between the CREs and cosmic ray protons changes, hence, the ratio between the number densities of the relativistic protons and electrons is no longer constant. We have therefore set $|\alpha_{\mathrm{nth}}| = 1$ wherever $|\alpha_{\mathrm{nth}}| > 1$.

The strength of the total magnetic field in NGC 4631 is shown in figure 6.15. The errors are at most 50% and decrease with increasing intensity. The errors in the total magnetic field strengths were estimated using Monte-Carlo method by taking into account the uncertainties in the nonthermal intensity values and the error in the nonthermal spectral indices as described in Basu & Roy (2013). We used 10^4 random flux intensity samples assuming a Gaussian distribution of error at 1.57 and 5.99 GHz. These values were then used to determine the distribution of B_{eq}. The error related to the adopted pathlength was not taken into account, however, as mentioned above the pathlength does not introduce significant errors compared to the other uncertainties. The mean strength in the disk is $\langle B_{eq} \rangle \approx 9 \pm 0.7\ \mu G$, however in the central area of the galaxy the field strength goes up to $B_{eq} \approx 12 \pm 0.5\ \mu G$. In the halo the mean field strength is slightly lower $\langle B_{eq} \rangle \approx 7 \pm 1.5\ \mu G$. These values are in accordance with those estimated by Mora & Krause (2013) with Effelsberg data at λ3.6 cm assuming a constant nonthermal spectral index. Furthermore, the mean strength of the total field in the central region of the disk, $\langle B_{eq} \rangle \approx 10 \pm 0.5\ \mu G$ is comparable to the mean strength of the perpendicular field above and below the galactic center, $\langle B_{eq} \rangle \approx 9 \pm 1\ \mu G$.

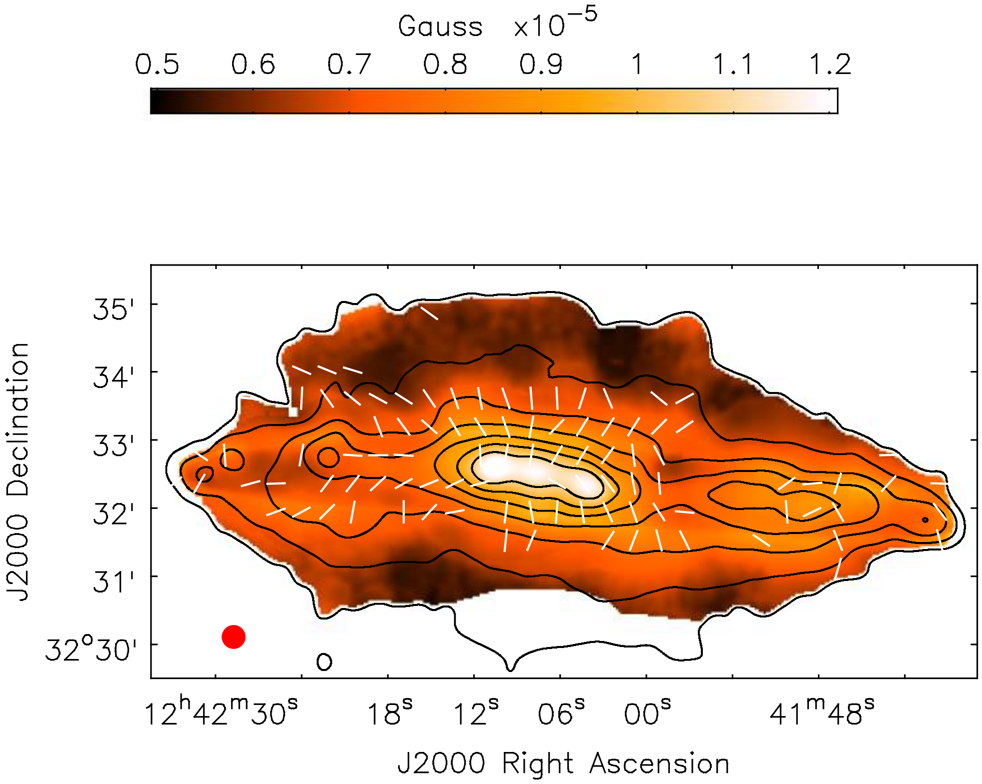

FIGURE 6.15— Strength of the total magnetic field in NGC 4631 with intrinsic magnetic field vectors observed at C-band. Polarization angles were clipped at 5σ of Stokes Q/U. Angular resolution is 20.5″. Contours correspond to the C-band total power emission (EVLA + Eff.): 60 μJy/beam $\cdot$ (3, 6, 12, 24, 48, 96, 192, 384).

The edge-on galaxy NGC 5775 has a total magnetic field strength in its disk of $11 \pm 3\ \mu G$ and $6 \pm 2\ \mu G$ in its halo (Soida et al. 2011). While NGC 253 has a total magnetic field strength in its disk of $15 \pm 1.5\ \mu G$ and $4.4 \pm 0.5\ \mu G$ in the halo (Heesen et al. 2009b). The mean magnetic field in the disk of NGC 4631 is comparable to that in NGC 5775, but is not as strong at the field strength in NGC 253 which is known to have very strong star formation activity in its disk. However, the strength of the mean magnetic field in the halo of NGC 4631 seems to be higher than in the other galaxies.

The strength of the ordered and turbulent magnetic field component in the plane of the sky was estimated taking into account $B_{eq,\perp}^{1+|\alpha_{nth}|} = B_{o,\perp}^{1+|\alpha_{nth}|} + B_{t,\perp}^{1+|\alpha_{nth}|}$, and in addition considering the degree of order of the field in case of equipartition Beck (2007):

$$q = \frac{B_{o,\perp}}{B_{t,\perp}} \simeq \sqrt{\frac{p_{nth}/p_0}{2(1-p_{nth}/p_0)}} \tag{6.3}$$

The parameter p_{nth} is the fractional polarization of the nonthermal emission and $p_0 = (3+3|\alpha_{nth}|)/(5+3|\alpha_{nth}|)$ is the intrinsic degree of polarization. The parameter q was determined with the C-band data of NGC 4631. The degree of field order is below 1 over most of the galaxy. Highest values of 0.7 coincide with the polarized intensity peaks observed at C-band. For the Milky Way an average value of $q \simeq 0.6$ has been determined from starlight polarization and from synchrotron data (Beck 2001). For NGC 6946, Beck (2007) determined that q lies between 0-1, having the highest values in the outer regions of the magnetic arms.

The strength of the ordered field in the plane of the sky is presented in figure 6.16. The values obtained for the strength of the ordered field perpendicular to the LOS represent lower limits since they are derived from the observed polarization which is affected by depolarization effects such as differential Faraday rotation, Faraday dispersion and beam depolarization. The mean strength of the ordered magnetic field is about $\langle \mathrm{B_{o,\perp}} \rangle \approx 1\ \mu$G in the disk, and $\langle \mathrm{B_{o,\perp}} \rangle \approx 2\ \mu$G in the halo. It increases with increasing polarized intensity, therefore the ordered field in the sky plane is stronger in the halo than in the disk. In figure 6.17 the strength of the turbulent component of the magnetic field perpendicular to the LOS is depicted. The turbulent field is strongest along the disk of NGC 4631 and specially in the central region where it reaches a maximum of $\mathrm{B_{t,\perp}} \approx 10\ \mu$G. This may be one of the reasons why the degree of depolarization is so high in this region.

6.3 Discussion

6.3.1 Cosmic ray electron energy losses

As has already been pointed out, the CREs in the ISM are produced in supernovae explosions and are subject radiation loss mechanisms through inverse-Compton scattering (IC), synchrotron emission, ionization and bremsstrahlung processes. Synchrotron and IC losses steepen the spectrum, ionization losses flatten the spectrum towards lower radio frequencies while bremsstrahlung losses do not considerably change the spectrum. In order to estimate the contribution of the different loss

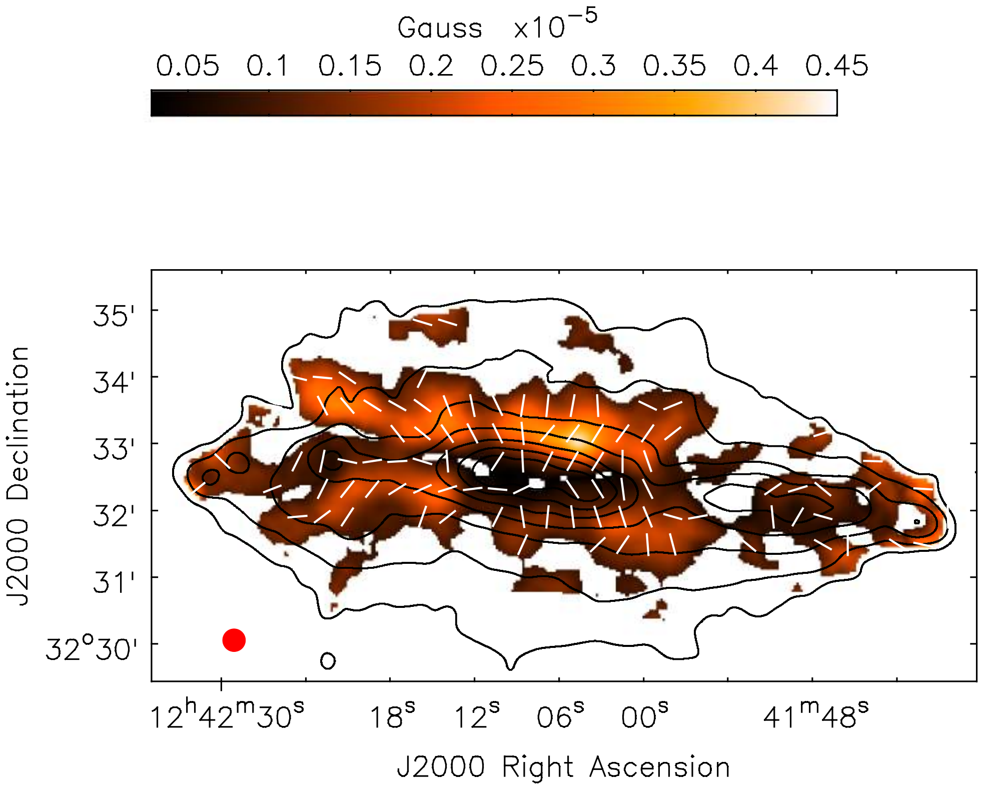

FIGURE 6.16— Strength of the ordered magnetic field in the sky plane with intrinsic magnetic field vectors observed at C-band. Values have been clipped at 2σ of the C-band polarized intensity. Polarization angles were clipped at 5σ of Stokes Q/U. All data plotted has an angular resolution of $20.5''$. Contours correspond to the C-band total power emission (EVLA + Eff.): 60 μJy/beam $\cdot$ $(3, 6, 12, 24, 48, 96, 192, 384)$.

processes in NGC 4631, the timescale of each of the mechanisms was derived separately for the central area of the galaxy, the disk (excluding the central region) and the halo of NGC 4631.

The energy loss of CREs by synchrotron radiation is proportional to the strength of the total magnetic field in the plane of the sky and to the energy of the electrons: $dE/dt \propto (B_{\perp}^2) \cdot E^2$. The energy of CREs gyrating in a magnetic field of strength B and emitting at a radio frequency ν can be estimated according to the equation (Longair 2011):

$$\left(\frac{\mathrm{E}}{\mathrm{GeV}}\right) = 7.9 \left(\frac{\nu}{\mathrm{GHz}}\right)^{1/2} \left(\frac{B_{\perp}}{\mu\mathrm{G}}\right)^{-1/2} \tag{6.4}$$

where $B_{\perp}$ is the strength of the total magnetic field in the sky plane. The synchrotron

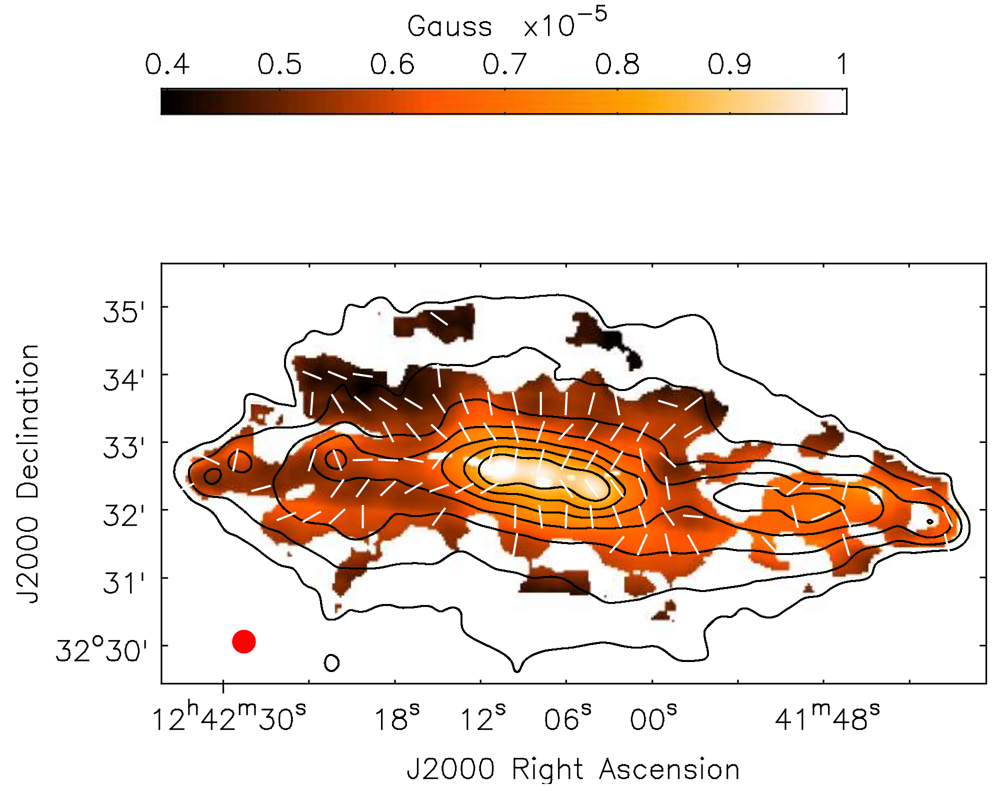

FIGURE 6.17— Strength of the turbulent magnetic field in the sky plane with intrinsic magnetic field vectors observed at C-band. Values have been clipped at 2σ of the C-band polarized intensity. Polarization angles were clipped at 5σ of Stokes Q/U. All data plotted has an angular resolution of 20.5″. Contours correspond to the C-band total power emission (EVLA + Eff.): 60 μJy/beam $\cdot$ $(3,6,12,24,48,96,192,384)$.

timescale can be estimated from the energy of CREs as (Longair 2011):

$$\left(\frac{\tau_{\rm syn}}{\rm yrs}\right) = 8.35 \cdot 10^{9} \left(\frac{E}{\rm GeV}\right)^{-1} \left(\frac{B_{\perp}}{\mu \rm G}\right)^{-2} \tag{6.5}$$

The energy loss of CREs due to inverse-Compton scattering is also proportional to the energy of the electrons and in addition, to the energy density of the radiation field: $dE/dt \propto U \cdot E^2$. The lifetime for inverse-Compton losses attributed to the scattering of CREs by the radiation field of NGC 4631 with energy density U_{rad} and by the cosmic microwave background with energy density $U_{CMB} = 4.2 \cdot 10^{-13}$erg cm^{-3} (at redshift

$z = 0$) is given by (Longair 2011):

$$\left(\frac{\tau_{\rm IC}}{\rm yrs}\right) = 4.5 \cdot 10^8 \left(\frac{E}{\rm GeV}\right)^{-1} \left(\frac{\rm U_{rad} + U_{CMB}}{10^{-12}\rm erg \cdot cm^{-3}}\right)^{-1} \tag{6.6}$$

For electrons with energy of a few GeV, most of the IC losses arise from interactions with IR and optical photons. The energy density of the radiation field within the three different regions taken into account in NGC 4631 was estimated using the following approximation from Murphy et al. (2008):

$$\rm U_{rad} \approx \frac{2\pi}{c} I_{bol} \gtrsim \frac{L_{TIR}}{2cA_{TIR}} \left(1 + \sqrt{\frac{3.8 \cdot 10^{42}}{L_{TIR}}}\right) \tag{6.7}$$

where I_{bol} is the bolometric surface brightness of the galaxy, c is the speed of light and A_{TIR} is the area of the region emitting the total infrared luminosity L_{TIR}. The factor $(1 + \sqrt{3.8 \cdot 10^{42}/L_{TIR}})$ accounts for the correction from nonabsorved UV emission (Bell 2003). The total infrared luminosity was estimated considering the following calibration given in Dale & Helou (2002):

$$\rm L_{TIR} = 1.559 \cdot \nu L_\nu[24\mu m] + 0.7686 \cdot \nu L_\nu[70\mu m] + 1.347 \cdot \nu L_\nu[160\mu m] \tag{6.8}$$

The infrared luminosities at 24, 70 and 160 μm in the regions considered within NGC 4631 were obtained from the maps presented in section 5.1. To estimate the area of the emitting regions, we assumed the distribution to have an spheroidal shape of a specific size depending on the region of interest. This resulted in an energy density of $\rm U_{rad,c} = 2.2 \cdot 10^{-12}$ erg $\cdot$ cm^{-3} for the central region, $\rm U_{rad,d} = 1.5 \cdot 10^{-14}$ erg $\cdot$ cm^{-3} for the disk and $\rm U_{rad,h} = 3.5 \cdot 10^{-14}$ erg $\cdot$ cm^{-3} for the halo.

Ionization losses occur when a cosmic ray collides with a neutral particle, imparting its energy to the neutral particle and therefore ionizing it. According to Murphy (2009), the timescale for ionization (τ_{ion}) and for bremsstrahlung (τ_{brem}) losses can be estimated from the average number density of neutral gas (atomic + molecular), $\langle n \rangle$:

$$\left(\frac{\tau_{\rm ion}}{\rm yrs}\right) = 4.1 \cdot 10^9 \left(\frac{\langle n \rangle}{\rm cm^{-3}}\right)^{-1} \left(\frac{E}{\rm GeV}\right) \left(3\ln\left(\frac{E}{\rm GeV}\right) + 42.5\right)^{-1} \tag{6.9}$$

$$\left(\frac{\tau_{\rm brem}}{\rm yrs}\right) = 3.96 \cdot 10^7 \left(\frac{\langle n \rangle}{\rm cm^{-3}}\right)^{-1} \tag{6.10}$$

To determine the average number density of neutral gas in the central region we take into account an HI density of 0.74 cm^{-3} modeled by Rand (1994) for the central area of NGC 4631. Since Irwin et al. (2011) estimated the H_I and H_2 masses are roughly equal in the central molecular ring of NGC 4631, we assume H_2 has half the density of H_I. The number density for the central region is then approximated to $\langle n_c \rangle \approx 1.36 \cdot (0.74 + 0.37)$ cm^{-3}, where the factor 1.36 is to account for the contribution of helium. The number density for the disk was estimated in a similar manner considering an HI density of 0.4 cm^{-3} (Rand 1994) and assuming that H_2 has half the density of H_I following the approximations of Irwin et al. (2011). To derive the number density in the halo we integrated the HI emission (shown in figure 4.5) within the 3σ sensitivity of our radio data and assumed an spheroidal volume.

Results are presented in Table 6.4. In the central area of the galaxy, where we find the strongest total magnetic field strength and highest number density, losses by synchrotron radiation have the lowest timescale. The average nonthermal spectral index in the central region is of $\alpha_{\mathrm{nth,c}} = -0.76 \pm 0.04$, steeper than the typical injection spectrum of -0.5 (see section 6.1.2). Therefore, it is plausible these CREs have lost a large portion of their energy due to synchrotron radiation which steepens the nonthermal spectral index between C-band and L-band. A similar trend is found for the rest of the disk emission.

In the halo, synchrotron radiation is again the dominating energy loss mechanism. The timescale for inverse-Compton losses, on the other hand, is almost a factor of four larger than τ_{syn}. Basu et al. (2015) estimated various CRE energy loss timescales at 5 GHz as a function of neutral gas surface density assuming a Milky Way model for the vertical distribution of the atomic and molecular gas. They find, IC losses are important in galaxies only in low density regions having magnetic field strengths less than $\sim 3.3\ \mu$G. Therefore, in the outer halo of NGC 4631, where neutral gas densities and magnetic field strengths are low, IC losses may play a major role in shaping the radio halo.

In addition, Basu et al. (2015) find that ionization losses are dominant in galaxies in regions of high gas density or at radio frequencies below 0.3 GHz. Since our observations are at much higher frequencies ionization losses are negligible in our case at large spatial scales, in accordance with the values presented in Table 6.4. According to Basu et al. (2015), for ionization losses to dominate over synchrotron losses at higher frequencies (1.4-5 GHz), an extremely high surface gas density of more than 1000 $M_\odot$pc^{-2} are required. Irwin et al. (2011) estimated the H_2 surface mass density in the central area of NGC 4631 peaks at 380 $M_\odot$pc^{-2}. Employing the same approximations described above (H_I and H_2 masses are roughly equal in the central molecular ring according to Irwin et al. 2011), we obtain a maximum neutral gas surface density of 1034 $M_\odot$pc^{-2}. Therefore, ionization losses may still play a role at small spatial scales within the central region of NGC 4631.

Up to now we have not considered energy losses due to adiabatic expansion, which may play an important role in NGC 4631. According to Sukumar & Velusamy (1985), adiabatic losses become more dominant at low frequencies and therefore, the effect of a galactic wind on the measured spectral indices of NGC 4631 can be seen only below a certain radio frequency ν_D, which is the frequency corresponding to the CRE energy for which synchrotron losses are equal to adiabatic losses. With observations at 327, 610 and 1412 MHz, they conclude that ν_D may be equal to ∼600 MHz.

TABLE 6.4— Cooling timescales for CREs due to synchrotron (τ_{syn}), inverse-Compton (τ_{IC}), ionization (τ_{ion}) and bremsstrahlung (τ_{brem}) losses in different regions within NGC 4631 at $\nu = 5.99$ GHz. The strength of the total magnetic field perpendicular to the LOS ($B_{eq,\perp}$) and the energy (E) of the CREs are also included. The emission of the central region was excluded in the values considered for the disk.

Region	**Central Region**	**Disk**	**Halo**
$\mathbf{B_{eq,\perp}}$ **[μG]**	9.4	6.4	5.5
E [GeV]	6.3	7.6	8.2
$\langle$n$\rangle$ [cm^{-3}]	1.5	0.8	0.02
$\tau_{\rm syn}$ [yrs]	$0.15 \cdot 10^8$	$0.27 \cdot 10^8$	$0.33 \cdot 10^8$
$\tau_{\rm IC}$ [yrs]	$0.27 \cdot 10^8$	$1.35 \cdot 10^8$	$1.2 \cdot 10^8$
$\tau_{\rm ion}$ [yrs]	$3.57 \cdot 10^8$	$7.91 \cdot 10^8$	$322.58 \cdot 10^8$
$\tau_{\rm brem}$ [yrs]	$0.26 \cdot 10^8$	$0.49 \cdot 10^8$	$19.8 \cdot 10^8$

6.3.2 Wavelength dependent depolarization effects

As explained in section 1.2.2, there are several wavelength dependent physical effects that can cause depolarization within NGC 4631. In section 6.2.3 we quantified the observed Faraday depolarization in NGC 4631 between C-band and L-band using the polarized intensities at each waveband. In this section we discuss separately the implications of differential Faraday rotation and internal Faraday dispersion to the observed polarized emission of NGC 4631.

Differential Faraday rotation

Differential Faraday rotation (DFR) originates in a medium which contains thermal electrons and a regular magnetic field. Differential Faraday rotation reduces the intrinsic polarization p_0 to the observed polarization p as (Burn 1966; Sokoloff et al. 1998):

$$\mathrm{p} = \mathrm{p}_0 \left(\frac{|\sin(2\,\mathrm{RM}\,\lambda^2)|}{|2\,\mathrm{RM}\,\lambda^2|} \right) \tag{6.11}$$

Depolarization due to DFR between C-band and L-band can be estimated by considering the ratio of the polarization degree at the two frequencies:

$$\mathrm{DP_{DFR}} = \frac{\mathrm{p_1}}{\mathrm{p_2}} = \frac{(|\sin(2\,\mathrm{RM}\,\lambda_1^2)|)(|2\,\mathrm{RM}\,\lambda_2^2|)}{(|2\,\mathrm{RM}\,\lambda_1^2|)(|\sin(2\,\mathrm{RM}\,\lambda_2^2)|)} \tag{6.12}$$

where λ_1 (λ_2) is the wavelength at L-band (C-band). With the Faraday depth values obtained with the C-band data, we have estimated the depolarization due to DFR in different regions within NGC 4631. Resulting values are shown in Table 6.5.

Results demonstrate DFR produces considerable depolarization between the two frequency bands. This is because at L-band significant DFR depolarization is expected for $|\mathrm{RM}| > 40\,\mathrm{rad\cdot m^{-2}}$. At shorter wavelengths, however, the depolarization due to DFR decreases. For example, employing rotation measures of $|\mathrm{RM}| = 400\,\mathrm{rad\cdot m^{-2}}$ would produce a DFR depolarization of ~ 0.55 between $\lambda 3.6$ and $\lambda 5$ cm (C-band).

TABLE 6.5— Estimates of the depolarization by differential Faraday rotation ($\mathrm{DP_{DFR}}$) in different regions within NGC 4631. Rotation measure (RM) values were obtained with the C-band data. The observed depolarization between C-band and L-band ($\mathrm{DP_{obs}}$(L,C)) is also included (see sect. 6.2.3 for details).

Region	**|RM|** **[rad $\cdot$ m^{-2}]**	**$\mathrm{DP_{DFR}}$(L,C)**	**$\mathrm{DP_{obs}}$(L,C)**
Central Region	400	0.06	0.1
Disk[a]	322	0.07	0.2
Disk-halo interface	142	0.09	0.5

[a] Excluding central region.

Internal Faraday dispersion

Internal Faraday dispersion (IFD) describes the depolarization due to small-scale variations of a turbulent magnetic field in the medium. This effect produces a degree of polarization given by (Burn 1966; Sokoloff et al. 1998):

$$\mathrm{p} = \mathrm{p_0}\left(\frac{1-\exp(-2\lambda^4\sigma_{\mathrm{RM}}^2)}{2\lambda^4\sigma_{\mathrm{RM}}^2}\right) \tag{6.13}$$

where p_0 is the intrinsic degree of polarization and σ_{RM} is the dispersion of intrinsic rotation measure within the volume of the telescope beam (in $\mathrm{rad\cdot m^{-2}}$). In a simplified model of a magnetoionic medium the RM dispersion can be written as (Arshakian & Beck 2011):

$$\sigma_{RM}^2 \cong \frac{(0.81\langle n_e\rangle\langle B_{t,\|}\rangle)^2 L\cdot d}{f} \tag{6.14}$$

Here, L is the pathlength through the ionized gas (in pc), $\langle n_e \rangle$ is the average thermal electron density within the volume along the pathlength traced by the telescope beam (in cm^{-3}), $\langle B_{t,\|} \rangle$ is the strength of the turbulent magnetic field along the LOS (in μG), d is the size of the turbulent cells (in pc) and f is the filling factor of the cells. Depolarization due to IFD between C-band and L-band can be estimated by considering the ratio of the polarization degree at the two frequencies:

$$\mathrm{DP_{IFD}} = \frac{\mathrm{p_1}}{\mathrm{p_2}} = \left(\frac{1-\exp(-2\lambda_1^4 \sigma_{\mathrm{RM}}^2)}{2\lambda_1^4 \sigma_{\mathrm{RM}}^2} \right) \left(\frac{2\lambda_2^4 \sigma_{\mathrm{RM}}^2}{1-\exp(-2\lambda_2^4 \sigma_{\mathrm{RM}}^2)} \right) \tag{6.15}$$

where λ_1 (λ_2) is the wavelength at L-band (C-band). To derive the depolarization, however, we need to have information on the thermal electron densities. We know the emission measure is related to the thermal electron density as:

$$EM = \int_0^L {n_e}^2(l)dl = \langle {n_e}^2 \rangle \cdot L = \frac{\langle n_e \rangle^2}{F_v} \cdot L \tag{6.16}$$

where F_v is the volume filling factor of the thermal electrons. In section 5.3 we derived emission measures for NGC 4631 using the Hα emission corrected for extinction with a combination of Hα and 24 μm measurements. Thermal electron densities in NGC 4631 were then estimated assuming a volume filling factor which ranges between $F_v = 5-20\%$, according to what has been observed for the Milky Way (Berkhuijsen et al. 2006; Berkhuijsen & Müller 2008). Values are listed in Table 6.6.

Assuming typical values for the size of the turbulent cells, d = 50 pc (Fletcher et al. 2011; Mao et al. 2015), and for the filling factor of the cells, f = 0.5 (Sun & Reich 2009), we estimate the RM dispersion and the depolarization attributed to internal Faraday dispersion between C-band and L-band. Results are presented in Table 6.6. As has already been found for several other galaxies, depolarization due to IFD is much stronger than the depolarization due to differential Faraday rotation. In the case of NGC 4631, depolarization due to internal Faraday dispersion it is at least by a factor of three stronger than the DFR depolarization.

The observed Faraday depolarization between L-band and C-band in the central area of NGC 4631 is 0.1, in the disk 0.2, and in the halo 0.5 (Table 6.5). The resulting IFR depolarization values are much smaller than the observed depolarization between L-band and C-band. The same applies for the DFR depolarization values obtained above. This implies we are perhaps tracing different layers of emission at C-band and at L-band. Therefore, the medium observed at L-band is Faraday thick and the polarization detected at this frequency must originate from a sheet of emission in the outskirts of the halo of NGC 4631.

If we take into account the same input values shown in Table 6.6 we can estimate the IFR depolarization between λ3.6 and 5 cm for the central area of NGC 4631. This

TABLE 6.6— Emission measures (EM), pathlength (L), average thermal electron densities ($\langle n_e \rangle$) and turbulent magnetic field strength along the LOS ($B_{t,\|}$) in different regions of NGC 4631. Estimates for the RM dispersion (σ_{RM}) and depolarization attributed to internal Faraday dispersion between C-band and L-band data (DP_{IFD}(L,C)) are found in the last two rows.

Region	**Central Region**	**Disk**[a]	**Disk-halo interface**
EM [$\mathrm{pc \cdot cm^{-6}}$]	2220	480	100
L [kpc]	29	24	20
$\langle n_e \rangle$ [$\mathrm{cm^{-3}}$]	0.06-0.12	0.03-0.06	0.016-0.03
$B_{t,\|}$ [μG]	9.3	6.4	5.7
d/f [pc]	100	100	100
σ_{RM} [$\mathrm{rad \cdot m^{-2}}$]	770-1540	241 - 482	105 - 196
DP_{IFD}(L,C)	0.005	0.005 - 0.009	0.01-0.04

---

[a] Excluding central region.

results in a value of ~0.3, much larger than that predicted between L-band and C-band. Therefore, the polarization in the central region of NGC 4631 is better probed at shorter wavelengths since the medium is more transparent to the polarized emission originating in the inner layers of the galaxy.

6.4 Conclusions

We analyzed the nonthermal emission of NGC 4631 at L-band and C-band by deriving its vertical scale heights and by estimating spectral indices between the two frequency bands (section 6.1). This is the first time the nonthermal spectral index distribution has been derived for an edge-on galaxy at a pixel-to-pixel basis. In addition, in section 6.2 we presented the polarized emission, Faraday depth distribution and intrinsic magnetic field orientation of NGC 4631 at L-band and C-band estimated by employing the RM-synthesis algorithm. The strength of the total, turbulent and ordered magnetic field in the galaxy were detailed in section 6.2.4. This is the first time maps of the strength of the turbulent and ordered magnetic field in the sky plane were derived for an edge-on galaxy. Furthermore, in this chapter we discussed the possible Faraday depolarization effects affecting the polarized emission of NGC 4631 and finally, we tentatively determined the dominating CRE energy loss mechanisms in several regions of NGC 4631. Our main conclusions are the following:

1. The synchrotron emission has the largest scale heights of the first component to the exponential fits at both frequency bands in the southeast and southwest of NGC 4631. In the SE strip the first component has a scale height at C-band (L-band) of 1.8 ± 0.1 kpc (2 ± 0.1 kpc), and in the SW strip the first component

has a scale height of 0.6 ± 0.05 kpc (1.3 ± 0.1 kpc). At C-band (L-band) these scale heights are a factor of 2-7 (2-3) larger than the synchrotron thin disk scale heights in the other parts of the galaxy. These areas coincide with disturbances in the disk also observed in the HI emission as supershells (Rand & van der Hulst 1993). Therefore, it seems we have not detected a thin disk in these regions within NGC 4631. We believe this might be associated with the disturbances present in these areas of the disk and/or it might be an indication that the disk is warped. Both scenarios seem to be related to the gravitational interaction the galaxy is undergoing.

2. The scale heights of the synchrotron thin disk observed at C-band (L-band) are on average 22% (9%) larger than the scale heights of the total radio thin disk in NGC 4631 (excluding the SE and SW strips). This is due to the thermal component of the radio continuum. The mean scale height of the synchrotron thick disk at C-band (L-band) is 3.4 ± 0.8 kpc (4.5 ± 0.6 kpc).

3. The Faraday depths at C-band and L-band are characterized by a smooth large-scale distribution, indicating that NGC 4631 has a regular magnetic field.

4. The background radio galaxy to the southwest of NGC 4631 has average degree of polarization of 6% at L-band. The Faraday depths are rather uniform over the two lobes with an average value of $21 \pm 13\ \mathrm{rad \cdot m^{-2}}$. The intrinsic magnetic field is orientated parallel to the radio galaxy's main axis.

5. The total magnetic field of NGC 4631 has a mean strength of $\langle \mathrm{B_{eq}} \rangle \approx 9 \pm 0.7\ \mu\mathrm{G}$ in the disk, and a mean strength of $\langle \mathrm{B_{eq}} \rangle \approx 7 \pm 1.5\ \mu\mathrm{G}$ in the halo. In addition, the ordered magnetic field in the plane of the sky has a mean strength of $\langle \mathrm{B_{o,\perp}} \rangle \approx 1\ \mu\mathrm{G}$ in the disk and $\langle \mathrm{B_{o,\perp}} \rangle \approx 2\ \mu\mathrm{G}$ in the halo, which represent lower limits. The mean degree of field order in the halo is a factor of two higher than in the disk.

6. Calculation of the loss timescales leads to conclude that synchrotron losses dominate the propagation of the cosmic ray electrons in NGC 4631 at C-band. This explains the steepening of the nonthermal spectral indices in the halo with respect to the disk.

7. Estimates of the depolarization due to differential Faraday rotation and to internal Faraday dispersion imply the medium is Faraday thick at L-band and therefore, the polarization detected at this frequency probably originates from a screen of emission on the outskirts of NGC 4631. The polarization along the disk of NGC 4631 is better probed at shorter wavelengths since the medium is

more transparent to the polarized emission originating in the inner layers of the galaxy.

7

Does NGC 4631 have a plane-parallel field along its disk?

"We are just an advanced breed of monkeys
on a minor planet of a very average star.
But we can understand the Universe.
That makes us something very special."
Stephen Hawking

All of the edge-on spiral galaxies observed so far present a similar magnetic field configuration, which consists of a field in the disk parallel to the plane of the galaxy and an X-shaped field in the halo. Only NGC 4631 seems to have a different field orientation in its disk. Along the eastern and western sides of the disk the magnetic field orientation is parallel to the galactic plane of NGC 4631 (refer to section 2), but in the central region of the disk a vertical field seems to dominate at low angular resolution. The plane-parallel magnetic field in the disk is the expected edge-on projection of the spiral magnetic field structure observed in face-on galaxies. As discussed in section 6.3.2, the center of the galaxy suffers from strong Faraday depolarization effects which become more severe with decreasing frequencies. Therefore, in order to clarify whether NGC 4631 has a unique magnetic field configuration in the central region along its disk, we analyze high-resolution Faraday-corrected polarization data at higher frequencies, i.e. 8.35 GHz. Since our 8.35 GHz interferometer data do not have wide bandwidths and were not observed in narrow frequency channels, we cannot perform RM-synthesis. Therefore, we obtain the intrinsic magnetic field orientation with the classical rotation measure approach derived with the observed polarization angles at 8.35 and 4.85 GHz.

An attempt to answer this question was already made by Mora (2012). However, with further analysis we have now determined that combining interferometer with single-dish data causes strong beam depolarization and therefore, limits the possibility of detecting the magnetic field orientation along the central region of the disk of the galaxy. We will demonstrate this in section 7.2.2. Hence, this work is based on interferometer data only and improves the previous study of Mora (2012). Our results have been published in Mora & Krause (2013) (section 3.6).

7.1 Very Large Array (VLA) data

The galaxy NGC 4631 was observed for 9 hrs at λ6.2 cm in April 1999 with the VLA telescope in its D array configuration (Project AD 896). The data were available from Mora (2012). The calibration and reduction was done in the AIPS data processing package. The nearby point source 1225+368 was used for phase and instrumental polarization calibration. The polarization position angle and flux-calibration were done by using 3C286 according to the flux scale published by Baars et al. (1977). The UV data were self-calibrated for phase and amplitude. The maps of the three Stokes parameters I, U, and Q have a linear resolution of $12\overset{''}{.}67 \times 12\overset{''}{.}08$ FWHM. The maps were corrected for the primary beam attenuation. The map of the total intensity together with the linear polarization is shown in figure 7.1. The rms noise values are 26 $\mu\mathrm{Jy/beam}$ in total intensity and 14 $\mu\mathrm{Jy/beam}$ in Stokes Q/U (at $12\overset{''}{.}67 \times 12\overset{''}{.}08$ FWHM).

Data from the VLA at λ3.6 cm were available from Golla & Hummel (1994). Observations we performed in the D array configuration for a net observing time of 7.2 hrs. All maps were corrected for the primary beam attenuation. The rms values of the maps is 28 $\mu\mathrm{Jy/beam}$ in total intensity and 15 $\mu\mathrm{Jy/beam}$ in Stokes Q/U (at $12''$ FWHM). In order to analyze the large-scale structure and increase the signal-to-noise ratio, we smoothed our maps (at both frequencies) in all Stokes parameters to a resolution of $25''$ and produced maps of the polarized intensity and polarization angle at this angular resolution. The total and polarized intensity of NGC 4631 at λ3.6 cm is shown in figure 7.2.

7.2 Analysis of the data

7.2.1 Rotation measure distribution between λ3.6 and 6.2 cm

As has already been mentioned in section 6.2.2, the contribution of the Galactic foreground component into our rotation measures is very small in the direction of the sky in which NGC 4631 is located. Nevertheless, we corrected for this by subtracting the value of $\mathrm{RM_{fg}} = (-4 \pm 3)\ \mathrm{rad \cdot m^{-2}}$ (Heald et al. 2009) from our rotation measures.

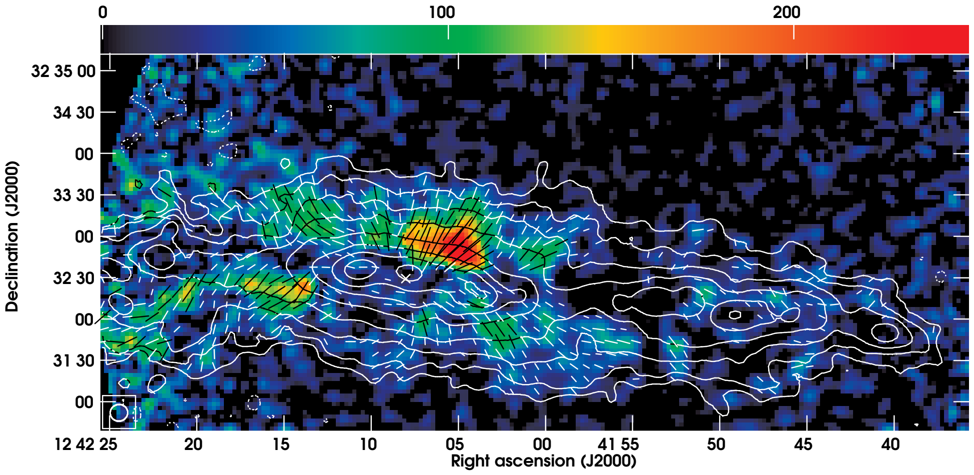

FIGURE 7.1— VLA maps at $\lambda 6.2$ cm of NGC 4631 with apparent magnetic field orientation. Contours represent the total radio intensity and the colorscale shows the polarized emission in μJy/beam. The length of the vectors is proportional to the polarized intensity ($1'' \widehat{=} 8.3$ μJy/beam). The half-power beam width is $12\farcs67 \times 12\farcs08$ and the rms noise (σ) is 26 μJy/beam. Contour levels are given by $\sigma \cdot (-3, 3, 6, 12, 24, 48, 96, 192, 384)$. Primary beam correction was applied. The “x” pinpoints the dynamical center of the galaxy.

Mora (2012) determined that due to the $n \cdot \pi$ ambiguity we would have ambiguous rotation measure values of $\mathrm{RM} = \pi/({\lambda_2}^2 - {\lambda_1}^2) \approx \pm 1230\ \mathrm{rad} \cdot \mathrm{m}^{-2}$, at wavelengths of 3.6 and 6.2 cm. The overall RM distribution obtained does not present values that exceed $\pm 615\ \mathrm{rad} \cdot \mathrm{m}^{-2}$. Even without being affected by the $n \cdot \pi$ ambiguity, a rotation of the polarization angle by 90° along the LOS through the emitting source leads to strong differential Faraday depolarization within the galaxy. This is expected at $\lambda 6.2$ cm for rotation measure values of $|RM| \approx |(\pm\pi/2)/(6.2 \cdot 10^{-2})^2| \approx 400\ \mathrm{rad} \cdot \mathrm{m}^{-2}$, and implies that the galaxy is no longer Faraday thin and that the derived rotation measure values may be incorrect (Mora 2012). To be on the safe side we set our rotation measure threshold to $|RM| \leq 350\ \mathrm{rad} \cdot \mathrm{m}^{-2}$ and clipped both the rotation measure distribution and the polarization angles to satisfy this condition.

The rotation measure distribution derived with the VLA data at $\lambda 3.6$ and 6.2 cm is presented in figure 7.3 at an angular resolution of $25''$. Overall, the rotation measure distribution is smooth and regular. It is in agreement with the C-band Faraday depth distribution presented in section 6.2.2.

7.2.2 Intrinsic magnetic field orientation in the sky plane

In order to obtain the intrinsic magnetic field orientation in NGC 4631, the observed polarization angles at $\lambda 3.6$ and 6.2 cm were corrected for Faraday rotation with the

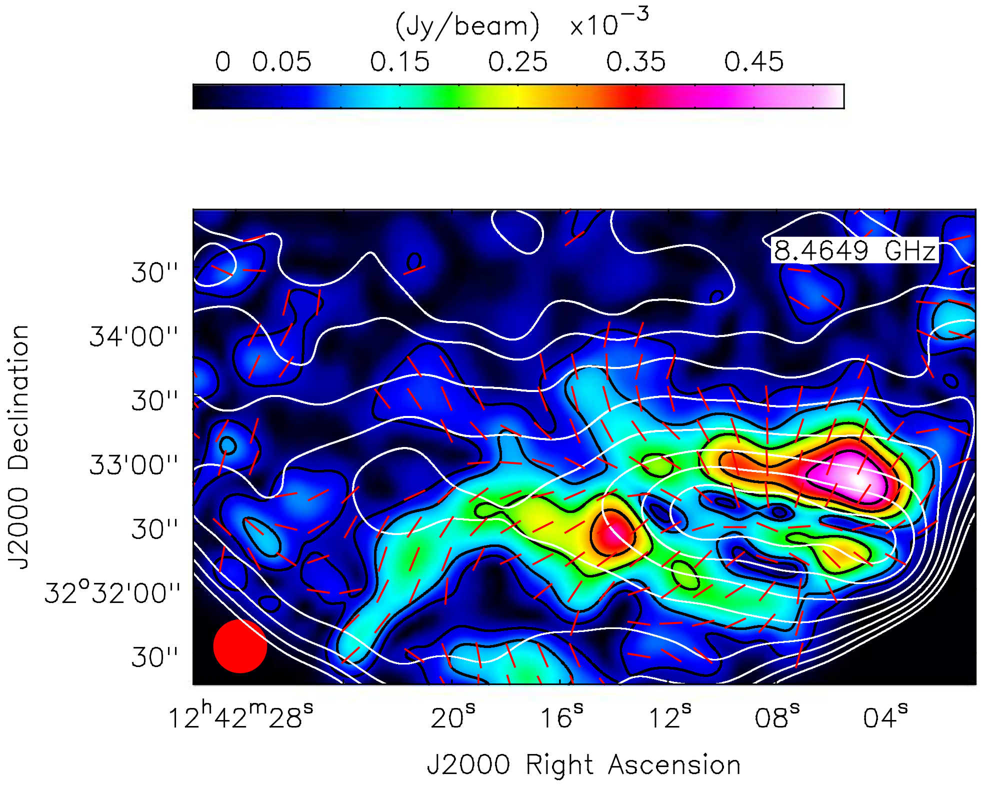

FIGURE 7.2— VLA maps at λ3.6 cm of NGC 4631 smoothed to an angular resolution of $25''$. The colorscale shows the polarized emission and the red vectors represent the apparent magnetic field orientation. Black contours correspond to the polarized emission: $(25\ \mu\mathrm{Jy/beam}) \cdot (2,4,8,12,16)$. White contours correspond to the total radio emission: $(40\ \mu\mathrm{Jy/beam}) \cdot (3,6,12,24,48,96,192,384)$. Primary beam correction was applied.

rotation measures presented in figure 7.3. We determined the vectors at those locations where the polarized intensity at both wavelengths is above 2σ and where the rotation measures are below $|\mathrm{RM}| \leqslant 350\ \mathrm{rad \cdot m^{-2}}$, which is where the derived values for the rotation measures are reliable as discussed in section 7.2.1. The intrinsic magnetic field orientation of NGC 4631 derived with the VLA data is presented in figures 7.3 and 7.4. By error propagation, the uncertainty in the intrinsic polarization angles is at λ6.2 cm $\sim 34°$ and at λ3.6 cm $\sim 18°$, in areas where the polarized emission is twice the rms noise. This uncertainty, however, scales down linearly with increasing polarized intensity.

The polarized intensity shows a minimum along the galactic midplane at both wavelengths. This is expected as Faraday depolarization effects are usually strongest

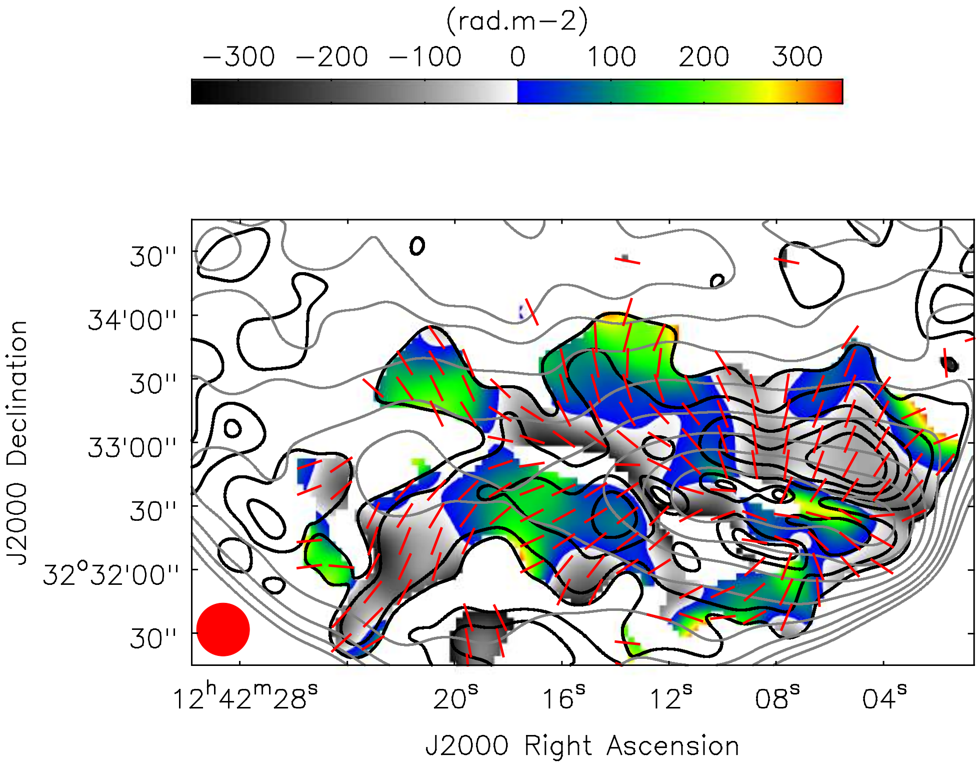

FIGURE 7.3— Rotation measure distribution of NGC 4631 estimated between λ3.6 cm and 6.2 cm, with intrinsic magnetic field orientation at λ3.6 cm. Vectors were clipped at the 2σ level of the polarized intensity maps (at both frequencies) and where $|\mathrm{RM}| \geq 350\ \mathrm{rad \cdot m^{-2}}$. All values are from the data at an angular resolution of 25″ FWHM. Black contours correspond to the λ3.6 cm polarized emission: $(25\ \mu\mathrm{Jy/beam}) \cdot (2, 4, 8, 12, 16)$. Grey contours correspond to the λ3.6 cm total radio emission: $(40\ \mu\mathrm{Jy/beam}) \cdot (3, 6, 12, 24, 48, 96, 192, 384)$.

in this area because the thermal electron density, the LOS, and the magnetic field strength are largest. A depolarization along the midplane has already been observed in several other spiral edge-on galaxies, for example NGC 5775 (Soida et al. 2011). Furthermore, if there is a magnetic field parallel to the disk accompanied by strong vertical magnetic fields above and below the disk, we also expect strong beam polarization along the region of the projected transition between both magnetic field components. To minimize the beam depolarization, observations with high resolution are required, while high frequency observations reduce the Faraday depolarization. However, the merging of single-dish data to the interferometer data increases the zone of depolarization along the midplane of NGC 4631 due to the large beam

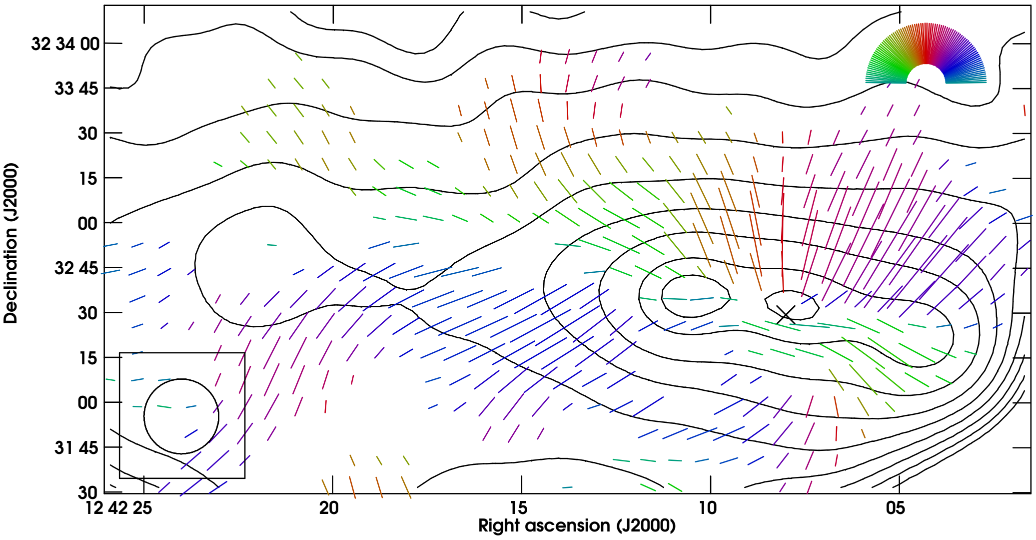

FIGURE 7.4— Intrinsic magnetic field orientation perpendicular to the LOS at $\lambda 3.6$ cm derived only with VLA data. Angular resolution is $25''$ FWHM. The contours show the VLA $\lambda 3.6$ cm total radio emission. The length of the vectors is proportional to the VLA $\lambda 3.6$ cm polarized intensity ($1'' \widehat{=} 15$ μJy/beam). These vectors were clipped at the 2σ level of the polarized intensity VLA maps (at both frequencies) and where $|\mathrm{RM_{VLA}}| \geq 350\,\mathrm{rad \cdot m^{-2}}$. The contour levels correspond to $(40\ \mu\mathrm{Jybeam}) \cdot (3, 6, 12, 24, 48, 96, 192, 384, 522)$. The "x" pinpoints the dynamical center of the galaxy. In the electronic version the angles are color coded as shown in the colorfan in the upper-right corner.

depolarization in the single-dish data. This is specially expected along the transition zone of two large-scale magnetic field patterns that are almost perpendicular to each other: the beam depolarization in the single-dish maps reduces the observed U- and Q-signal at positions where the interferometer beam still detects a signal.

To illustrate this effect we show the intrinsic magnetic field orientation of the galaxy obtained by combining the VLA data with Effelsberg data at 4.85 and 8.35 GHz in figure 7.5. Please refer to the work of Mora (2012) for details on the single-dish data and the combination. These polarization angles were corrected for Faraday rotation with rotation measure values derived with a combination of VLA and Effelsberg data. In addition, they were clipped at the 2σ level of the VLA+Eff. polarized intensity maps (at $\lambda 3.6$ and 6.2 cm) and where the absolute value of the rotation measures exceeded $350\,\mathrm{rad \cdot m^{-2}}$. Comparing figures 7.4 and 7.5, one can see that the amount of magnetic field vectors along the central region of the disk are diminished when combining with single-dish data, while the number of vectors in the halo increase. The two maps were derived and clipped in exactly the same way, the only difference is that the plot shown in figure 7.5 was obtained by combining with Effelsberg data. Merging with Effelsberg data is essential for recovering the large-scale emission of the total intensity and the linear polarization in NGC 4631. In special cases, however, the polarized signal may even be weakened by the merging process, e.g., along a transition zone of large-scale magnetic field patterns with abruptly changing field orientations.

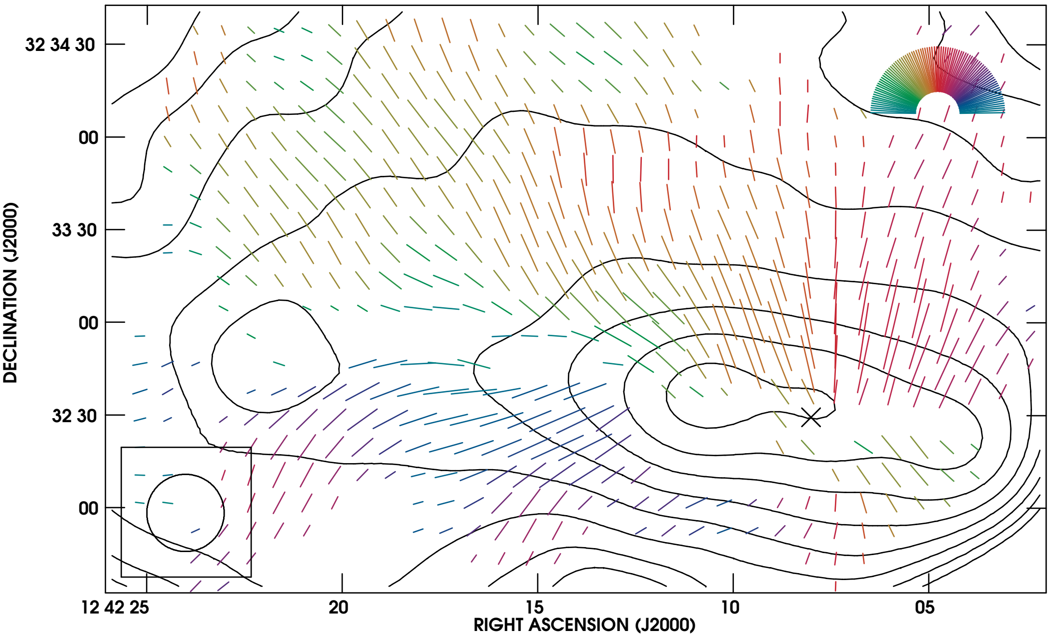

FIGURE 7.5— Intrinsic magnetic field orientation perpendicular to the LOS at $\lambda 3.6$ cm derived from the combination of VLA and Effelsberg data. Angular resolution is $25''$ FWHM. The contours show the VLA+Eff. $\lambda 3.6$ cm total radio emission. The length of the vectors is proportional to the VLA+Eff. $\lambda 3.6$ cm polarized intensity. These vectors were clipped at the 2σ level of the VLA+Eff. polarized intensity maps (at both frequencies) and where $|\mathrm{RM}_{\mathrm{VLA+Eff.}}| \geq 350\,\mathrm{rad}\cdot\mathrm{m}^{-2}$. The contour levels correspond to $(43\ \mu\mathrm{Jy/beam})\cdot(3,6,12,24,48,96,192,384)$.

In figure 7.4 we can clearly see that the halo magnetic field orientation in the eastern side of the galaxy is almost symmetric with respect to the major axis of NGC 4631 and that it curves radially outwards. At the edges of the western side of the galaxy we can also distinguish that the halo magnetic field begins to curve outwards. This forms part of the X-shaped halo magnetic field seen in other edge-on galaxies. Above the central region of the disk the halo magnetic field is orientated perpendicular to the major axis of the galaxy, and in section 6.2.1 we demonstrated that there are vertical components also below the central area which we were able to recover with the C-band data.

Along the central region of the disk the magnetic field vectors are oriented parallel to the galaxy's plane extending over several beam sizes. The disk-parallel magnetic field in the outer regions along the midplane had previously been indicated by Krause (2009) with Effelsberg observations, however, the magnetic field orientation along the center of the disk had never been clearly observed. With the plane-parallel vectors in figure 7.4 we can now see for the first time the missing link of a disk-parallel magnetic field in the central 5-7 kpc in NGC 4631. The magnetic field derived with our L-band data (section 6.2), also supports the conclusion that the field orientation is parallel to the major axis of the galaxy in the central region of NGC 4631.

7.2.3 Ratio between the size of turbulent cells and the filling factor of the cells

As demonstrated in section 6.3.2, the differential Faraday rotation within the galaxy is not as strong as the Internal Faraday dispersion. Therefore, one can assume that the observed Faraday depolarization in NGC 4631 is mostly due to internal Faraday dispersion effects. By introducing observed Faraday depolarization values in equation 6.15 one can derive the RM dispersion. In addition, with equation 6.14 rough estimates of the ratio between the size of turbulent magnetic field cells and the filling factor of the cells (d/f) can be calculated. With the observed Faraday depolarization distribution between λ3.6 and 6.2 cm derived by Mora & Krause (2013), we obtained the mean depolarization ($DP_{obs}(6.2,3.6)$) in the central region, the disk (excluding the central area) and the disk-halo interface of NGC 4631. Values are shown in Table 7.1. With the parameters that have already been presented in section 6.3.2, we estimate the ratio d/f within these three regions of NGC 4631.

The resulting d/f ratio is shown in Table 7.1, values represent upper limits since they were derived assuming that internal Faraday dispersion is the only effect responsible for the observed depolarization in NGC 4631. For the central region of the galaxy the ratio ranges between 4 to 15 pc. If we assume a filling factor of f = 0.1, the size of the turbulent cells in the central area of NGC 4631 is approximately $d \approx 40 - 150$ pc. For the disk-halo interface, if one takes into consideration the filling factor of the cells derived for the Milky Way (Sun & Reich 2009), f = 0.5, we obtain a turbulent cell size of $d \approx 92 - 320$ pc. These values agree with those predicted by Sokoloff et al. (1998) for the disk and halo of spiral galaxies. In M 51 Shneider et al. (2014) estimated that the size of the turbulent cells in the disk of this galaxy range between 40-61 pc and in the halo 157-253 pc.

7.3 Discussion and conclusions

In Sect. 7.2.2 we described our results for the magnetic field orientation of NGC 4631 perpendicular to the LOS derived only with VLA data. In the halo it is characterized

TABLE 7.1— Observed Faraday depolarization between λ3.6 and 6.2 cm (DP$_{\rm obs}$(6.2,3.6)), emission measures (EM), pathlength (L), average thermal electron densities ($\langle n_e \rangle$) and turbulent magnetic field strength along the LOS (B$_{t,||}$) in different regions of NGC 4631. Estimates for the RM dispersion (σ_{RM}) and the ratio between the size of the turbulent cells and the filling factor of the cells (d/f) are found in the last two rows.

Region	**Central Region**	**Disk**[a]	**Disk-halo interface**
DP$_{\rm obs}$(6.2,3.6)[b]	0.4	0.5	0.8
EM [pc $\cdot$ cm^{-6}]	2220	480	100
L [kpc]	29	24	20
$\langle$n$_{\rm e}\rangle$ [cm^{-3}]	0.06-0.12	0.03-0.06	0.016-0.03
B$_{\rm t,\|\|}$ [μG]	9.3	6.4	5.7
$\sigma_{\rm RM}$ [rad $\cdot$ m^{-2}]	300	255	132
d/f [pc]	4-15	28-112	46-160

---

[a] Excluding central region.

[b] Values obtained from Mora & Krause (2013).

by an overall X-shaped configuration together with a strong perpendicular field above and below the central region of the galaxy. The edge-on spiral galaxies NGC 4666 (Soida 2005) and NGC 5775 (Soida et al. 2011) also have prominent perpendicular components above and below their central regions. Dynamo simulations by Hanasz et al. (2009) may be able to explain not only this X-shaped morphology but also these vertical fields.

Faraday-corrected Effelsberg observations at λ3.6 cm show a plane-parallel magnetic field in the outer eastern and western regions along the midplane (Krause 2009; Mora 2012). However, we have demonstrated that combining interferometer with single-dish data causes strong beam depolarization along the central region of the disk of NGC 4631 and therefore reduces the observed U- and Q-signal limiting the detection of the magnetic field orientation in this area. With the plane-parallel vectors in figure 7.4 derived with VLA data alone, we can now see for the first time the missing link of a disk-parallel magnetic field in the central 5-7 kpc in NGC 4631. Hence, NGC 4631 does not have a unique magnetic field configuration since it also contains a disk-parallel magnetic field along its midplane as expected from dynamo theory, and as has been detected in all of the other face-on and edge-on galaxies observed so far (e.g., Beck & Wielebinski 2013). This plane-parallel magnetic field is thought to be generated by a large-scale $\alpha - \Omega$ dynamo. The galaxy NGC 4631 was regarded as an exception, but our research indicates this is not the case.

The mean magnetic field strength in the disk of NGC 4631, $\langle$B$_{\rm eq}\rangle \approx 9 \pm 0.7$ μG (see section 6.2.4), is comparable to the total field strength of the star forming edge-on galaxy NGC 5775 (Soida et al. 2011), but it is not as strong as the strength in the starburst galaxy NGC 253 (Heesen et al. 2009b) which also has strong star formation along its disk. However, the mean strength of the total magnetic field in the halo, $\langle B_{eq} \rangle \approx 7 \pm 1.5\ \mu G$, is relatively higher than in other the edge-on galaxies studied so far. Mora (2012) comes to a similar conclusion with the magnetic field strengths derived with her Effelsberg data. In addition, the mean strength of the ordered field perpendicular to the LOS in the halo $\langle B_{o,\perp} \rangle \approx 2\ \mu G$ is larger than the mean strength of the ordered field in the disk $\langle B_{o,\perp} \rangle \approx 1\ \mu G$. Hence, some differential Faraday rotation in the disk as well as in the halo is expected, together with strong Internal Faraday dispersion in the disk. This, together with strong beam depolarization along the transition zone between the horizontal disk field and the mainly vertical halo field in the central region of NGC 4631, might explain why the plane-parallel field in this disk was so difficult to detect when compared to other galaxies.

8

Summary

Let's do something difficult,
in the most difficult way possible!!!
Anonymous (2015)

NGC 4631 is a nearby edge-on spiral galaxy with a spectacular radio halo, one of the largest observed among edge-on galaxies. This makes the galaxy an ideal target to study the properties of synchrotron halos, the propagation of cosmic rays from the disk into the halo and to investigate how the magnetic field out of the plane relates to the magnetic field in the disk of the galaxy. Radio observations of the edge-on spiral galaxy NGC 4631 were performed with the Karl G. Jansky Very Large Array (EVLA), during its commissioning phase as part of the project *Continuum HAlos in Nearby Galaxies- an EVLA Survey (CHANG-ES)* during 2011-2012. The data were obtained at C-band in the C & D array configurations, and at L-band in the B, C & D array configurations. At C-band the data covers a total bandwidth of 2 GHz centered at 5.99 GHz, while at L-band the data covers a total bandwidth of 512 MHz centered at 1.57 GHz. In order to recover the large-scale emission that is missing due to the incomplete u,v sampling of the interferometer the data were combined with single-dish Effelsberg data. NGC 4631 was observed with the Effelsberg telescope at 1.42 GHz in 2002 and at 4.85 GHz in 2014. Prior to merging, the Effelsberg data were rescaled to the corresponding central frequency of the EVLA observations taking into account the spectral index of the galaxy. At C-band (L-band) we recovered missing flux attributed to the large-scale structures which amounted to $\sim$27% ($\sim$11%) of the total flux-density of the galaxy .

We fit a single power law to the total flux-densities of NGC 4631 measured with single-dish data (including values obtained from the literature), and obtain a total integrated spectral index of $\alpha_{tot} = -0.81 \pm 0.03$ ($I_\nu \propto \nu^\alpha$). In addition, we derived the total spectral index distribution of the galaxy between C-band and L-band. To quantify the extent of the radio halo in NGC 4631 independently of sensitivity and overall radio intensity, the total vertical scale heights were derived in both frequency bands. The mean vertical scale height at C-band for the thick disk (3.4 ± 0.9 kpc) is larger by a factor of 1.9 compared to the mean scale height of the thick disk found in five other edge-on spiral galaxies (Krause 2012). There are several indications that convection may be strong in NGC 4631, which may originally be related to the tidal interaction with its neighboring galaxies. Because of the tidal interaction, material may be dragged out from or even stream onto NGC 4631. Hence, this interaction may explain why the thick disk scale heights deviate from those of the other galaxies without strong tidal interaction.

The radio continuum emission in spiral galaxies emerges from two emission mechanisms, thermal free-free and nonthermal synchrotron emission. Synchrotron emission can be used to infer properties of the magnetic field and to study the propagation of cosmic ray electrons (CREs). However, to do this one must first estimate the thermal component and subtract it from the total radio emission. We derive the thermal emission of NGC 4631 on a pixel-by-pixel basis at C-band and L-band with three different approaches. The purpose of using three different methods to estimate the thermal emission of NGC 4631 was to determine the best approach to account for dust extinction in the context of edge-one galaxies. Method one employs the technique developed by Tabatabaei et al. (2007), which is based on correcting the Hα emission for extinction using the $\mathrm{I}_{70\mu\mathrm{m}}/\mathrm{I}_{160\mu\mathrm{m}}$ dust ratio. The second method combines Hα and 24 μm data to correct for extinction and uses the calibrations estimated by Calzetti et al. (2007) and Kennicutt et al. (2009). Method three corrects for extinction using only 24 μm measurements and the calibrations derived by Zhu et al. (2008) and Relaño et al. (2007).

For method one it is necessary to derive the dust temperature distribution using measurements at 70 μm and 160 μm. The dust temperature estimates are well in agreement with values that were derived by fitting the spectral energy distribution between 70-500 μm (Meléndez et al. 2015). The Hα emission is optically thick along the entire disk of NGC 4631 and it becomes optically thin with larger distance from the plane. Hence, the Hα emission detected in the region of the disk probably originates in the outer layers of NGC 4631. Therefore, the thermal/nonthermal separation method developed by Tabatabaei et al. (2007; method one) should be applied with caution to edge-on galaxies due to the optically thick nature of the disk emission. However, in the optically thin regions, the calibration of Kennicutt et al. (2009) to correct the Hα emission for extinction with a combination of Hα and 24 μm measurements yields results similar to method one. Therefore, we state that this calibration can be used at small spatial scales for optically thin regions. The calibrations proposed by Zhu et al. (2008) and Relaño et al. (2007), which scale the 24 μm luminosity to the extinction-corrected Hα emission (method three), appear to overestimate the correction for extinction when compared to results obtained with the other two methods. We conclude that method two is the best way to estimate the amount of free-free emission in NGC 4631 and other edge-on galaxies. The integrated thermal flux-density of NGC 4631 is 61±13 mJy at C-band and 70±13 mJy at L-band. This corresponds to a global thermal fraction at C-band (L-band) of 15±3% (6±1%).

We analyze the properties of the synchrotron emission in NGC 4631 at L-band and C-band by deriving its vertical scale heights and by estimating spectral indices between the two frequency bands. This is the first time the distributions of the synchrotron emission and synchrotron spectral indices have been derived for an edge-on galaxy on a pixel-by-pixel basis. The mean scale height of the synchrotron-emitting thick disk at C-band (L-band) is 3.4 ± 0.8 kpc (4.5 ± 0.6 kpc). The scale heights of the synchrotron-emitting thin disk observed at C-band (L-band) are on average 22% (9%) larger than the scale heights of the total radio thin disk in NGC 4631. Taking into account estimates for the CRE energy loss timescales, we conclude that synchrotron losses dominate the propagation of the cosmic ray electrons in NGC 4631. This explains the steepening of the nonthermal spectral indices in the halo with respect to the disk.

The disturbance in the eastern side of the disk of NGC 4631 is visible in the HI emission as a large supershell (Rand & van der Hulst 1993) which has strongly been indicated to be caused by tidal encounters. This disturbance is reflected in the radio continuum emission in two ways. Firstly, the scale heights at both frequency bands of the first component of the exponential fits to the total radio emission (the thinner component) are larger in this area than in the rest of the disk and secondly, the disk-halo interface in the southeastern side shows flatter total radio spectral indices than in other parts of the galaxy. The disk of NGC 4631 is also found to be disturbed in its western side, where there is a smaller HI supershell (Rand & van der Hulst 1993). The largest scale heights at both wavebands of the first component of the exponential fits to the synchrotron emission correspond to the emission in the southeast and southwest of the galaxy. In the SE the synchrotron emission at C-band (L-band) has a first component scale height of 1.8 ± 0.1 kpc (2 ± 0.1 kpc), and in the SW the first component has a scale height of 0.6 ± 0.05 kpc (1.3 ± 0.1 kpc). At C-band (L-band) these scale heights are a factor of 2-7 (2-3) larger than the scale heights of the synchrotron-emitting thin disk found in other parts of the galaxy. Therefore, it seems we have not detected a thin disk in these regions within NGC 4631. We believe this might be associated with the disturbances present in these areas of the disk and/or it might be an indication that the disk is warped. Both scenarios seem to be related to the gravitational interaction the galaxy is undergoing.

In addition, we present the distribution of polarized emission, Faraday depths, and the intrinsic magnetic field orientation of NGC 4631 at L-band and C-band which we estimate by employing the RM-synthesis algorithm. The orientation of the magnetic field component perpendicular to the line-of-sight (LOS) in the halo of NGC 4631 is characterized by an overall X-shaped configuration together with a strong perpendicular field above and below the central region of the galaxy. The Faraday depths at each frequency band are characterized by a smooth large-scale distribution, indicating that the disk and halo of NGC 4631 has a regular magnetic field. The Faraday depths in the northern disk-halo interface of NGC 4631 vary smoothly from $\sim 200~\mathrm{rad\cdot m^{-2}}$ to about -150 $\mathrm{rad\cdot m^{-2}}$ in a quasi-periodic pattern, indicating that the magnetic field along the LOS has a systematic change in direction on scales of about 1.9 kpc (half wavelength). A possible explanation of the origin of these features is that they may be attributed to magnetic loops extending out of the sky plane.

We calculate the strengths of the total, turbulent and ordered magnetic field in the galaxy. This is the first time maps of the strength of the turbulent and ordered magnetic field in the sky plane were derived for an edge-on galaxy. The total magnetic field of NGC 4631 has a mean strength of $\langle \mathrm{B_{eq}} \rangle \approx 9 \pm 0.7~\mu\mathrm{G}$ in the disk, and a mean strength of $\langle \mathrm{B_{eq}} \rangle \approx 7 \pm 1.5~\mu\mathrm{G}$ in the halo. In addition, the ordered magnetic field in the plane of the sky has a mean strength of $\langle \mathrm{B_{o,\perp}} \rangle \approx 1~\mu\mathrm{G}$ in the disk and $\langle \mathrm{B_{o,\perp}} \rangle \approx 2~\mu\mathrm{G}$ in the halo, which represent lower limits since values were derived with the observed polarization which is affected by depolarization effects. The mean degree of order of the magnetic field in the halo is a factor of two higher than in the disk.

By calculating the depolarization due to differential Faraday rotation and internal Faraday dispersion we show that the medium along the disk and the disk-halo interface is Faraday thick at L-band. Therefore, the polarization detected at this frequency probably originates from a screen of emission on the outskirts of NGC 4631. The polarization along the disk of NGC 4631 is better probed at shorter wavelengths since the medium is more transparent to the polarized emission originating from the inner layers of the galaxy. In addition, by assuming that the observed Faraday depolarization between $\lambda 3.6$ and 6.2 cm in NGC 4631 is only due to internal Faraday dispersion effects, we calculate rough estimates for the ratio between the size of turbulent magnetic field cells and the filling factor of these cells.

All of the edge-on spiral galaxies observed so far present a similar magnetic field configuration, which consists of a field in the disk parallel to the plane of the galaxy and an X-shaped field in the halo. Only NGC 4631 seems to have a different field orientation in its disk. Along the eastern and western sides of the disk the magnetic field orientation is parallel to the galactic plane of NGC 4631, but in the central region of the disk a vertical field seems to dominate at low angular resolution. To uncover the disk magnetic field in the center of NGC 4631 we analyze high-resolution Faraday-corrected polarization data at shorter wavelengths, $\lambda 3.6$ cm, observed using the Very Large Array Telescope (VLA). There is strong Faraday depolarization along the galactic plane of the galaxy and in addition, we demonstrate that the merging of single-dish data to the interferometer data increases the zone of depolarization along the midplane of NGC 4631, specially in the central area of the disk, due to the large beam depolarization in the single-dish data. Our study indicates that the magnetic field orientation along the central 5-7 kpc of the disk is parallel to the midplane of the galaxy, which is only clearly visible in the high-resolution $\lambda 3.6$ cm interferometer data. Therefore, we confirm that NGC 4631 also has a magnetic field structure plane-parallel along its entire disk, similar to all other edge-on galaxies observed up to now. The plane-parallel magnetic field in the disk is the expected edge-on projection of the spiral magnetic field structure observed in face-on galaxies.

The spectral index distribution of the background radio galaxy to the southwest of NGC 4631 is flat in the outskirts of the lobes and steepens towards the core. This spectral index distribution is typical of FR II radio galaxies and is consistent with the backflow model (Leahy & Williams 1984; Leahy et al. 1989). According to this model, CREs are reaccelerated in the hot spots, and flow back towards the nucleus due to the pressure gradient created by the jet of the active galactic nucleus (AGN). Therefore, the emission closer to the core comes from an older population of CREs than the emission from the hot spots, which produces a steeper radio spectrum close to the core of the AGN. Furthermore, the background radio galaxy has an average degree of polarization of 6% at L-band. The Faraday depths are rather uniform over the two lobes with an average value of 21 ± 13 rad $\cdot$ m^{-2}. The intrinsic magnetic field is orientated parallel to the radio galaxy's main axis.

Bibliography

Aaronson, M. 1978, PASP, 90, 28

Adebahr, B., Krause, M., Klein, U., et al. 2013, A&A, 555, A23

Alton, P. B., Davies, J. I., & Bianchi, S. 1999, A&A, 343, 51

Aniano, G., Draine, B. T., Gordon, K. D., & Sandstrom, K. 2011, PASP, 123, 1218

Ann, H. B. & Park, J.-C. 2006, New A, 11, 293

Ann, H. B., Seo, M. S., & Baek, S.-J. 2011, Journal of Korean Astronomical Society, 44, 23

Arshakian, T. G. & Beck, R. 2011, MNRAS, 418, 2336

Arshakian, T. G., Beck, R., Krause, M., Sokolff, D., & Stepanov, R. 2009, ArXiv e-prints

Baars, J. W. M., Genzel, R., Pauliny-Toth, I. I. K., & Witzel, A. 1977, A&A, 61, 99

Basu, A., Beck, R., Schmidt, P., & Roy, S. 2015, MNRAS, 449, 3879

Basu, A., Mitra, D., Wadadekar, Y., & Ishwara-Chandra, C. H. 2012, MNRAS, 419, 1136

Basu, A. & Roy, S. 2013, MNRAS, 433, 1675

Battaner, E. & Lesch, H. 2000, ArXiv Astrophysics e-prints

Beck, R. 2001, Space Sci. Rev., 99, 243

Beck, R. 2007, A&A, 470, 539

Beck, R. 2015, in Astrophysics and Space Science Library, Vol. 407, Astrophysics and Space Science Library, ed. A. Lazarian, E. M. de Gouveia Dal Pino, & C. Melioli, 507

Beck, R., Brandenburg, A., Moss, D., Shukurov, A., & Sokoloff, D. 1996, ARA&A, 34, 155

Beck, R. & Krause, M. 2005, Astronomische Nachrichten, 326, 414

Beck, R., Loiseau, N., Hummel, E., et al. 1989, A&A, 222, 58

Beck, R. & Wielebinski, R. 2013, Magnetic Fields in Galaxies, ed. T. D. Oswalt & G. Gilmore, 641

Bell, E. F. 2002, ApJ, 577, 150

Bell, E. F. 2003, ApJ, 586, 794

Bendo, G. J., Dale, D. A., Draine, B. T., et al. 2006, ApJ, 652, 283

Berkhuijsen, E. M., Mitra, D., & Mueller, P. 2006, Astronomische Nachrichten, 327, 82

Berkhuijsen, E. M. & Müller, P. 2008, A&A, 490, 179

Birk, G. T., Lesch, H., & Zimmer, F. 1998, Physica Scripta Volume T, 74, 89

Blain, A., Combes, F., & Draine, B. T. 2002, The Cold Universe: Saas-Fee Advanced Course 32 (Springer)

Brandenburg, A., Chatterjee, P., Del Sordo, F., et al. 2010, Physica Scripta Volume T, 142, 014028

Bregman, J. N. & Pildis, R. A. 1994, ApJ, 420, 570

Brentjens, M. A. & de Bruyn, A. G. 2005, A&A, 441, 1217

Briggs, D. S. 1995, in Bulletin of the American Astronomical Society, Vol. 27, American Astronomical Society Meeting Abstracts, 112.02

Burn, B. J. 1966, MNRAS, 133, 67

Calzetti, D. 2001, PASP, 113, 1449

Calzetti, D., Kennicutt, R. C., Engelbracht, C. W., et al. 2007, ApJ, 666, 870

Calzetti, D., Kennicutt, Jr., R. C., Bianchi, L., et al. 2005, ApJ, 633, 871

Caprini, C., Durrer, R., & Fenu, E. 2009, J. Cosmology Astropart. Phys., 11, 1

Carilli, C. L. & Taylor, G. B. 2002, ARA&A, 40, 319

Chanmugam, G. 1992, ARA&A, 30, 143

Cho, J. & Ryu, D. 2009, ApJ, 705, L90

Chrysostomou, A., Aitken, D. K., Jenness, T., et al. 2002, A&A, 385, 1014

Clark, B. G. 1980, A&A, 89, 377

Combes, F. 1978, in IAU Symposium, Vol. 77, Structure and Properties of Nearby Galaxies, ed. E. M. Berkhuijsen & R. Wielebinski, 275

Cornwell, T. J. 2008, IEEE Journal of Selected Topics in Signal Processing, 2, 793

Courtillot, V. & Le Mouel, J. L. 1988, Annual Review of Earth and Planetary Sciences, 16, 389

Cox, D. P. 2005, ARA&A, 43, 337

Crillon, R. & Monnet, G. 1969, A&A, 2, 1

Crutcher, R. M. 2012, ARA&A, 50, 29

Dale, D. A., Bendo, G. J., Engelbracht, C. W., et al. 2005, ApJ, 633, 857

Dale, D. A., Gil de Paz, A., Gordon, K. D., et al. 2007, ApJ, 655, 863

Dale, D. A. & Helou, G. 2002, ApJ, 576, 159

de Bruyn, A. G. & Brentjens, M. A. 2005, A&A, 441, 931

Dickinson, C., Davies, R. D., & Davis, R. J. 2003, MNRAS, 341, 369

Donahue, M., Aldering, G., & Stocke, J. T. 1995, ApJ, 450, L45

Donati, J.-F. & Landstreet, J. D. 2009, ARA&A, 47, 333

Dotson, J. L., Davidson, J., Dowell, C. D., Schleuning, D. A., & Hildebrand, R. H. 2000, ApJS, 128, 335

Draine, B. T. 2003, ARA&A, 41, 241

Draine, B. T. 2010, Physics of the Interstellar and the Intergalactic Medium (Princeton University Press)

Drzazga, R. T., Chyży, K. T., Jurusik, W., & Wiórkiewicz, K. 2011, A&A, 533, A22

Dumke, M. & Krause, M. 1998, in Lecture Notes in Physics, Berlin Springer Verlag, Vol. 506, IAU Colloq. 166: The Local Bubble and Beyond, ed. D. Breitschwerdt, M. J. Freyberg, & J. Truemper, 555–558

Dumke, M., Krause, M., & Wielebinski, R. 2004, A&A, 414, 475

Dumke, M., Krause, M., Wielebinski, R., & Klein, U. 1995, A&A, 302, 691

Duric, N., Seaquist, E. R., & Crane, P. C. 1982, AJ, 87, 1671

Ekers, R. D. & Sancisi, R. 1977, A&A, 54, 973

Fanaroff, B. L. & Riley, J. M. 1974, MNRAS, 167, 31P

Fletcher, A., Beck, R., Shukurov, A., Berkhuijsen, E. M., & Horellou, C. 2011, MNRAS, 412, 2396

Gardner, F. F. & Whiteoak, J. B. 1966, ARA&A, 4, 245

Golla, G. 1999, A&A, 345, 778

Golla, G., Dettmar, R.-J., & Domgoergen, H. 1996, A&A, 313, 439

Golla, G. & Hummel, E. 1994, A&A, 284, 777

Golla, G. & Wielebinski, R. 1994, A&A, 286, 733

Gómez, G. C. & Cox, D. P. 2002, ApJ, 580, 235

Green, D. A. 2002, in IAU Symposium, Vol. 199, The Universe at Low Radio Frequencies, ed. A. Pramesh Rao, G. Swarup, & Gopal-Krishna, 276

Hall, J. S. & Mikesell, A. H. 1949, AJ, 54, 187

Hanasz, M., Wóltański, D., & Kowalik, K. 2009, ApJ, 706, L155

Hanayama, H., Takahashi, K., Kotake, K., et al. 2005, ApJ, 633, 941

Haverkorn, M. 2015, in Astrophysics and Space Science Library, Vol. 407, Astrophysics and Space Science Library, ed. A. Lazarian, E. M. de Gouveia Dal Pino, & C. Melioli, 483

Heald, G., Braun, R., & Edmonds, R. 2009, A&A, 503, 409

Heckman, T. M., Armus, L., & Miley, G. K. 1990, ApJS, 74, 833

Heesen, V., Beck, R., Krause, M., & Dettmar, R.-J. 2009a, A&A, 494, 563

Heesen, V., Krause, M., Beck, R., & Dettmar, R.-J. 2009b, A&A, 506, 1123

Hiltner, W. A. 1949, Science, 109, 165

Ho, L. C., Filippenko, A. V., & Sargent, W. L. 1995, ApJS, 98, 477

Hoopes, C. G., Walterbos, R. A. M., & Rand, R. J. 1999, ApJ, 522, 669

Hovatta, T., Lister, M. L., Aller, M. F., et al. 2012, AJ, 144, 105

Hummel, E. & Dettmar, R.-J. 1990, A&A, 236, 33

Hummel, E., Lesch, H., Wielebinski, R., & Schlickeiser, R. 1988, A&A, 197, L29

Irwin, J., Beck, R., Benjamin, R. A., et al. 2012a, AJ, 144, 44

Irwin, J., Beck, R., Benjamin, R. A., et al. 2012b, AJ, 144, 43

Irwin, J., Krause, M., English, J., et al. 2013, AJ, 146, 164

Irwin, J. A., Henriksen, R. N., Krause, M., et al. 2015, ApJ, 809, 172

Irwin, J. A., Wilson, C. D., Wiegert, T., et al. 2011, MNRAS, 410, 1423

Israel, F. P. & van der Hulst, J. M. 1983, AJ, 88, 1736

Jones, C. A. 2011, Annual Review of Fluid Mechanics, 43, 583

Karachentsev, I. D., Bautzmann, D., Neyer, F., et al. 2014, ArXiv e-prints

Kennicutt, R. C., Calzetti, D., Aniano, G., et al. 2011, PASP, 123, 1347

Kennicutt, Jr., R. C. 1998, ARA&A, 36, 189

Kennicutt, Jr., R. C., Armus, L., Bendo, G., et al. 2003, PASP, 115, 928

Kennicutt, Jr., R. C., Calzetti, D., Walter, F., et al. 2007, ApJ, 671, 333

Kennicutt, Jr., R. C., Hao, C.-N., Calzetti, D., et al. 2009, ApJ, 703, 1672

Klein, U. & Fletcher, A. 2015, Galactic and Intergalactic Magnetic Fields (Springer)

Klein, U., Wielebinski, R., & Beck, R. 1984, A&A, 133, 19

Krause, M. 2003, Acta Astronomica Sinica, 44, 123

Krause, M. 2009, in Revista Mexicana de Astronomia y Astrofisica Conference Series, Vol. 36, 25–29

Krause, M. 2012, in Magnetic Fields in the Universe III: From Laboratory and Stars to Primordial Structures, Proceedings of the International Conference, ed. M. Soida, K. Otmianowska-Mazur, E. M. de Gouveia Dal Pino & A. Lazarian, 155–158

Krause, M., Golla, G., Morita, K.-I., & Wielebinski, R. 1994, in Astronomical Society of the Pacific Conference Series, Vol. 59, IAU Colloq. 140: Astronomy with Millimeter and Submillimeter Wave Interferometry, ed. M. Ishiguro & J. Welch, 363

Kruegel, E. 2003, The physics of interstellar dust

Krügel, E., ed. 2002, Wiley Praxis Series in Astronomy and Astrophysics, Vol. 10, The Physics of Interstellar Dust

Lai, S.-P., Crutcher, R. M., Girart, J. M., & Rao, R. 2001, ApJ, 561, 864

Lara, L., Mack, K.-H., Lacy, M., et al. 2000, A&A, 356, 63

Leahy, J. P., Muxlow, T. W. B., & Stephens, P. W. 1989, MNRAS, 239, 401

Leahy, J. P. & Williams, A. G. 1984, MNRAS, 210, 929

Lee, S.-W., Irwin, J. A., Dettmar, R.-J., et al. 2001, A&A, 377, 759

Leroy, A. K., Bigiel, F., de Blok, W. J. G., et al. 2012, AJ, 144, 3

Liu, J. 2011, ApJS, 192, 10

Longair, M. S. T. E. 2011, High-energy astrophysics (Cambridge University Press)

Maiolino, R. & Rieke, G. H. 1995, ApJ, 454, 95

Makarov, D. & Karachentsev, I. 2011, MNRAS, 412, 2498

Mao, S. A., Zweibel, E., Fletcher, A., Ott, J., & Tabatabaei, F. 2015, ApJ, 800, 92

Martin, C. & Kern, B. 2001, ApJ, 555, 258

Martinez-Delgado, D., D'Onghia, E., Chonis, T. S., et al. 2014, ArXiv e-prints

McConnachie, A. W., Patton, D. R., Ellison, S. L., & Simard, L. 2009, MNRAS, 395, 255

McKee, C. F. & Ostriker, E. C. 2007, ARA&A, 45, 565

Meléndez, M., Veilleux, S., Martin, C., et al. 2015, ArXiv e-prints

Melia, F. 2009, High-energy astrophysics (Princeton University Press)

Mora, S. C. 2012, Master's thesis, University of Bonn

Mora, S. C. & Krause, M. 2013, A&A, 560, A42

Moustakas, J., Kennicutt, Jr., R. C., & Tremonti, C. A. 2006, ApJ, 642, 775

Murphy, E. J. 2009, ApJ, 706, 482

Murphy, E. J., Helou, G., Kenney, J. D. P., Armus, L., & Braun, R. 2008, ApJ, 678, 828

Neininger, N. & Dumke, M. 1999, Proceedings of the National Academy of Science, 96, 5360

Niklas, S., Wielebinski, R., Klein, U., & Braine, J. 1996, in IAU Symposium, Vol. 171, New Light on Galaxy Evolution, ed. R. Bender & R. L. Davies, 424

Norman, C. A. & Ikeuchi, S. 1989, ApJ, 345, 372

Oppermann, N., Junklewitz, H., Robbers, G., et al. 2012, A&A, 542, A93

Pacholczyk, A. G. 1970, Radio Astrophysics (W. H. Freeman and Company)

Parker, E. N. 1970, ARA&A, 8, 1

Pérez-González, P. G., Kennicutt, Jr., R. C., Gordon, K. D., et al. 2006, ApJ, 648, 987

Pérez-Sánchez, A. F. & Vlemmings, W. H. T. 2013, A&A, 551, A15

Pérez-Sánchez, A. F., Vlemmings, W. H. T., Tafoya, D., & Chapman, J. M. 2013, MNRAS, 436, L79

Pizzo, R. F., de Bruyn, A. G., Bernardi, G., & Brentjens, M. A. 2011, A&A, 525, A104

Poglitsch, A., Waelkens, C., Geis, N., et al. 2010, A&A, 518, L2

Rand, R. J. 1994, A&A, 285, 833

Rand, R. J. 1997, ApJ, 474, 129

Rand, R. J. 2000, ApJ, 535, 663

Rand, R. J., Kulkarni, S. R., & Hester, J. J. 1992, ApJ, 396, 97

Rand, R. J. & van der Hulst, J. M. 1993, AJ, 105, 2098

Rau, U. & Cornwell, T. J. 2011, A&A, 532, A71

Read, A. M., Ponman, T. J., & Strickland, D. K. 1997, MNRAS, 286, 626

Rees, M. J. 2005, in Lecture Notes in Physics, Berlin Springer Verlag, Vol. 664, Cosmic Magnetic Fields, ed. R. Wielebinski & R. Beck, 1

Relaño, M., Lisenfeld, U., Pérez-González, P. G., Vílchez, J. M., & Battaner, E. 2007, ApJ, 667, L141

Reynolds, R. J. 1990, in IAU Symposium, Vol. 139, The Galactic and Extragalactic Background Radiation, ed. S. Bowyer & C. Leinert, 157–169

Rieke, G. H., Young, E. T., Engelbracht, C. W., et al. 2004, ApJS, 154, 25

Roberts, M. S. 1968, ApJ, 151, 117

Roy, J.-R., Wang, J., & Arsenault, R. 1991, AJ, 101, 825

Schlickeiser, R. 2005, Plasma Physics and Controlled Fusion, 47, A205

Schnitzeler, D. H. F. M., Banfield, J. K., & Lee, K. J. 2015, MNRAS, 450, 3579

Schnitzeler, D. H. F. M. & Lee, K. J. 2015, MNRAS, 447, L26

Seth, A. C., Dalcanton, J. J., & de Jong, R. S. 2005, AJ, 130, 1574

Shneider, C., Haverkorn, M., Fletcher, A., & Shukurov, A. 2014, A&A, 568, A83

Sievers, A. 1988, PhD thesis, University of Bonn

Smith, A. M., Collins, N. R., Waller, W. H., et al. 2001, ApJ, 546, 829

Soida, M. 2005, in The Magnetized Plasma in Galaxy Evolution, ed. K. T. Chyzy, K. Otmianowska-Mazur, M. Soida, & R.-J. Dettmar , 185–190

Soida, M., Krause, M., Dettmar, R.-J., & Urbanik, M. 2011, A&A, 531, A127

Sokoloff, D. D., Bykov, A. A., Shukurov, A., et al. 1998, MNRAS, 299, 189

Soria, R. & Ghosh, K. K. 2009, ApJ, 696, 287

Sukumar, S. & Velusamy, T. 1985, MNRAS, 212, 367

Sun, X. H. & Reich, W. 2009, A&A, 507, 1087

Tabatabaei, F. S., Beck, R., Krügel, E., et al. 2007, A&A, 475, 133

Tamhane, P., Wadadekar, Y., Basu, A., et al. 2015, MNRAS, 453, 2438

Tomisaka, K. & Ikeuchi, S. 1988, ApJ, 330, 695

Trumpler, R. J. 1930, PASP, 42, 214

Valls-Gabaud, D. 1998, PASA, 15, 111

Vigroux, L. & Nieto, J.-L. 1985, in Lecture Notes in Physics, Berlin Springer Verlag, Vol. 232, New Aspects of Galaxy Photometry, ed. J.-L. Nieto, 67–72

Vogler, A. & Pietsch, W. 1996, A&A, 311, 35

Walterbos, R. A. M. & Greenawalt, B. 1996, ApJ, 460, 696

Wang, B. & Heckman, T. M. 1996, ApJ, 457, 645

Wang, Q. D., Immler, S., Walterbos, R., Lauroesch, J. T., & Breitschwerdt, D. 2001, ApJ, 555, L99

Wang, Q. D., Walterbos, R. A. M., Steakley, M. F., Norman, C. A., & Braun, R. 1995, ApJ, 439, 176

Weliachew, L., Sancisi, R., & Guelin, M. 1978, A&A, 65, 37

Werner, W. 1984, PhD thesis, University of Bonn

Werner, W. 1988, A&A, 201, 1

Widrow, L. M., Ryu, D., Schleicher, D. R. G., et al. 2012, Space Sci. Rev., 166, 37

Wiegert, T., Irwin, J., Miskolczi, A., et al. 2015, AJ, 150, 81

Wielebinski, R. & Krause, F. 1993, A&A Rev., 4, 449

Wilson, T. L., Rohlfs, K., & Hüttemeister, S. 2009, Tools of Radio Astronomy (Springer-Verlag)

Zhu, Y.-N., Wu, H., Cao, C., & Li, H.-N. 2008, ApJ, 686, 155

List of Figures

List of Tables

Acknowledgments

I am deeply grateful to Dr. Marita Krause for giving me the opportunity to work on this project and for introducing me to collaborations opening up new scientific perspectives. Thank you Marita for reviewing my chapters so quickly and on such short notice. Many thanks to Dr. Judith Irwin and to the members of the CHANG-ES consortium for the lively exchange of scientific knowledge.

My sincere thanks to Dr. Rainer Beck for all the fruitful discussions and for always pointing me in the right direction. Huge thanks to Dr. Fatemeh Tabatabaei for feedback on the thermal/nonthermal separation chapter. I owe my sincere gratitude to Dr. Peter Müller for always being available to help me with problems no matter how insignificant they were.

I would like to thank Prof. Dr. Michael Kramer for the financial support during my doctorate and for giving me the opportunity to be a part of such an important research group. Many thanks to Gabi Breuer, Tuyet-Le Tran and Kira Kühn for all the logistical help during my time at the Max Planck Institute for Radio Astronomy (MPIfR).

I wish to express my warm thanks to Dr. Rodion Stepanov and Prof. Dr. Peter Frick for hosting me at the Institute of Continuous Media Mechanics in Perm, Russia and for their efforts to share all their wavelet knowledge in such short periods of time. I thank Prof. Dr. Richard Rand for providing the HI map of NGC 4631. The financial support from the International Max Planck Research School (IMPRS) for Astronomy & Astrophysics is gratefully acknowledged. I thank the staff of the Effelsberg and the EVLA telescopes for their assistance with radio observations.

I would like to express my deep gratitude to Dr. Aritra Basu for so patiently guiding me through the thermal/nonthermal separation methods and for all the valuable advice. Thank you for even having the time to go through my scripts and checking for errors. Without your help this work would have not been possible!

A very special thanks to Dr. Theresa Wiegert for all the help with the data reduction and for always welcoming my silly questions, you are an angel! I am also extremely grateful to Dr. Dominic Schnitzeler for taking the time to review a large part of this thesis. Thank you Dominic for sharing your perspectives and always motivating me no matter the circumstances.

I would like to thank some very special people at the MPIfR for all the joyful memories and support: Dr. Denise Riquelme, Pablo Torne, Dr. Juan-Pablo Pérez-Beaupuits, Dr. Luis Esteras, Joey Martinez and especially to my officemate Ancor Damas for putting up with me at the office everyday. My most sincere and deep gratitude to Dr. Ana Ros, Dr. Judith Neumann and Dr. Natasa Tsitali for your encouragement and kind words when I needed them the most. To my awesome friends, Funda Togar and Annika Bente, thank you for the delicious cookie surprise, and for everything you did to brighten my days these past months.

Words are inadequate to express my gratitude to my amazing parents, my ever-cheerful brother and to my sweet Adam for their unconditional love and support. You always point out the larger picture and remind me what really matters. Gracias a tí Jorge M. por inspirarme a conocer nuevos horizontes, espero que estes descubriendo todos los secretos del Universo en tu nuevo estado de existencia. No es una despedida, nos volveremos a ver cerca del mar en Venezuela...

Llevo tu luz y tu aroma en mi piel
y el cuatro en el corazón.
Llevo en mi sangre la espuma del mar
y tu horizonte en mis ojos.
No envidio el vuelo ni el grito al turpial,
soy como el viento en la mies.
Siento el Caribe como una mujer,
soy así, que voy a hacer.
Soy desierto, selva, nieve y volcán,
y al andar dejo mi estela,
y el rumor del llano en una canción que me desvela.
Con tus paisajes y sueños me iré
por esos mundos de Dios.
Y tus recuerdos al atardecer
me harán mas corto el camino.
Entre tus playas quedó mi niñez tendida al viento y al sol.
Y esa nostalgia que hoy sube a mi voz,
sin querer se hizo canción.
De los montes quiero la inmensidad y del río la acuarela.
Y de ti los hijos que sembrarán nuevas estrellas.
Y si un día tengo que naufragar y un tifón rompe mis velas,
enterrad mi cuerpo cerca del mar en Venezuela.
Luis Silva